Techniques for Noise Suppression and Robust Control in Spin-Based Quantum Information Processors

by

Troy William Borneman

Submitted to the Department of Nuclear Science and Engineering
in partial fulfillment of the requirements for the degree of

Doctor of Philosophy in Nuclear Science and Engineering

at the

MASSACHUSETTS INSTITUTE OF TECHNOLOGY

December 2012
[FEBRUARY 2013]

Author .....
Department of Nuclear Science and Engineering
December, 2012

Certified by .....
David G. Cory
Professor
Thesis Supervisor

Read By .....
Paola Cappellaro
Assistant Professor

Accepted by .....
Mujid S. Kazimi
Chairman, Department Committee on Graduate Students

Techniques for Noise Suppression and Robust Control in Spin-Based Quantum Information Processors

by

Troy William Borneman

Submitted to the Department of Nuclear Science and Engineering
on December, 2012, in partial fulfillment of the
requirements for the degree of
Doctor of Philosophy in Nuclear Science and Engineering

Abstract

Processing information quantum mechanically allows the relatively efficient solution of many important problems thought to be intractable on a classical computer. A primary challenge in experimentally implementing a quantum information processor is the control and suppression of environmental noise that decoheres the quantum system and causes it to behave classically. Environmental errors may be dynamically suppressed by applying coherent control pulses to the qubits that decouple the environment. However, the pulses themselves are subject to implementation errors, which hinders the ability to robustly store a complete quantum state.

This thesis details results on the use of optimal control theory, noise twirling, and logical qubit encodings to design high-fidelity control pulses and decoupling sequences that are robust to implementation errors. Results are also presented that demonstrate how high-fidelity inductive control of a quantum system may be obtained with limited resonator bandwidth, with a discussion of applications to actuator-based quantum information processors. In a multinode design for such a processor, which allows efficient removal of entropy, a new protocol is suggested that permits robust parallel information transfer between nodes.

The results detailed in this thesis apply broadly to most implementations of quantum information processing and specifically enable a new design for a spin-based multinode quantum information processor based on single-crystal molecular monolayer electron-nuclear spin systems integrated with superconducting electronics.

Thesis Supervisor: David G. Cory
Title: Professor

Acknowledgments

The years of dedication and study required to complete a doctoral dissertation are at once arduous and enlightening. By far the greatest reward comes from those I have had the privilege to interact with along the way. This work represents the culmination of many collaborations and discussions with many talented researchers and thinkers. There are simply too many people to thank, so if I have neglected to mention someone I am deeply sorry.

First and foremost I would like to thank my advisor, David Cory, for his help and guidance over the course of my research and studies. His vast knowledge and experience have been crucial in helping me to navigate the complex field of quantum information processing. By constantly challenging me, he has pushed me toward achieving my full potential as a researcher and scientist.

I would also like to thank Bruce Boghosian, who both introduced me to the field and to Professor Cory. Without him I would have never embarked on the journey of graduate school and been given the opportunity to conduct the research presented in this thesis. The support and advice offered by Chandrasekhar Ramanathan and Paola Cappellaro have also helped me grow as a scientist and person.

I was fortunate to be part of a research group that grew significantly in size since the time I first started graduate school. The wide range of knowledge and unique perspectives offered by the many members of Professor Cory's group have been a constant source of inspiration. Thanks to all of you for creating such an engaging and stimulating research environment.

I would like to particularly acknowledge those with whom I directly collaborated on the work presented in this thesis: Martin Hurlimann and the NMR group at Schlumberger-Doll Research, Chris Granade, Holger Haas, Jeremy Chamilliard, and Easwar Magesan. I look forward to working with you all more in the future.

The completion of this work wouldn't have been possible without the unconditional support of family and friends. I would like to especially thank Shannon Curry for being my partner in one of the most challenging years of my life. Thanks also

to Tony Fonseca for many engaging discussions about politics, science, and countless other topics that have helped me to put my work and life in perspective. A great future awaits you both and I can't wait to see what you accomplish.

I am also grateful for the continued support of old friends in Boston. Sean Lewis, Jordan Edwards, Heather Terkla, Katie McCarty, Pete Maher, Jeremy Scanlan, and Bryan Swaim, thanks to all of you for always being there.

Moving to Waterloo midway through my studies presented a unique set of challenges. I am indebted to Jonathan Lavoie for making me feel welcome in a new country and introducing me to many great friends. The friends I've made in Canada have helped to make the move all the more worth it. Rainer Kaltenbaek, Adriana and Ernesto Morales, Anna-Lina and Bill Bombardier, though you've moved on, I'll never forget the times we spent together. Thanks also to Adam and Marion Paetznick, Lori Woolner Melko, Halle Revell, Andrew Achkar, Ann Kallin, Chad Daley, Sarah Sheldon, Ivar Taminiau, and Pat Gumann for many great times.

Finally, the love and support of my parents, Terry and Louise, and my sisters, Tracy and Jennie, has sustained me throughout my life. To you I dedicate this thesis.

Foreword

This dissertation is about control strategies for quantum devices in the presence of environmental noise, specifically targeted toward achieving large-scale multinode quantum information processing with electron and nuclear spins. The engineering of such a device would serve as a test-bed for control methods and design for large-scale quantum systems, with the potential for scalability and integration with other devices. The structure of the dissertation is the following: Chapter 1 provides context by detailing the basic notions of quantum information processing, quantum error correction, and quantum devices, and introduces the discussion of multinode quantum information processing in Chapter 3. Chapter 2 reviews the background material necessary for the treatment of open quantum systems used in Chapters 5, 6, and 7. Chapter 3 briefly reviews spin-based quantum information processing and multinode designs. Chapter 4 introduces a novel theoretical procedure for efficiently transferring information between the nodes of the processor described in Chapter 3. Chapter 5 discusses the procedure for generating high-fidelity quantum gates and formalizes the concept of strongly modulating pulses. Chapter 6 details how numerically optimized pulses may be used to enhance the refocusing properties of a commonly used environmental decoupling sequence and introduces the concept of describing pulse errors in decoupling sequences as a Pauli channel. Chapter 7 builds on the results of Chapter 6 to show how a Pauli channel representation permits concepts from quantum information theory to be applied to suppress pulse errors in decoupling sequences. Chapter 8 details how the control techniques introduced in the preceding chapters may be applied to achieve high-fidelity control with high quality factor resonators. Chapter 9 summarizes all results and their implications, with a discussion of the prospects for building a moderate-scale spin-based quantum information processor.

Contents

1 Introduction: Processing Information with Quantum Devices **25**

1.1 Quantum Computing 26

1.2 Quantum Error Correction 27

1.3 Quantum Devices 29

2 Modeling Open Quantum System Dynamics **31**

2.1 Representations of a Quantum Map 32

2.1.1 χ-Matrix Representation 33

2.1.2 Kraus Representation 33

2.1.3 Pauli Channel Representation 34

2.2 Exact Model of Reduced Dynamics 35

2.3 Incoherent Processes 36

2.4 Stochastic Processes 37

2.5 Markov Processes 40

3 Spin-Based Quantum Information Processing **41**

3.1 Interaction Hamiltonians for Spin-Based QIP 42

3.2 Electron-Nuclear Actuator-Based QIP 44

3.3 Multi-Node Designs 45

4 Efficient Information Transfer In a Multi-Node Quantum Information Processor **49**

4.1 Creating An Effective Cross-Node Processor Coupling 50

4.2 Implementing a Parallel Swap Operation 53
4.3 Robustness to Actuator Noise 54
4.4 Discussion 55

5 Designing Control Sequences to Implement Robust Quantum Gates 57
5.1 Optimizing for a Target Unitary Operation 58
5.1.1 Optimal Control Theory 60
5.1.2 Implementation of Optimal Control 61
5.2 Strongly Modulating Quantum Gates 62
5.2.1 Waugh's Decoupling Criteria 63
5.2.2 Decoupling a Static Environment 65
5.2.3 Generalization to a Stochastic Environment 67
5.3 Discussion 68

6 Refocusing Noise: A Robust CPMG Sequence 71
6.1 CPMG Criteria 73
6.2 Optimization Methods 76
6.2.1 Iterative Optimization Strategy 78
6.3 Simulated Optimization Results 81
6.4 Experimental Verification 85
6.5 Comparison to Previous Pulses 86
6.6 Pulse Error Analysis 90
6.6.1 CPMG Superoperator 90
6.6.2 Pauli Channel Model 91
6.6.3 Validity of Pauli Channel Model 96
6.7 Discussion 98

7 Robust Qubit Storage: XY-Type Sequences and Logical Encodings 101
7.1 Constructing Supercycles to Suppress Pulse Errors 102
7.1.1 Constructing a Primitive Operation 103
7.1.2 Construction of Higher-Order XY-Type Sequences 105

7.2 Pauli Channel Representation of Errors 106
7.3 Twirling The XY-16 Sequence 107
7.3.1 Simulated Twirl 108
7.4 Logical Encoding for Pulse Errors 110
7.4.1 Requirements for Existence of a Logical Encoding 110
7.4.2 A DFS for Pulse Errors 113

8 High-Fidelity Control with High-Q Resonators **117**
8.1 Resonator Model and Ringdown Suppression 119
8.2 Optimizing Bandwidth-Limited Controls 122
8.3 Optimization Results and Experimental Verification 124
8.4 Controllability With Limited Bandwidth 128
8.5 Application of Bandwidth-Limited Control to Electron-Nuclear Spin Systems 131
8.6 Discussion 132

9 Conclusions and Outlook **135**

A Derivation of Gradients for Reactive Controls **139**

List of Figures

3-1 Schematic of a 2×(1e-3n) node structure. The nodes are taken to be identical, with resolved anisotropic hyperfine interactions (solid red lines) between electron actuator spins and nuclear processor spins. The local processors are initially disjoint, but may be effectively coupled (dotted lines) by modulating an isotropic actuator exchange interaction (solid blue double line) and moving into an appropriate microwave Hamiltonian interaction frame. The spin labeling is e_i for electron actuator spins and n_{ij} for nuclear processor spins, where i labels the nodes and j labels the qubits. 46

4-1 The energy level structure of a 2×(1e-1n) system. Quantum information is encoded in the states $|\downarrow\downarrow 00\rangle$, $|\downarrow\downarrow 01\rangle$, $|\downarrow\downarrow 10\rangle$, and $|\downarrow\downarrow 11\rangle$ of the actuator ground-state (Computational) manifold, where arrows indicate electron actuator spin states and binary digits indicate nuclear processor spin states. The desired transition (bold red arrow) for a SWAP operation is implemented by applying a selective microwave field that induces transitions between the two manifolds (dotted lines), effectively moving the induced cross-node processor transitions (dashed lines) in the actuator zero-quantum (ZQ) manifold to the Computational manifold. Note that the actuator excited state manifold, $|\uparrow\uparrow\rangle$, is not included as it is not involved in the internode transfer process. 51

4-2 The induced coupling network of local processor elements consists of interactions between every pair of cross-node spins. For implementation of a parallel swap operation, we wish to keep interactions between identical spins (solid red lines) while refocusing all other interactions (dotted lines). 53

4-3 A plot of the channel fidelity, F, as a function of noise strength, $T_1 = T_2$, scaled by computing $-\log[1 - F]$. The induced channel (solid line) performs significantly better than a serial swap operation (dotted line). Given a modest Rabi frequency, $\omega_1 = 100$ MHz, the induced channel is nearly independent of actuator decoherence for electron relaxation times above 100 μs. 56

6-1 Two representative examples of the iterative optimization procedure utilized in this study. The results shown by the red circles and blue squares correspond to two iterative series of pulses derived from two different random initial guesses, respectively. The pulses are iteratively optimized over an increasing target bandwidth of resonance offsets. We find that, regardless of the initial guess, the resulting curves of average fidelity versus target bandwidth are similar, indicating that the pulses for the different realizations have similar maximum bandwidth. The filled in squares represent the pulses mentioned in the text, with the inset showing the temporal profile of the pulse chosen for extended analysis. High-resolution pulse profile and parameter list is available in supplementary material. 82

6-2 Calculated magnetization as a function of resonance offset for the first (blue), second (red), and 500th (black) echoes of a CPMG sequence using the 1 ms OCT refocusing pulse optimized over $|\Delta\omega| \leq 2\ A_{\max}$. The simulation assumes a perfect excitation pulse, no relaxation, and uniform drive. The time between refocusing pulse applications is $2\tau = 2$ ms. The magnetization is very nearly retained over the entire optimization range, and shows no additional degradation for higher echo numbers. 83

6-3 Fidelity and CPMG criteria as a function of resonance offset for the 1 ms OCT refocusing pulse (Blue) optimized over $|\Delta\omega| \leq 1.6\ A_{\max}$ and $\omega_1 = 0.9 - 1.1$, as compared to a 100 μs hard pulse (Red). The solid lines indicate the response for uniform drive ($\omega_1 = 1$), while the dotted (dash-dotted) lines indicate the maximum (minimum) angle over the range of $\omega_1 = 0.9 - 1.1$. The rotation axis for the OCT pulse stays within 15° of the initial magnetization over the optimized distribution and the nutation angle remains within 30° of 180°. 84

6-4 Experimental results of echo amplitudes generated by CPMG sequences with OCT refocusing pulses (top) and standard hard pulses (bottom) acquired at 300 MHz on a sample of $CuSO_4$ doped 90% D_2O / 10% H_2O with $T_2 \approx$ 270 ms. The results were acquired sequentially by changing the resonance offsets systematically over the range of $|\Delta\omega| \leq 2\ A_{\max}$. The time between refocusing pulses is $2\tau = 20$ ms. The CPMG sequence with OCT pulses generates a uniform response over resonance offsets in the range of ± 1.6 $A_{\max}$. The response of the excitation pulse is shown to be flat over the relevant range of resonance offsets. 86

6-5 Comparison of measured echo amplitudes with different values of 2τ (time between refocusing pulses), as indicated in the legend, for a CPMG sequence with OCT refocusing pulses. The results show that a decrease in echo spacing does not lead to an increase in the relaxation rate, indicating that no additional relaxation is induced by the pulses. In fact, as the echo spacing is decreased and more pulses are applied, the measured relaxation time becomes longer. As discussed in the text, this is caused by T_1 effects during the application of the refocusing pulses. Additionally, the measured echo amplitudes show a small transient effect of roughly 1% amplitude, in agreement with expectation, but not apparent in the current display. . . 87

6-6 Bloch sphere trajectories during the OCT refocusing pulse for several values of resonance offset as applied to a σ_y initial state. The trajectories for different isochromats vary significantly but result in nearly identical effective rotations. Roughly two-thirds of the magnetization is in the transverse plane during pulsing. The black 'o' denotes the initial state, while the black 'x' denotes the final state. 88

6-7 Simulated fidelity as a function of resonance offset for our 1 ms OCT pulse optimized over ±10% RFI and $|\Delta\omega| \leq 1.6\ A_{\max}$ (blue), a previously published OCT excitation pulse [114] optimized over ±20% RFI and $|\Delta\omega| \leq 1.5\ A_{\max}$ and modified to be a 1.02 ms refocusing pulse (red), a 4 ms Chirp refocusing pulse (black) [93], and a 100 μs hard pulse (green). All pulses have maximum RF amplitude $A_{\max}/2\pi = 5$ kHz. The fidelities for each offset were averaged over ±10% RFI ($\omega_1 = 0.9 - 1.1$). High-resolution time-domain profiles for each pulse are included in the supplementary material. 89

6-8 Pauli channel representations for CPMG dynamics using four different refocusing pulses. Probabilities of the identity (black solid), σ_x (red dashed), σ_y (blue dash-dotted), and σ_z (green dotted) operations are shown as a function of the number of cycle applications. The sequences were simulated over $|\Delta\omega| \leq 1.6\ A_{\max}$ and $\omega_1 = 0.9 - 1.1$ with time between refocusing pulses of $2\tau = 2$ ms. Similar behavior is seen when the value of τ is varied. Representation as a Pauli channel allows us to accurately compare the influence of cumulative errors associated with each pulse. The dephasing rate constant, $T_{2,\text{pulse}}$, was taken as the 1/e point in the decay of the identity probability. 94

6-9 Full simulated dynamics for a CPMG sequence and CP sequence using our OCT refocusing pulse optimized and simulated over $|\Delta\omega| \leq 1.6\ A_{\max}$ and a range of drive amplitudes of $\omega_1 = 0.9 - 1.1$. The time between refocusing pulses was set to $2\tau = 2$ ms. The immediate and fast loss of visibility is shown by the initial and asymptotic magnetization being less than unity. The decay of the transients is due to the dephasing portion of the dynamics. Representation of the dynamics as a Pauli channel captures over 99% of the action of the map, describing both the loss of visibility and pulse-induced dephasing. 95

6-10 Decomposition of the propagator characterizing a cycle $[\tau - \pi_y - 2\tau - \pi_y - \tau]$ with OCT pulses (left) and standard hard pulses (right) versus resonance offset. The top panels show the projections of the net rotation axis onto the $\widehat{y}$ axis, the middle panels the nutation angle for a single cycle, and the bottom panels the effective nutation angle for 50 cycles. In each panel, the solid line is the response for uniform drive ($\omega_1 = 1$), while the dashed (dotted) lines indicate the maximum (minimum) over the range of $\omega_1 = 0.9$ - 1.1. The OCT pulse was optimized over $|\Delta\omega| \leq 1.6\ A_{\max}$ with a uniform range of $\omega_1 = 0.9$ - 1.1. For this calculation τ was set to 1 ms. Note that in the top two panels, the scales for the OCT and hard pulses are different. . 99

7-1 Diamond norm distinguishability from a Pauli channel as a function of the number of applied cycles for various decoupling sequences. As the complexity of the cycle increases (from CPMG to XY-16), the resulting channel becomes more accurately representable as a Pauli channel. 106

7-2 Sequence to perform a geometric twirl of pulse errors in the XY-16 sequence. A magic angle rotation (see main text) is performed after each XY-16 sequence consisting of N cycles. Note that the twirling pulse is applied only three times, mitigating the accumulation of errors associated with its implementation. 107

7-3 Result of an ideal twirl of an XY-16 sequence composed of hard pulses. The probability of each Pauli error occuring as a function of the number of cycles contained in each XY-16 sequence are plotted in the absence of twirling (top plot) and in the presence of twirling (bottom plot). In the untwirled case, the σ_z error is dominant, rising in probability as the number of cycles is increased. The σ_x and σ_y error probabilities remain small throughout the examined number of cycles. When twirling is applied, the error probabilities of each Pauli operator become nearly identical over all numbers of cycles considered. 109

8-1 A general resonant transmission circuit may be modeled as a series tuned RLC circuit capacitively coupled to a time-varying voltage source [8] (inset). The quality factor (Q) of the resonator is given mainly by the circuit resonance frequency, $\omega_0 = 1/\sqrt{LC_T}$, the coil inductance,L, and the coil resistance, r: $Q \approx \omega_0 L/r$. The circuit impedance is matched to $R_0 = 50$ Ohms by varying the capacitances C_T and C_M. For high-Q resonators, the dominant transient response of the resonator to a square pulse input of voltage, V_S, (bold line) is an exponential rise (dashed line) and subsequent ring-down (dotted line) of the coil current, i_L, and resulting magnetic field. The ringdown may be suppressed by application of a phase inverted compensation pulse at the end of the square pulse to drive the coil current to zero. The characteristic transient ringdown time without compensation, $\tau_r = Q/\omega_0$, is denoted by a cross. 120

8-2 The bandwidth-limited GRAPE pulse optimization algorithm proceeds in a similar manner as for undistorted controls [105], with the resonator transfer function included in the calculation of the pulse propagator, average gate fidelity, and gradients. The notation is explained in the main text, with $k = 1$ for simplicity. An initial guess of control amplitudes is resampled and convolved with the resonator transfer function to yield a distorted set of control amplitudes including ringdown. A compensation pulse period is then optimized in a sub-routine and appended to the waveform to yield a distorted set of control amplitudes with minimized ringdown. The propagator for each evolution period of the distorted control amplitudes is then calculated and the average gate fidelity computed. The set of propagators is used to calculate the gradient direction of the fidelity with respect to the undistorted controls. A line search is then performed to optimize the step-size in the gradient direction. At each step of the line-search the sub-routines to calculate the updated distorted control amplitudes and corresponding compensation pulse are called, accounting for the compensation pulse not being included in the gradient calculation. The undistorted controls are then updated according to the gradient direction and step-size and the process iterates until a desired value of the fidelity is achieved. 125

8-3 (a) Time-domain profile of a transients optimized OCT pulse with ringdown suppression implementing a $\pi/2)_x$ rotation robust to variations in the static and microwave field strengths. The dashed line represents the undistorted controls and the solid line represents the control fields seen by the spin system after transmission through a resonator with Q = 8,486. The control amplitudes are normalized to a nominal Rabi frequency of $\omega_{1,\mathrm{nom}}/2\pi = 5.26$ MHz. Optimization parameters and further details are discussed in the main text. Note that this pulse is phase-refocused, in that all spins in the sample are rotated with the same phase. (b) Simulated pulse fidelity over an extended range of static and microwave field inhomogeneities, demonstrating the robustness of the pulse. 126

8-4 Digitized pulse and free-induction decay (FID) of irradiated quartz. The transients optimized OCT pulse shown in the previous figure was applied to an inhomogeneously broadened solid-state sample of irradiated fused-quartz in a rectangular cavity with Q = 8,486 at a resonance frequency of 9.5236 GHz. The black solid line for $t < 0$ shows the pulse profile digitized through a pick-up coil inserted in the cavity. The digitized profile closely matches the calculated profile with the only ringdown being a small oscillation which decays after roughly 75 ns. The resulting quartz FID is shown as a blue solid line for $t > 0$ and was acquired after a 75 ns spectrometer deadtime. The static field was moved roughly 2 MHz off-resonance (still within the high-fidelity operation regime of the pulse, as shown in Figure 8-3) to emphasize the shape of the FID. For comparison, a digitized square pulse of length 1 μs is shown as the black dashed line. In a separate measurement, the necessary spectrometer deadtime in the absence of ringdown suppression was determined to be 1.2 μs (shown as a dotted vertical line), which would prevent the detection of a significant portion of the FID. The separate plots have been scaled for visual clarity. 127

8-5 (a) The undistorted (dashed line) and distorted (solid line) control amplitudes of a pulse designed to perform a π rotation of the electron spin in a resonator with Q = 10,000. Access to such an operation guarantees universal control of the nuclear spin via electron-only modulation [86]. The pulse consists of 500 time steps of Δt= 10 ns each for a total length of 5 μs, with $\omega_{1,\mathrm{nom}}/2\pi$ = 100 MHz. The simulated average gate fidelity is Φ = 0.9901. (b) The single-sided amplitude spectrum of the undistorted pulse (dotted line) and the distorted pulse (solid line) filtered by the resonator admittance function (bold solid line). The transitions necessary to achieve the desired operation were separated by an amount ($|\omega_{23} - \omega_{14}|$ = 51 MHz) much greater than the bandwidth of the resonator ($\approx$ 1.2 MHz), demonstrating that linear response may be greatly exceeded by pulses of high complexity optimized under a sufficiently accurate system model. . . 133

9-1 Schematic diagram of possible processor layout and addressing scheme. Each small blue square region denotes a node of the processor, containing a single molecule with a single electron spin coupled to ten nuclear spins – a candidate molecule is perchlorotriphenylmethyl (PTM) [7]. The black square regions denote a plaquette that is identically repeated about 10^6 times to allow inductive ensemble measurements. Four of the nuclear spins are used as classical bits to spatially label the nodes within each plaquette. The remaining six nuclear spins may be used as coherent processing qubits, leading to a total of 96 qubits in the processor. 137

List of Tables

6.1 Dephasing rate and asymptotically retained magnetization for CPMG sequences using four different types of refocusing pulses. 96

Chapter 1

Introduction: Processing Information with Quantum Devices

The idea of manipulating information within a physical system to perform a useful computation has been around for millenia and has led in the last century to a technological revolution based on digital computing devices. The notion of computation has been formalized as a Turing machine [203], where an infinitely long tape containing discrete symbols representing *states* is passed through a processing device that reads each symbol in turn and writes a new symbol based on a simple set of rules. Although no modern computer is built in this way, the computational power of any computing device is polynomially related to a Turing machine. In terms of Shannon's quantification of information in terms of the number of state configurations possible for a physical system [181], quantum mechanical systems – whose state space grows exponentially with the size of the physical system – offer tremendous potential for information storage and computation. The formalization of a *quantum* Turing machine [13, 14, 15] provides a foundation on which to discuss the computational power of a quantum computer [49].

The operating principle of a gate-based digital quantum computer is straightforward: information is stored in a register of quantum bits (qubits) that is operated on by a black-box that manipulates the register state in a deterministic, time-reversable manner. Qubits admit the fundamentally quantum properties of superposition states

and entanglement, and the black-box evolves the qubit register state according to the equations of quantum dynamics. It is believed that the power of a quantum information processing device is based on the ability to prepare, and maintain under dynamical evolution, coherent superposition states and multi-body states that exhibit non-classical correlated behavior (a generalization of entanglement). While this appears to be true for pure states [101], the existence of non-classical behavior for a thermally mixed ensemble of pure states suggests the origin of the power of quantum devices is more subtle [121]. Nevertheless, the capability to maintain coherence and entanglement of pure states during evolution is sufficient for quantum information processing and serves as a good baseline for evaluating potential quantum devices.

1.1 Quantum Computing

We will use a general model for the physical implementation of quantum computation based on an array of coupled quantum systems whose state is manipulated by electromagnetic radiation [128]. Early suggestions for appropriate physical systems included nuclear spins in liquid-state nuclear magnetic resonance (NMR) systems [41, 69] or silicon [104], quantum dots [132], and trapped ions [152, 39]. There are many challenges facing experimental implementations of quantum computing [50, 38], which have been formally expressed as the five *DiVincenzo criteria* for physically realizable quantum computation [52]:

1. A scalable physical system with well characterized qubits
2. The ability to initialize the state of the qubits to a simple fiducial state
3. Decoherence times much longer than gate operation times
4. The ability to implement a universal set of quantum gates
5. The ability to measure individual qubits

At the base level, a physical system must be engineered and characterized to yield a set of well defined qubits which may be controlled, initialized, and measured by some

means. These qubits need not be isolated two-level systems, such as spin-1/2 electrons or nuclei, but may be logically defined as a subspace of a larger energy structure [213]. Given a sufficiently detailed description of the physical system, control sequences must be developed that generate a universal set of quantum gates in the presence of noise [51]. A relatively small set of repeatable single-qubit and two-qubit gates may be used to build up any quantum computation [26].

The challenge for designing gates for a particular physical system stems from sufficiently suppressing environmental decoherence. The effect of an environment coupled to the quantum system was raised as one of the first questions posed when considering if experimental quantum computation was possible [129, 207, 123] and remains as an intense area of current study [120]. In any practical implementation of a quantum device there are many degrees of freedom which we either cannot control or don't have sufficient knowledge of to describe in full detail. These uncontrolled degrees of freedom comprise the *environment* and the combination of the qubits and the environment is an *open* quantum system.

The statement that we must both isolate qubits and perform quantum gates on them at first seems paradoxical, as manipulating the state of a qubit necessarily means interacting with it, requiring coupling to external fields that should act as a decohering environment. However, as will be the focus of much of this work, the applied external fields may actually be used to remove the effects of environmental noise, provided the environment has sufficient memory. For situations where environmental effects may not be suppressed directly through control sequences, quantum error correction schemes may be used to mitigate the errors induced by the environment.

1.2 Quantum Error Correction

Due to the no-cloning theorem of quantum mechanics [222], an arbitrary quantum state to be protected against errors may not be simply copied across several qubits, as is done in repetition codes for classical computing. Instead, a single quantum state must be encoded in a subspace of a larger number of qubits to allow for the detection

and correction of errors. For example, the *bit-flip code* stores a single quantum state, $|\Psi\rangle = \alpha|0\rangle + \beta|1\rangle$, as a superposition state over three qubits:

$$|\Psi_L\rangle = \alpha|000\rangle + \beta|111\rangle . \tag{1.1}$$

This code protects against a single bit-flip error, which is represented as a Pauli X operation, σ_x, being applied to the state with probability p:

$$|\Psi\rangle \mapsto \sqrt{(1-p)}|\Psi\rangle + \sqrt{p}\sigma_x|\Psi\rangle . \tag{1.2}$$

A simple basis transformation of this code protects against a phase flip, σ_z, or bit-phase-flip, σ_y, error. Other examples of common quantum error correcting codes are the *Shor code*, which uses nine physical qubits to encode a single logical qubit that allows for the detection and correction of any arbitrary error on a single qubit [182], and the *Steane code*, that requires only seven physical qubits [194]. The smallest code for arbitrary errors on a single qubit provably uses five physical qubits, and is referred to as the *perfect code* due to its optimality in qubit resources [122].

An implementation of a gate on encoded qubits is said to be *fault tolerant* if the error rate for the gate is below cp^2, where c is a constant, guaranteeing that a single error will not propagate to cause an unrecoverable error. The accuracy thresholds for error rates required for fault tolerance may be described in the stabilizer formalism in terms of the generators of the set of correctable errors [72]. Recent arguments suggest that gate error rates of less than 10^{-5} [4, 195] are necessary before QEC may be applied to reach fault tolerance. Achieving these gate error rates requires the design of robust coherent control pulses that are insensitive to the environment.

The overarcing principle of quantum error correction is the encoding of quantum information into subspaces of a large Hilbert space where noise does not operate, or obeys convenient symmetries. This unifies the concepts of *passive* codes, such as decoherence-free subspaces (see Section 7.4), that aim to prevent errors from occuring, and the aforementioned *active* codes that aim to detect and correct errors after they occur [112]. An example of using only a small portion of a physical Hilbert space for

encoding of qubits is planar surface codes [111, 48]. Surface codes spatially delocalize quantum information over a regular two-dimensional array of physical qubits, thereby offering enhanced protection against any errors on locally acting gates. At the expense of requiring a very large number of physical qubits to encode logical qubits, the single gate error threshold for a surface code approaches 1% [63]. Another advantage of surface codes is the natural mapping to qubit arrangements conveniently realized in physical systems, particularly multi-node configurations (see Section 3.3).

1.3 Quantum Devices

It is generally thought that despite the enormous progress achieved in the time since quantum computers were first suggested, realization of a fully scalable quantum computer is still a long way off. In the meantime, the research devoted to building a quantum computer has practical applications that are either currently viable, or will be in the near future. Particularly, the prospect of engineering devices to perform specialized tasks that take advantage of our ability to understand and control physical systems at the quantum level is already emerging as a reality. For example, taking advantage of quantum coherence in a physical system leads to unprecendented sensitivity in sensors built with nitrogen-vacancy centers in diamond [142, 161] and neutron interferometry [165]. Quantum cryptography [58] has also been developed to the point that several devices are commercially available. The continued development of quantum repreaters [28] to counter photon loss in quantum communication devices will allow larger range and further application of these devices.

Special purpose quantum processors that do not require universality or scalability may also have a significant impact. The quintessential example is a quantum simulator [60, 130], which was initially demonstrated in NMR [192]. Without providing universal quantum computation, such a device could allow the investigation of physical phenomena too complex to be understood numerically or analytically. Another example of a special purpose quantum processor is a module that performs only an efficient quantum Fourier transform (QFT), which is an integral part of many quan-

tum algorithms [100]. Such a processor could be used not only as a unit of a larger quantum processor, but also as an efficient replacement for classical Fourier transform modules, with broad implications for signal processing. Increasing our understanding of the control and error suppression of open quantum system dynamics not only will help pave the way toward a quantum computer, but will also enhance the performance of a wide range of quantum devices currently in use and in development.

Chapter 2

Modeling Open Quantum System Dynamics

Designing control sequences to implement high-fidelity gates and suppress decoherence in open quantum systems requires an accurate model of the system dynamics. In this chapter we review the aspects of modeling the dynamics of open quantum systems necessary to develop the control schemes discussed in the remainder of the work. Much of the discussion in this chapter is contained within standard references for the treatment of open quantum systems [27, 158, 66].

A standard description of an open quantum system is in terms of three distinct physical spaces: the relevant qubit degrees of freedom, the immediate environment that couples to the qubits, and the extended environment (lattice) that induces fluctuations of the environment, leading to dissipation on the qubits. This model is motivated by the physical situations commonly encountered in experiments; for example, for superconducting devices the qubits would be quantized current, charge, or flux in a superconducting material with incorporated Josephson junctions, the immediate environment is a collection of 2-level systems coupling to the qubits, and the lattice causes fluctuations of the 2-level systems - perhaps surface states or bond rotations in the device materials. Another example is electron-nuclear spin systems, where the qubits are the spin degree of freedom of electrons and nuclei, the environment is other degrees of freedom not used as qubits, and the lattice is Raman processes that cause

fluctuations. In the presence of a drive term, H_d, of strength ω_d, that operates only on the qubits, the total system Hamiltonian may be written as:

$$H_{tot} = H_Q \otimes \mathbb{I}_E + \mathbb{I}_Q \otimes H_E(t) + \omega_d(t) H_d + \alpha H_{QE}, \tag{2.1}$$

where H_Q and $H_E(t)$ are the drift Hamiltonians for the qubits and environment, respectively. The lattice is implicitly included as inducing the time-dependence of H_E. The qubit-environment interaction, H_{QE}, operates on the joint qubit-environment Hilbert space with a strength α defined by the operator norm of the general qubit-environment Hamiltonian. The full system dynamics evolves according to the Liouville-von Neumann equation,

$$\frac{\partial}{\partial t}\rho(t) = -i\left[H_{tot}, \rho(t)\right], \tag{2.2}$$

where we have used the common convention $\hbar = 1$. Complete knowledge of the full system Hamiltonian is often not obtainable due to the size and complexity of the environment. Thus, practical calculations normally require reducing the effective dynamics to operate only on the qubit subspace. The reduced dynamics may be fully and generally described as a map, $\mathcal{E}$, which operates on ρ as $\mathcal{E}(\rho) \mapsto \rho'$. Determining the map for a given noise model depends on the nature of the noise process in question.

2.1 Representations of a Quantum Map

Several representations of $\mathcal{E}$ are commonly used, with each being convenient for certain calculations. The standard representation is in terms of a superoperator that defines how any valid input state in a particular basis evolves into a valid output state in the same basis. The Pauli basis is often used, consisting of $n-$fold tensor products of the usual spin-1/2 Pauli operators, where n is the number of qubits. In superoperator form, the Liouville-von Neumann equation is written in terms of columnized density matrices, $\hat{\rho}$ - obtained by stacking the columns of ρ on top of one another in a right

to left fashion [81] - acted upon by a Liouvillian superoperator, $\mathcal{L} = \overline{H} \otimes I - I \otimes H$:

$$\frac{\partial}{\partial t}\hat{\rho}(t) = \mathcal{L}(t)\hat{\rho}(t). \tag{2.3}$$

2.1.1 χ-Matrix Representation

Given a basis, $\{P_i\}$, for a D-dimensional Hilbert space, the χ-matrix is defined as

$$\mathcal{E}(\rho) = \sum_{i,j} \chi_{ij} P_i \rho P_j, \tag{2.4}$$

and may be simply derived from the superoperator representation [81, 221]. The χ-matrix is often referred to as the *process matrix* because it reveals the operational form of the processes occuring during the map in the chosen basis.

2.1.2 Kraus Representation

While a general quantum process may be conveniently described by a superoperator, representing the system as a density matrix requires the map to be completely positive and trace-preserving (CPTP). Requiring a map to be positive and trace-preserving ensures that valid quantum states – given by positive, Hermitean density operators – are mapped to other valid quantum states, and that probability is conserved. Demanding that the map be completely positive ensures that the same is true when the map is considered as a subsystem of a larger quantum system. Any map that is CPTP admits representation in a Kraus form [115]:

$$\rho_{\text{out}} = \sum_k p_k A_k \rho_{\text{in}} A_k^\dagger, \tag{2.5}$$

where for every instant in time there is a probability, p_k, of the qubits undergoing evolution under the Kraus operator, A_k, accounting for the influence of the environment. The form of the Kraus operators depends on the particular qubit-environment

model being considered. Requiring preservation of the trace introduces the restriction

$$\sum A_k A_k^\dagger = I. \tag{2.6}$$

There are an infinite number of Kraus representations for a particular map, related to one another by a unitary transformation, but only one maximizes the linear independence of the operators. This unique representation is determined by the eigenvectors and eigenvalues of the Choi matrix [37].

2.1.3 Pauli Channel Representation

A channel which admits representation as a χ-matrix which is diagonal in the Pauli basis is called a Pauli channel, $\mathcal{E}_p$

$$\mathcal{E}_p(\rho) = \sum_i p_i \sigma_i \rho \sigma_i, \tag{2.7}$$

where p_i is the probability of the i^{th} Pauli error occuring. We obtain Pauli channels in this work by simple truncation of the off-diagonal elements of the χ-matrix, although recent work has shown how to estimate the Pauli channel representation of a general map that most accurately reflects the errors present in the original map [134]. Pauli channels are often used in the evaluation of error propagation in large quantum systems that do not permit full simulation. The errors are statistically sampled in a Quantum Monte Carlo algorithm [201, 19], with the presence of only diagonal error operators corresponding to a Pauli channel providing relative efficiency. As will be discussed in Chapters 6 and 7, representation of control sequences as Pauli channels allows the application of a number of concepts from quantum information theory to be applied to correct for errors in the sequences.

2.2 Exact Model of Reduced Dynamics

To determine the reduced dynamics on the qubits only, we may apply projection operator techniques [27, 144] to derive a differential equation on the qubit degrees of freedom only - the Nakajima-Zwanzig equation. To derive the equation in the presence of a drive term we first move into an interaction frame that isolates the effect of the qubit-environment coupling:

$$\mathcal{L}_{QE}(t) = \mathcal{S}(t)\mathcal{L}_{QE}\mathcal{S}^{-1}(t), \tag{2.8}$$

with

$$\mathcal{S}(t) = \mathcal{T}e^{-i\int_0^t \mathrm{d}\tau\, \mathcal{L}_Q + \mathcal{L}_E(\tau) + \omega_d(\tau)\mathcal{L}_d}. \tag{2.9}$$

The reduced dynamics are determined by defining operators, $\mathcal{P}$ and $\mathcal{Q}$, that act on the total system density matrix, ρ, to project onto the qubit degrees of freedom and environmental degrees of freedom, respectively. The system projection operator is defined as

$$\mathcal{P}\rho := \mathrm{Tr}_E(\rho) \otimes \rho_B, \tag{2.10}$$

where ρ_B is an arbitrary fixed state of the environment appended to the reduced density matrix. The projection operators are idempotent, $\mathcal{P}^2 = \mathcal{P}$ and $\mathcal{Q}^2 = \mathcal{Q}$, sum to the identity, $\mathcal{P} + \mathcal{Q} = \mathcal{I}$, and are commutative, $\mathcal{P}\mathcal{Q} = \mathcal{Q}\mathcal{P} = 0$. Upon applying the projection operators to equation 2.3 we obtain two coupled differential equations for the system and environment, respectively:

$$\begin{aligned} \frac{\partial}{\partial t}\mathcal{P}\hat{\rho}(t) &= \alpha\mathcal{P}\mathcal{L}_{QE}(t)\hat{\rho}(t) \\ &= \alpha\mathcal{P}\mathcal{L}_{QE}(t)\mathcal{P}\hat{\rho}(t) + \alpha\mathcal{P}\mathcal{L}_{QE}(t)\mathcal{Q}\hat{\rho}(t), \end{aligned} \tag{2.11}$$

and

$$\begin{aligned} \frac{\partial}{\partial t}\mathcal{Q}\hat{\rho}(t) &= \alpha\mathcal{Q}\mathcal{L}_{QE}(t)\hat{\rho}(t) \\ &= \alpha\mathcal{Q}\mathcal{L}_{QE}(t)\mathcal{P}\hat{\rho}(t) + \alpha\mathcal{Q}\mathcal{L}_{QE}(t)\mathcal{Q}\hat{\rho}(t). \end{aligned} \tag{2.12}$$

We may solve 2.11 in terms of the solution to 2.12,

$$\mathcal{Q}\hat{\rho}(t) = \mathcal{G}(t,t_0)\mathcal{Q}\hat{\rho}(t_0) + \alpha \int_{t_0}^{t} \mathrm{d}s\, \mathcal{G}(t,s)\mathcal{Q}\mathcal{L}_{QE}(s)\mathcal{P}\hat{\rho}(s), \tag{2.13}$$

where $\mathcal{G}(t_2,t_1)$ contains the non-Markovian effects of the environment from time t_1 to t_2:

$$\mathcal{G}(t_2,t_1) = \mathcal{T}e^{\int_{t_1}^{t_2} \mathrm{d}\tau\, \mathcal{Q}\alpha\mathcal{L}_{QE}(\tau)}. \tag{2.14}$$

Upon inserting this solution into 2.11, we obtain the Nakajima-Zwanzig equation for the reduced system dynamics:

$$\begin{aligned}\frac{\partial}{\partial t}\mathcal{P}\hat{\rho}(t) =& \alpha\mathcal{P}\mathcal{L}_{QE}(t)\mathcal{P}\hat{\rho}(t) + \\ & \alpha\mathcal{P}\mathcal{L}_{QE}(t)\mathcal{G}(t,t_0)\mathcal{Q}\hat{\rho}(t_0) + \\ & \alpha^2 \int_{t_0}^{t} \mathrm{d}s\mathcal{P}\mathcal{L}_{QE}(t)\mathcal{G}(t,s)\mathcal{Q}\mathcal{L}_{QE}(t)\mathcal{P}\hat{\rho}(s).\end{aligned} \tag{2.15}$$

No approximations have been made to derive this equaion, so it provides an exact description of the reduced system dynamics on the qubits only. This equation is generally intractable, and so is not often used for practical calculations. The difficulty lies in the evaluation of the memory kernel, $\mathcal{K}(t,s) = \mathcal{P}\mathcal{L}_{QE}(t)\mathcal{G}(t,s)\mathcal{Q}\mathcal{L}_{QE}(s)$, which often requires further approximations to be made, depending on the noise process under consideration.

2.3 Incoherent Processes

Incoherent noise has been studied extensively in NMR settings, where it is often the dominant noise term [218, 25, 164, 84, 131]. The noise manifests when considering a measurement over an ensemble, either in time or space, where the effective Hamiltonian acting on the qubits varies over some parameter $\vec{\omega}$. The variation leads to a set of unitary propagators, $\{U(\vec{\omega})\}$, with corresponding classical probability distribution, $P(\vec{\omega})$. The superoperator for incoherent noise is calculated as a convex operator sum

over the distribution of unitary operators:

$$\mathcal{S} = \int \mathrm{d}\vec{\omega}\, P(\vec{\omega}) \overline{U}(\vec{\omega}) \otimes U(\vec{\omega}). \tag{2.16}$$

2.4 Stochastic Processes

Stochastic processes cause a time-variation of the qubit Hamiltonian during an experiment and are characterized by a set of multi-point correlation functions, G_n, with associated correlation times, τ_c, that determine how an underlying distribution of noise strengths is sampled over time. In the limiting case of stationary Gaussian noise, which may be described by a single correlation time, the noise effects are fully characterized by specifying the two-point correlation function, $G_2(\tau)$, or the noise power spectral density, $S(\omega)$, which is the Fourier transform of $G_2(\tau)$. A general description is to consider the qubit Hamiltonian to be subject to additive stochastic noise:

$$H(t) = H_Q + H_{st}(t). \tag{2.17}$$

When dealing with a stochastic process, the dynamics are calculated as an average over instances of the noise process. The method we choose to model stochastic noise is based on a cumulant expansion of the stochastic Liouville equation [116]. We assume in the following that the time-dependence of the stochastic noise is parameterized by a fluctuating scalar, $\omega(t)$, multiplying a constant Hamiltonian:

$$H_{st}(t) = \omega(t) H_s. \tag{2.18}$$

We also assume that the fluctuation is zero-mean and the underlying distribution generating the fluctuation is Gaussian and stationary.

As the noise is stochastic, we must take an ensemble average of the propagator over many instances of the noise:

$$\mathcal{S}(t) = \left\langle \mathcal{T} e^{-i \int_0^t \mathrm{d}t' \mathcal{L}(t')} \right\rangle \tag{2.19}$$

where $\mathcal{L}(t) = \overline{H} \otimes I - I \otimes H$ is the Liouvillian noise operator. In order to move the expectation value to the Liouvillian operators, we take a Dyson series of the propagator [55]:

$$\mathcal{S}(t) = \mathbb{I} - i\int_0^t \mathrm{d}t' \langle \mathcal{L}(t') \rangle + \frac{(-i)^2}{2!}\mathcal{T}\int_0^t \mathrm{d}t_1 \int_0^t \mathrm{d}t_2 \langle \mathcal{L}(t_1)\mathcal{L}(t_2) \rangle + ... \tag{2.20}$$

By defining a cumulant function, $K(t)$, we can also write the propagator as:

$$\mathcal{S}(t) = e^{K(t)} = 1 - itK_1(t) + \frac{(-it)^2}{2!}K_2(t) + ... \tag{2.21}$$

We may now equate terms of identical order to obtain the n^{th} order cumulants,

$$K_1(t) = \frac{1}{t}\int_0^t \mathrm{d}t' \langle \mathcal{L}(t') \rangle , \tag{2.22}$$

$$K_2(t) = \frac{1}{t^2}\mathcal{T}\int_0^t \mathrm{d}t_1 \int_0^t \mathrm{d}t_2 \langle \mathcal{L}(t_1)\mathcal{L}(t_2) \rangle - K_1(t)^2. \tag{2.23}$$

We now apply the zero-mean property of $\omega(t)$ to assert that $K_1(t) = 0$ and explicitly apply the time-ordering operator to obtain:

$$K_2(t) = \frac{2}{t^2}\int_0^t \mathrm{d}t_1 \int_0^{t_1} \mathrm{d}t_2 \langle \omega(t_1)\omega(t_2)\mathcal{L}(t_1)\mathcal{L}(t_2) \rangle . \tag{2.24}$$

In the special case where the stochastic portion of the Hamiltonian commutes with the deterministic portion the time-dependence of $\mathcal{L}(t)$ may be dropped and we get:

$$K_2(t) = \frac{2\mathcal{L}^2}{t^2}\int_0^t \mathrm{d}t_1 \int_0^{t_1} \mathrm{d}t_2 \langle \omega(t_1)\omega(t_2) \rangle . \tag{2.25}$$

When the stochastic and deterministic Hamiltonians do not commute we discretize the problem and perform the calculation in the interaction frame of the deterministic Hamiltonian. Equation 2.25 may be written in terms of a two-point correlation function

$$G(t_1 - t_2) = \langle \omega(t_1)\omega(t_2) \rangle , \tag{2.26}$$

to obtain

$$K_2(t) = \frac{2\mathcal{L}^2}{t^2} \int_0^t \mathrm{d}t_1 \int_0^{t_1} \mathrm{d}t_2 G(t_1 - t_2). \tag{2.27}$$

This expression may be further simplified by using the stationary property of the noise, applying a change of variables, and assuming that the behavior of the autocorrelation depends only on the absolute value of the difference between t_1 and t_2 [44]:

$$K_2(t) = 2 \int_0^t d\tau (t - \tau) G(\tau). \tag{2.28}$$

The effect of the noise is now completely defined by the nature of the autocorrelation function, $G(\tau)$. When $G(\tau)$ corresponds to an underlying probability distribution with a finite variance, a single parameter, the correlation time, characterizes the memory of the noise:

$$\tau_c = \frac{1}{G(0)} \int_0^\infty G(\tau)\, \mathrm{d}\tau. \tag{2.29}$$

For general noise, however, the correlation time is often ill-defined and provides little insight into the problem. For stationary noise, the autocorrelation is defined as the inverse Fourier transform of the noise power spectral density:

$$G(\tau) = \int_{-\infty}^{\infty} S(\omega) e^{i\omega\tau}\, \mathrm{d}\tau \tag{2.30}$$

Thus, for noise processes sampled from an underlying Gaussian distribution, the effect of the noise is fully specified by either $S(\omega)$ or $G(\tau)$. The power spectral density may be calculated based on a particular model of the underlying process; for example, motional modulation of a dipolar interaction [20]. However, these calculations are often difficult or inaccurate, requiring the spectral density to be experimentally determined [30]. For general noise processes, the underlying distribution must be fully specified to allow the calculation of a complete set of multi-point correlation functions that may be used to calculate higher-order cumulants.

2.5 Markov Processes

A Markov process is one where the evolution of the system does not depend on a history of any prior evolution; the noise process has no memory and each incremental period of evolution is causally disconnected from every other period. Noise on a quantum system that is due to a Markov process cannot be directly suppressed through control techniques, and leads to dissipative effects that can only be suppressed by the application of quantum error correction. The most commonly used equation of motion governing the dynamics of qubits coupled to a Markovian environment is the *Lindblad equation*:

$$\frac{d\rho}{dt} = -i\left[H^{\text{eff}}, \rho\right] - \frac{1}{2}\sum_k \left(L_k^\dagger L_k \rho + \rho L_k^\dagger L_k\right) + \sum_k L_k \rho L_k^\dagger. \tag{2.31}$$

The first term represent unitary (dissipationless) evolution of the qubits under an effective Hamiltonian, H^{eff}, given by the raw qubit Hamiltonian, H_Q, rewritten in a chosen interaction frame. The remaining terms dictate the non-unitary (dissipative) behavior of the qubit dynamics under the action of Lindblad jump operators, L_k, representing the effect of the environment and derived from a model of the underlying process or specified based on measurement.

Chapter 3

Spin-Based Quantum Information Processing

Physical implementations of quantum information processing based on magnetic resonance of nuclear spins in the liquid state have provided a testbed for quantum control in large Hilbert spaces [43, 42]. The Hamiltonians and noise structure of these systems are generally well-characterized and control methods developed for NMR spectroscopy and imaging may be directly utilized. Many demonstrations of quantum algorithms, quantum error correction, quantum simulation, and control techniques have been performed on liquid-state NMR systems [98], but ultimately the scalability of these systems is limited by both the limited connectivity of the spins and an exponential decrease in signal as more spins are added. While algorithmic cooling techniques may be used to circumvent this signal loss [178, 173], there is still the requirement of finding molecules large enough and with the proper structure to implement more qubits.

Solid-state NMR systems may prove to be more appropriate due to their regular crystal-lattice structure [9, 10]. In addition to being candidates for quantum information processing, these systems provide a natural platform for investigating many-body physics [36] and transport in one-dimensional spin chains, which have been suggested as a means of transferring information between regions (or spatially separated registers) of a quantum processor [3, 168]. The addition of localized free-radical electron

spins provides additional degrees of freedom that offer enhanced purity at convenient temperatures and a way to efficiently remove entropy from the system [145]. Control of a nuclear spin processor via pulsed electron spin resonance manipulation of an electron spin offers intriguing benefits for node-based quantum computing.

3.1 Interaction Hamiltonians for Spin-Based QIP

The interactions important for magnetic resonance of electron and nuclear spins may be categorized in terms of spin interactions with bulk fields, spin interactions between spins of the same type, and spin interactions between spins of different type. Examples of the interactions with bulk fields are the electron and nuclear Zeeman interactions. Examples of same-type spin interactions include exchange couplings and dipole-dipole couplings. Varying-type interactions include the hyperfine coupling between electron and nuclear spins, which is a combination of a dipole-dipole coupling and a Fermi contact exchange interaction. We describe each of these interactions in this section. Further details of these couplings may be found in standard texts on magnetic resonance of electrons and nuclei [1, 187, 179, 5]. In the following the common convention $\hbar = 1$ is used.

In the presence of an externally applied static magnetic field, $\vec{B}_0$, the energy of a nuclear spin, $\vec{I}$, is given by the nuclear Zeeman interaction Hamiltonian:

$$H_{nZ} = -\gamma \vec{B}_0 (1 - \boldsymbol{\sigma}) \vec{I}, \tag{3.1}$$

where γ is the gyromagnetic ratio, a constant whose value is inherent to the particular nucleus in question, and $\boldsymbol{\sigma}$ is the chemical shielding tensor accounting for shielding of the external field by the electron cloud surrounding the nucleus. For an electron spin, $\vec{S}$, in an applied magnetic field, $\vec{B}_0$ a corresponding electron Zeeman interaction Hamiltonian is defined as

$$H_{eZ} = \beta_e \vec{B}_0 \boldsymbol{g} \vec{S}, \tag{3.2}$$

where β_e is the Bohr magneton, and $\boldsymbol{g}$ is the electron g-tensor, the combination of

which give the electron analogue of the nuclear gyromagnetic ratio. For a free electron the g-tensor is isotropic with $g_e = 2.0023$. Deviations of $\boldsymbol{g}$ from the free electron value may be due to a spin-orbit mixing of excited and ground electronic energy levels for bound electrons.

A Heisenberg exchange coupling occurs in systems where the orbitals of two spins overlap, allowing the exchange of the spins between sites. The Hamiltonian for the exchange interaction is given by

$$H_E = \vec{S}_1 \boldsymbol{J} \vec{S}_2, \tag{3.3}$$

where $\boldsymbol{J}$ is the exchange tensor. The same interaction occurs with nuclei, but is mediated by hyperfine coupling to the surrounding electrons. The exchange tensor is generally isotropic and leads to a scalar coupling of the form $J\vec{S}_1 \cdot \vec{S}_2$. However, in some systems, such as transition metal ions, the interaction can be anisotropic [2].

The spin dipolar Hamiltonian emerges from a direct magnetic dipole-dipole interaction between spins

$$H_{dd} = \vec{S}_1 \boldsymbol{D} \vec{S}_2 = \frac{\mu_0}{4\pi} g_1 g_2 \beta_e^2 \left[\frac{3(\vec{S}_1 \cdot \vec{r})(\vec{S}_2 \cdot \vec{r}))}{r^5} - \frac{\vec{S}_1 \cdot \vec{S}_2}{r^3} \right], \tag{3.4}$$

where μ_0 is the permeability of free space and $\vec{r}$ is the spatial vector between the two spins. A similar Hamiltonian exists for nuclear spins with the electron g-factor and Bohr magneton replaced by the respective nuclear gyromagnetic ratios. The hyperfine coupling between electron and nuclear spins originates from a dipolar coupling of this form and an isotropic Fermi contact term

$$H_F = \frac{2}{3} \mu_0 g_e \beta_e \gamma_n \left| \psi_0(0) \right|^2, \tag{3.5}$$

where $\left|\psi_0(0)\right|^2$ is the density of the electron wavefunction at the site of the nucleus. The general hyperfine interaction Hamiltonian is

$$H_{hf} = \vec{S} \boldsymbol{A} \vec{I}, \tag{3.6}$$

where $\boldsymbol{A}$ is the hyperfine interaction tensor.

3.2 Electron-Nuclear Actuator-Based QIP

Systems composed of electron and nuclear spins have been studied extensively for use in quantum information processing, including organic free radical molecules in the solid state [143, 146, 147, 82], defect nuclear spins in silicon [155], and lattice carbon and nitrogen spins in nitrogen-vacancy center defects in diamond [95, 96]. These proposals often rely on using both electron and nuclear spins as qubits, with electron spin operations applied using microwave frequencies and nuclear spin operations applied using radio frequencies. The drawback of this method is that performing nuclear spin operations directly with radio frequencies limits achievable Rabi frequencies (related to the required gate time) to the order of kilohertz. Recently, Jonathan Hodges and Jamie Yang demonstrated that electron spins could be used as a dedicated actuator element to perform quantum operations on a nuclear spin register, coupled to the electron via an anisotropic hyperfine interaction, with Rabi frequencies of order megahertz [86].

To demonstrate their concept of electron-actuator based control we consider a one electron, one nuclear (1e-1n) spin system in a strong external magnetic field $\vec{B_0} = B_0\hat{z}$ with an anisotropic hyperfine interaction coupling the two spins. We assume a drift Hamiltonian of the form

$$H_d = \frac{1}{2}\omega_z^e\sigma_z^e + \frac{1}{2}\omega_z^n\sigma_z^n + \frac{1}{4}\omega_{zz}\sigma_z^e\sigma_z^n + \frac{1}{4}\omega_{zx}\sigma_z^e\sigma_x^n, \tag{3.7}$$

where ω_z^e and ω_z^n are the strengths of the electron and nuclear Zeeman interactions, respectively, with the static field, and ω_{zz} and ω_{zx} are isotropic and anisotropic components of the hyperfine interaction. The electron Zeeman interaction is dominant and defines the principle coordinate system of spin quantization. In terms of this coordinate system, the eigenstates of the nuclear spins are given by the vector sum of the nuclear Zeeman interaction and the spin dependent local field generated by the

anisotropic hyperfine coupling to the electron:

$$\begin{aligned}
|1\rangle &= |\uparrow \alpha_0\rangle = \sin\theta_\uparrow |\uparrow\uparrow\rangle + \cos\theta_\uparrow |\uparrow\downarrow\rangle , \\
|2\rangle &= |\uparrow \alpha_1\rangle = \cos\theta_\uparrow |\uparrow\uparrow\rangle - \sin\theta_\uparrow |\uparrow\downarrow\rangle , \\
|3\rangle &= |\downarrow \beta_1\rangle = \cos\theta_\downarrow |\downarrow\uparrow\rangle - \sin\theta_\downarrow |\downarrow\downarrow\rangle , \\
|4\rangle &= |\downarrow \beta_0\rangle = \sin\theta_\downarrow |\downarrow\uparrow\rangle + \cos\theta_\downarrow |\downarrow\downarrow\rangle ,
\end{aligned} \tag{3.8}$$

where $\theta_\uparrow$ and $\theta_\downarrow$ determine the non-commutativity of the resulting eigenstates and are given by:

$$\begin{aligned}
\theta_\uparrow &= \tan^{-1}\left(\frac{-\omega_{zx}}{\omega_{zz} - \omega_z^n}\right) , \\
\theta_\downarrow &= \tan^{-1}\left(\frac{-\omega_{zx}}{\omega_{zz} + \omega_z^n}\right) .
\end{aligned} \tag{3.9}$$

Due to the non-commutativity of the local fields seen by the nuclear spin when the electron spin is in the spin-up versus spin-down state, universal control over the entire spin system (generalizing to 1e-Nn systems) may be achieved by implementing only the electron σ_x^e generator and allowing free evolution under H_d [86]. This may also be seen by noting that the transition probability between any pair of non-degenerate states associated with the σ_x^e operation is non-zero [87]. We may thus use the nuclear spins as a quantum processor, with the electron spin acting as an actuator element to allow for fast quantum operations on the processor [86, 227].

3.3 Multi-Node Designs

A distributed, multi-node structure has been suggested as a convenient means of arranging qubits in an experimentally realizable quantum computer architecture [145, 197, 204, 128, 104, 109, 97, 33]. Such a structure requires the ability to define an array of disjoint quantum processors that may be controlled locally, with communication between local processors provided by a coupling between nodes that may be turned on or off in turn. One method of satisfying these requirements is to append a small

number of qubits to each node of a two-dimensional array of nearest-neighbor coupled actuator elements. The actuator elements provide local control of the surrounding processor qubits and a means of transferring information between nodes via isotropic actuator couplings [23, 17].

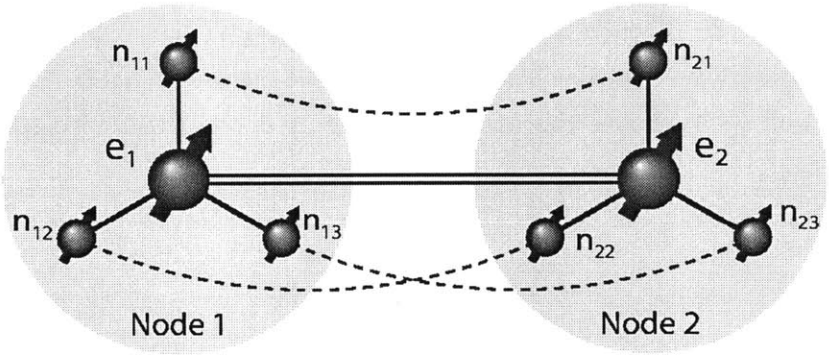

Figure 3-1: Schematic of a 2×(1e-3n) node structure. The nodes are taken to be identical, with resolved anisotropic hyperfine interactions (solid red lines) between electron actuator spins and nuclear processor spins. The local processors are initially disjoint, but may be effectively coupled (dotted lines) by modulating an isotropic actuator exchange interaction (solid blue double line) and moving into an appropriate microwave Hamiltonian interaction frame. The spin labeling is e_i for electron actuator spins and n_{ij} for nuclear processor spins, where i labels the nodes and j labels the qubits.

The details of this structure will be discussed from the standpoint of a spin-based quantum information processor. This system contains all the necessary physics and is representative of many other modalities being considered for experimental realizations of quantum information processing. For example, Rydberg atom excitations of neutral atoms [94, 175], inductive coupling of superconducting qubits [135, 136], and Bloch wave dispersion in cavity devices [54, 189] all take the form of an isotropic dipolar coupling. Direct dipolar interactions also naturally occur in spin-based devices such as semiconductor quantum dots [132, 160], silicon-based devices [104, 155], nitrogen-vacancy defect centers in diamond [223], and other solid-state spin systems [11, 197, 80]. The methods discussed may be readily extended to these systems.

In our spin-based model, each node consists of a single actuator electron spin coupled via resolved anisotropic hyperfine interactions to each of k qubits of a local nuclear spin processor (Fig. 3-1). Control over the local processors is achieved via

electron-only modulation [87], taking advantage of the relative strength of the hyperfine interaction to generate a universal set of fast quantum gates on the nuclear spins [86], which serve as good qubits due to their relatively long coherence times [198]. We require that the differences in the hyperfine coupling strengths within each node are large enough for each pair of identical spins to be spectroscopically resolved, limiting the number of qubits per node [33]. However, due to the inherent inefficiency of designing control sequences for a large number of particles, it may be advantageous to keep the size of nodes relatively small (of order 20 - 30 spins) and rely on the ability to swap qubit states between nodes to implement large-scale quantum algorithms. The internode coupling of actuators is given by an isotropic dipolar or exchange interaction between electrons, with the spatial separation of the nodes taken to be sufficiently large for any cross-node dipolar interactions of nuclear spins to be small enough to be simply refocused.

Universal control over the entire $2\times$(1e-kn) system is obtained by adding a term to the Hamiltonian that spatially labels the nodes to allow for local operations. For example, a constant 2D field gradient could be applied to add a position dependence to the electron spin Zeeman frequency [190]. Pulses may then be designed with a frequency selectivity corresponding to a single node [113]. In practice, the presence of a constant field gradient during control pulses introduces additional noise to the spin system. Alternatively, a pulsed gradient field may be applied at the start of any computation to allow the initialization of a subset of the nuclear spins into an eigenstate, such that they act as classical bits. The effective hyperfine field associated with each eigenstate modifies the local field seen by the actuator, labeling the node by the modified electron Zeeman frequency.

Chapter 4

Efficient Information Transfer In a Multi-Node Quantum Information Processor

In this chapter we describe a method for coupling disjoint qubits in neighboring processing nodes of a distributed node quantum information processor. An effective channel for information transfer between nodes is obtained by moving the system into an interaction frame where all pairs of cross-node qubits are effectively coupled via an exchange interaction between actuator elements of each node. All control is achieved via actuator-only modulation, leading to fast implementations of a universal set of internode quantum gates. The method is expected to be nearly independent of actuator decoherence and may be made insensitive to experimental variations of system parameters by appropriate design of control sequences. We show, in particular, how the induced cross-node coupling channel may be used to swap the complete quantum states of the local processors in parallel.

4.1 Creating An Effective Cross-Node Processor Coupling

An effective cross-node processor coupling network is created by taking advantage of four-body coupling terms between actuator and processor elements that appear in a manifold of excited states unused for quantum information storage. By moving into an appropriate interaction frame, the four-body coupling terms appear as two-body couplings between every pair of cross-node processor qubits in a properly defined computational manifold. While this complete cross-node coupling network allows for a computationally universal set of operations between nodes, we present an explicit implementation of a parallel swap of the complete quantum mechanical states of two local quantum processors. Consideration of this representative entangling operation serves to motivate the broader applicability of the induced information transfer channel. Additionally, since information is never explicitly stored for an appreciable amount of time on the actuators – which are exposed to higher levels of noise than the processor elements – we expect the channel to be nearly independent of actuator decoherence.

The state structure of a two node system with one electron actuator spin and one nuclear processor spin each – a 2×(1e-1n) system – is shown in Fig. 4-1. The computational basis states of the local quantum processors are defined in the ground-state manifold of the actuators. This choice of encoding allows us to implement gates between the disjoint processors by taking advantage of an induced cross-node coupling in the zero-quantum (ZQ) manifold of actuator excited states not used for information storage.

To derive the general form of the cross-node coupling we consider a 2×(1e-kn) system. The nodes are taken to be identical with energy structure given by a dominant, quantizing electron Zeeman interaction, $H_{\mathrm{Z}}^{\mathrm{e}}$, with a strong static magnetic field oriented along the laboratory $\hat{z}$ direction; a corresponding nuclear Zeeman interaction, $H_{\mathrm{Z}}^{\mathrm{n}}$; an anisotropic hyperfine interaction between electron and nuclear spins, $H_{\mathrm{HF}}^{\mathrm{e-n}}$;

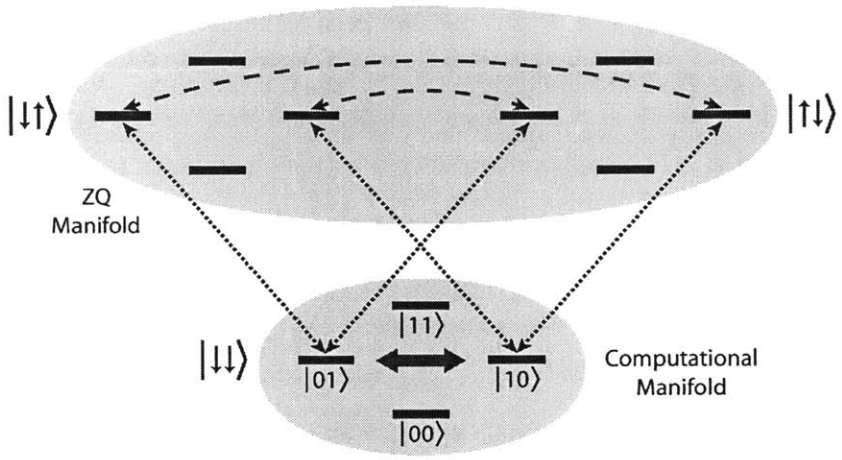

Figure 4-1: The energy level structure of a 2×(1e-1n) system. Quantum information is encoded in the states $|{\downarrow\downarrow}\,00\rangle$, $|{\downarrow\downarrow}\,01\rangle$, $|{\downarrow\downarrow}\,10\rangle$, and $|{\downarrow\downarrow}\,11\rangle$ of the actuator ground-state (Computational) manifold, where arrows indicate electron actuator spin states and binary digits indicate nuclear processor spin states. The desired transition (bold red arrow) for a SWAP operation is implemented by applying a selective microwave field that induces transitions between the two manifolds (dotted lines), effectively moving the induced cross-node processor transitions (dashed lines) in the actuator zero-quantum (ZQ) manifold to the Computational manifold. Note that the actuator excited state manifold, $|{\uparrow\uparrow}\rangle$, is not included as it is not involved in the internode transfer process.

and a dipolar interaction between electron spins, $H_{\mathrm{D}}^{\mathrm{e-e}}$:

$$H^{2\mathrm{e}\text{-}k\mathrm{n}} = H_{\mathrm{Z}}^{\mathrm{e}} + H_{\mathrm{Z}}^{\mathrm{n}} + H_{\mathrm{HF}}^{\mathrm{e-n}} + H_{\mathrm{D}}^{\mathrm{e-e}}. \tag{4.1}$$

In a frame rotating at the electron Zeeman frequency, the resulting secular Hamiltonians are given in terms of the usual spin-$\frac{1}{2}$ Pauli operators as [1]

$$\begin{aligned} H_{\mathrm{Z}}^{\mathrm{n}} &= \sum_k \omega_z^k \left(\sigma_z^{\mathrm{n}_{1k}} + \sigma_z^{\mathrm{n}_{2k}}\right) \\ H_{\mathrm{D}}^{\mathrm{e-e}} &= \omega_d \left(2\sigma_z^{\mathrm{e}_1}\sigma_z^{\mathrm{e}_2} - \sigma_x^{\mathrm{e}_1}\sigma_x^{\mathrm{e}_2} - \sigma_y^{\mathrm{e}_1}\sigma_y^{\mathrm{e}_2}\right) \\ H_{\mathrm{HF}}^{\mathrm{e-n}} &= \sum_k \vec{A^k} \cdot (\sigma_z^{\mathrm{e}_1}\vec{\sigma}^{\mathrm{n}_{1k}} + \sigma_z^{\mathrm{e}_2}\vec{\sigma}^{\mathrm{n}_{2k}}), \end{aligned} \tag{4.2}$$

where the vectors $\vec{A^k} = A_x^k\hat{x} + A_y^k\hat{y} + A_z^k\hat{z}$ represent the strengths and directions of the hyperfine coupling between the kth nuclear spin in each node and the corresponding

actuator, ω_z^k is the strength of the nuclear Zeeman interaction for the kth nuclear spin, ω_d is the strength of the dipolar interaction, and $\vec{\sigma} = \sigma_x\hat{x} + \sigma_y\hat{y} + \sigma_z\hat{z}$.

The full set of interactions accessible by evolution under the Hamiltonians in (4.2) is given by the Lie algebra generated by taking Lie brackets to all orders [167, 177]. In particular, the second-order bracket, $[[H_{\mathrm{D}}^{\mathrm{e-e}}, H_{\mathrm{HF}}^{\mathrm{e-n}}], H_{\mathrm{HF}}^{\mathrm{e-n}}]$, takes the form of a four-body inter-node interaction, given by an effective cross-node nuclear spin dipolar coupling, $H_{\mathrm{D}}^{\mathrm{n-n}}$, along with flip-flop transitions of the electron spins:

$$[[H_{\mathrm{D}}^{\mathrm{e-e}}, H_{\mathrm{HF}}^{\mathrm{e-n}}], H_{\mathrm{HF}}^{\mathrm{e-n}}] \propto \omega_d \left(\sigma_+^{\mathrm{e}_1}\sigma_-^{\mathrm{e}_2} + \sigma_-^{\mathrm{e}_1}\sigma_+^{\mathrm{e}_2}\right) \otimes H_{\mathrm{D}}^{\mathrm{n-n}}. \tag{4.3}$$

The resulting nuclear spin dynamics in the ZQ manifold may be decomposed into a sum of coupling terms, $H_{\mathrm{D}}^{\ell m}$, that act on every pair of cross-node spins, $\mathrm{n}_{1\ell}$ and n_{2m} (Fig. 4-2). Each $H_{\mathrm{D}}^{\ell m}$ may be written in terms of the well-known dipolar alphabet, with $\sigma_\pm = \sigma_x \pm i\sigma_y$ [1]:

$$\tilde{A}_{\ell m} = A_z^\ell A_z^m \left(\sigma_z^{\mathrm{n}_{1\ell}}\sigma_z^{\mathrm{n}_{2m}}\right) \tag{4.4a}$$

$$\begin{aligned}\tilde{B}_{\ell m} = &\left(A_x^\ell A_x^m + A_y^\ell A_y^m\right)\left(\sigma_+^{\mathrm{n}_{1\ell}}\sigma_-^{\mathrm{n}_{2m}} + \sigma_-^{n_{1\ell}}\sigma_+^{n_{2m}}\right) \\ &+ \left(A_x^\ell A_y^m - A_y^\ell A_x^m\right)\left(\sigma_+^{\mathrm{n}_{1\ell}}\sigma_-^{\mathrm{n}_{2m}} - \sigma_-^{\mathrm{n}_{1\ell}}\sigma_+^{\mathrm{n}_{2m}}\right)\end{aligned} \tag{4.4b}$$

$$\begin{aligned}\tilde{C}_{\ell m} = &\left(A_x^\ell A_z^m - iA_y^\ell A_z^m\right)\left(\sigma_+^{\mathrm{n}_{1\ell}}\sigma_z^{\mathrm{n}_{2m}} + \sigma_z^{\mathrm{n}_{1\ell}}\sigma_+^{\mathrm{n}_{2m}}\right) \\ &+ \left(A_z^\ell A_x^m - A_z^\ell A_z^m - iA_z^\ell A_y^m + iA_y^\ell A_z^m\right)\sigma_z^{\mathrm{n}_{1\ell}}\sigma_+^{\mathrm{n}_{2m}}\end{aligned} \tag{4.4c}$$

$$\tilde{E}_{\ell m} = \left(A_x^\ell A_x^m - A_y^\ell A_y^m - iA_x^\ell A_y^m - iA_y^\ell A_x^m\right)\sigma_+^{\mathrm{n}_{1\ell}}\sigma_+^{\mathrm{n}_{2m}} \tag{4.4d}$$

$$\tilde{D}_{\ell m} = \tilde{C}_{\ell m}^\dagger, \tilde{F}_{\ell m} = \tilde{E}_{\ell m}^\dagger. \tag{4.4e}$$

After application of an appropriate microwave control field, these four-body interactions in the ZQ manifold appear as effective cross-node two-body couplings in the computational manifold. To demonstrate this, we consider the implementation of a particularly powerful operation: a parallel swap of entire local processor states between nodes at once. For the case of a single nuclear spin per node, the relevant ZQ transitions are $|\uparrow\downarrow 01\rangle\langle\downarrow\uparrow 10|$ and $|\uparrow\downarrow 10\rangle\langle\downarrow\uparrow 01|$. Application of a microwave field with matrix elements $|\uparrow\downarrow\rangle\langle\downarrow\downarrow|$ and $|\downarrow\uparrow\rangle\langle\downarrow\downarrow|$ of strength commensurate with the ZQ

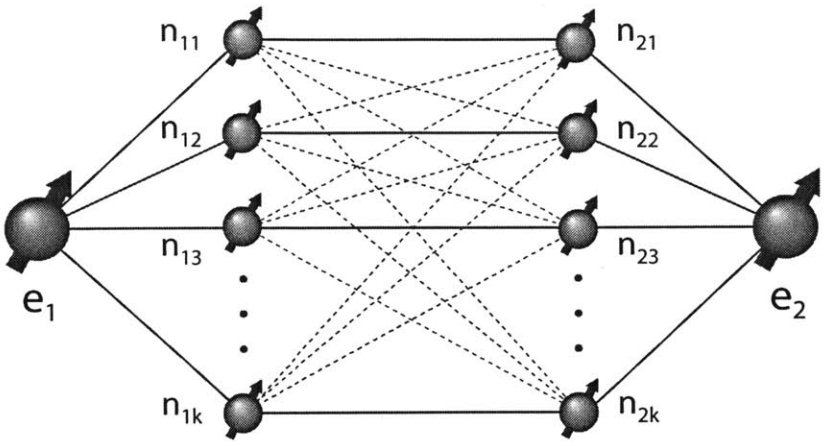

Figure 4-2: The induced coupling network of local processor elements consists of interactions between every pair of cross-node spins. For implementation of a parallel swap operation, we wish to keep interactions between identical spins (solid red lines) while refocusing all other interactions (dotted lines).

transitions transforms both of the transitions to a swap operation in the computational manifold: $|\downarrow\downarrow 01\rangle \langle\downarrow\downarrow 10|$ (See Fig. 4-1).

4.2 Implementing a Parallel Swap Operation

When multiple nuclear spins are present in each node, a parallel swap operation requires suppressing couplings between non-identical spins ($\ell \neq m$) while retaining couplings between identical spins ($\ell = m$). This may be accomplished by exploiting the difference in symmetry between the prefactors of the coupling operators for identical versus non-identical spins.

Consider, as an example, a 2×(1e-2n) system. The effective Hamiltonians of the induced interactions may be written as $H_{\mathrm{D}}^{\shortparallel} + H_{\mathrm{D}}^{\times}$, where $H_{\mathrm{D}}^{\shortparallel} = H_{\mathrm{D}}^{11} + H_{\mathrm{D}}^{22}$ and $H_{\mathrm{D}}^{\times} = H_{\mathrm{D}}^{12} + H_{\mathrm{D}}^{21}$. The effective dipolar coupling strength for $H_{\mathrm{D}}^{\times}$ appears as odd order in $\vec{A}^1$ and $\vec{A}^2$, while each term in $H_{\mathrm{D}}^{\shortparallel}$ appears as even order. Thus, by inverting the state of only the second (or first) spin in each node halfway through free evolution under the induced Hamiltonians, we can generate a zeroth-order average Hamiltonian of only the desired $H_{\mathrm{D}}^{\shortparallel}$ interactions [77]. Higher order terms in the average Hamiltonian may be

suppressed through the use of more sophisticated pulses or by applying the evolution-pulse-evolution cycle at a rate fast compared to ω_D. This symmetry argument may be easily generalized to a larger number of nuclear spins per node by applying a binomially expanding set of inversion pulses to properly select the desired couplings [99].

We now consider how to isolate the desired interaction (4.3) from other elements of the algebra. One method of suppressing the extraneous terms is to use a composite pulse sequence to generate an effective Hamiltonian for which the desired second order commutator is the dominant term. Concretely, recall that by the BCH expansion, $e^X e^Y = \exp(X + Y + \frac{1}{2}[X,Y] + \frac{1}{12}[X,[X,Y]] + \frac{1}{12}[Y,[Y,X]] + \cdots)$. By recursively applying this expansion, we can derive an identity that suppresses all terms below second order:

$$e^X e^Y e^{-X} e^{-Y} e^{-X} e^Y e^X e^{-Y} = e^{[X,[X,Y]]+\cdots}. \tag{4.5}$$

By making the correspondence $X = H_{\mathrm{HF}}^{\mathrm{e-n}}$ and $Y = H_{\mathrm{D}}^{\mathrm{e-e}}$, we obtain a pulse composed of sequential periods of only electron dipolar or hyperfine evolution, leading to the effective propagator,

$$U(8\tau) \approx e^{i\tau^3[[H_{\mathrm{D}}^{\mathrm{e-e}},H_{\mathrm{HF}}^{\mathrm{e-n}}],H_{\mathrm{HF}}^{\mathrm{e-n}}]}, \tag{4.6}$$

where higher-order terms have been neglected. We may also suppress the undesired terms by numerically optimizing experimentally robust microwave pulses which achieve the desired interaction while suppressing all other interactions [61, 42, 105, 24].

4.3 Robustness to Actuator Noise

A final consideration is the sensitivity of the induced channel to actuator noise processes. We claim that by never transferring complete qubit state information to the actuators, we may operate in a regime where any portion of the information present in the ZQ manifold arrives back to the computational manifold before it is corrupted. We may quantitatively determine the robustness of the channel to actuator noise by comparing, as a function of noise strength, the Hilbert-Schmidt inner product fidelity,

$F(\hat{\hat{S}}_{\text{ideal}}, \hat{\hat{S}}_{\text{noisy}}) = \text{Tr}(\hat{\hat{S}}^{\dagger}_{\text{ideal}} \hat{\hat{S}}_{\text{noisy}})/d^2$, between d^2 dimensional superoperators representing the channel in the presence of noise, $\hat{\hat{S}}_{\text{noisy}}$, and in the ideal noiseless case, $\hat{\hat{S}}_{\text{ideal}}$.

The ideal channel is generated by a Liouvillian operator, $\hat{\hat{L}}$, corresponding to unitary evolution only. The noisy channel includes two dissipation operators, $\hat{\hat{D}}_1$ and $\hat{\hat{D}}_2$, describing the relaxation of e_1 and e_2, respectively:

$$\hat{\hat{S}}_{\text{noisy}}(t) = e^{-it\hat{\hat{L}}+t\hat{\hat{D}}_1+t\hat{\hat{D}}_2}. \tag{4.7}$$

A physically motivated model of noise is a contribution of phase and amplitude damping applied seperately to each electron, which leads to a dissipator,

$$\begin{aligned} \hat{D} = \quad & -\frac{1}{2}(\Gamma_1 + \Gamma_2)(E_- \otimes \mathbb{1} + \mathbb{1} \otimes E_-) \\ & + \Gamma_1 \sigma_+ \otimes \sigma_+ + \Gamma_2 E_- \otimes E_-, \end{aligned} \tag{4.8}$$

where $E_+ = |0\rangle\langle 0|$ and $E_- = |1\rangle\langle 1|$ are projection operators. The noise strength is parameterized by $\Gamma_{1,2}$, which are related to the commonly used energy, T_1, and coherence, T_2, relaxation times by $\Gamma_1 = 1/T_1$ and $\Gamma_2 = (2T_1 - T_2)/(T_1 T_2)$. A plot of the superoperator fidelity versus noise strength is shown in Fig. 4-3. The noise has a minimal effect on the operation of the channel for values of $T_1\omega_1 \gtrsim 10^4$. Assuming a modest Rabi frequency of $\omega_1 = 100$ MHz, actuator relaxation times of 100 μs are required to avoid significant corruption of the information during transfer. Currently achievable relaxation times for electron spins are well within this range [155, 83].

4.4 Discussion

By taking advantage of the additional degrees of freedom present in an actuator based system, and manipulating the naturally occuring actuator interactions between nodes, we were able to create an effective channel between initially disjoint local processors that allows the parallel transfer of k-qubit states between nodes, effectively independent of actuator decoherence. The channel takes the form of four-body cross-node

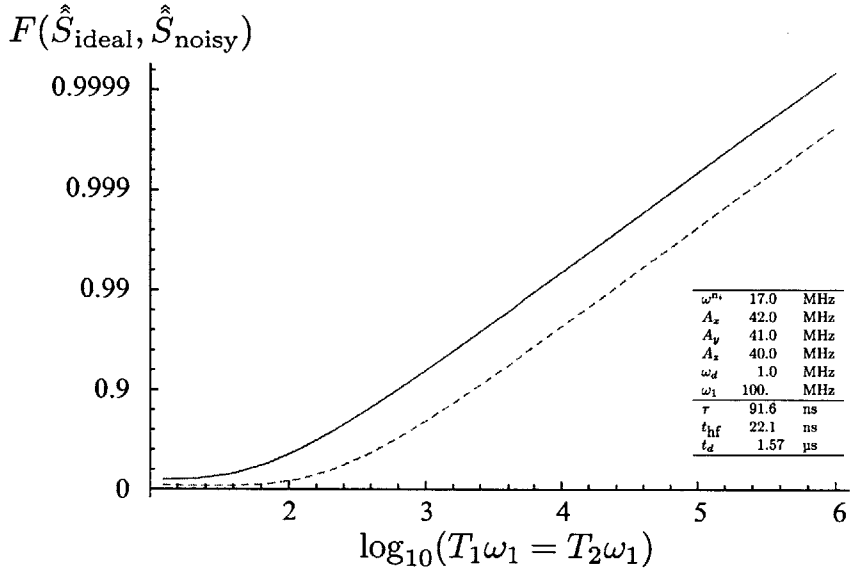

Figure 4-3: A plot of the channel fidelity, F, as a function of noise strength, $T_1 = T_2$, scaled by computing $-\log[1 - F]$. The induced channel (solid line) performs significantly better than a serial swap operation (dotted line). Given a modest Rabi frequency, $\omega_1 = 100$ MHz, the induced channel is nearly independent of actuator decoherence for electron relaxation times above 100 μs.

interactions in the zero-quantum manifold of actuator states which, after moving into an appropriate microwave interaction frame, appear as effective two-body couplings of cross-node qubits in the computational manifold. The resulting complete cross-node coupling network may be used to generate a universal set of gate operations between nodes. We expect these techniques to be applicable to a wide-variety of quantum devices, with minimal need for modification.

Chapter 5

Designing Control Sequences to Implement Robust Quantum Gates

When considering the design of a control sequence to implement a quantum gate, we must first consider what criteria the gate should satisfy. First and foremost, the gate should perform a desired unitary operation with high-fidelity. This implies that the controls should be directly optimized to not only perform the target unitary robustly over uncertainty in the qubit drift and control Hamiltonians, but also decouple the environment over the course of the gate to reduce dissipative effects. The second condition is that gates should be composable to ensure that any gate-dependent errors do not accumulate and correlate over the course of a quantum computation. Composability is normally defined over a continuous process, but may be stated for a discrete gate set as requiring the same quantum map over all instances of the noise. This condition is satisfied if the environment is decoupled, such that the gate action is unitary, or if the effect of the environment appears as a Markov process on the qubits under the action of memory-less Lindblad operators (Section 2.5). A final condition is that any errors in the gate be well-described by a Pauli channel (Section 2.1.3). This condition is not strictly necessary, but permits efficient simulations of the action of multiple gates and is convenient for the development of logical qubit encodings to suppress the errors (Section 7.4). In this chapter we describe how optimal control theory techniques may be used to optimize control pulses that perform a high-

fidelity unitary operation in the absence of dissipation, and demonstrate how strong modulation techniques may be used to suppress non-Markovian noise in the system.

5.1 Optimizing for a Target Unitary Operation

In the absence of dissipative processes, control sequence design simplifies to optimizing a time-dependent Hamiltonian, $H(t)$, such that the action of the Hamiltonian on a general quantum state, ρ, yields the desired dynamics, as governed by the Liouville-von Neumann equation,

$$\frac{d\rho}{dt} = -\frac{i}{\hbar}\left[\rho, H(t)\right]. \tag{5.1}$$

As is common practice for dynamical calculations, we will use the convention $\hbar = 1$ for the remainder of this work. The formal solution of this equation may be written as

$$\rho(t) = U(t)\rho(0)U^{\dagger}(t), \tag{5.2}$$

where $U(t)$ is a unitary propagator representing time evolution under the applied Hamiltonian:

$$U(t) = \mathcal{T}e^{-i\int_0^t H(s)\,ds}, \tag{5.3}$$

where $\mathcal{T}$ is the Dyson time-ordering operator accounting for non-commutivity of $H(t)$ with time. For the control sequences considered in the remainder of this work, we are interested in finding a time-dependent Hamiltonian that accurately implements a desired unitary operation, U_{d}. The notion of accuracy for unitary operations is quantified by defining an appropriate performance functional, such as the average gate fidelity for Hilbert space dimension D:

$$\Phi(U_{\mathrm{d}}, U_{\mathrm{pulse}}) = \left|\langle U_{\mathrm{d}}|U_{\mathrm{pulse}}\rangle\right|^2 = \frac{\left|\mathrm{Tr}\left[U_{\mathrm{d}}^{\dagger}U_{\mathrm{pulse}}\right]\right|^2}{2^D}. \tag{5.4}$$

This performance functional has been shown to be equivalent to the average state fidelity over a complete set of input states [61] and guarantees the desired evolution over all possible input states when Φ is close to unity.

The set of unitary operations that may be generated depends on the form of the accessible physical interactions present in a given system. These interactions are commonly separated into drift Hamiltonian terms, H_d, that are time-independent, and control Hamiltonian terms, $H_c(t)$, that may be varied during the course of an experiment. We parameterize the control Hamiltonians into a set of constant Hamiltonians, $\{H_k\}$, for which we may independently vary amplitudes, $u_k(t)$, to yield a total system Hamiltonian of

$$H(t) = H_d + \sum_k u_k(t) H_k. \tag{5.5}$$

To avoid having to evaluate a set of time-ordered exponentials to solve (5.3), it is common practice to discretize the time-dependence of the control amplitudes into N intervals of length t_j, such that the unitary propagator for a time $T = \sum_{j=1}^{N} t_j$ may be formally expressed as a product of time-independent exponentials:

$$U(T) = \prod U_j = \prod_{j=1}^{N} e^{-i(H_d + \sum_k u_k^j H_k)t_j}. \tag{5.6}$$

This decomposition assumes no reactance in the controls. Control in the presence of finite reactance is discussed in Chapter 8. For the sake of simplicity, we will assume $t_j = \Delta t$ for all j. The validity of this time-slicing method of propagator evaluation depends on the chosen value of Δt, with accuracy increasing for smaller time discretization intervals. With all time-dependence effectively removed from the problem, the control objective now simplifies to determining the set of constant amplitudes, $\{u_k^j\}_{j=1}^{N}$, which maximize the value of the average gate fidelity (5.4).

The fundamental control pulse is a simple square pulse, corresponding to setting $u_k(t)$ to a constant value for some pulse time, with a value of zero otherwise. For a closed quantum system, square pulses would be all the control required to perform quantum computation. However, for open quantum systems, more advanced pulse techniques are required. This may be seen by considering the effect of incoherent noise (Section 2.3) on a square pulse, such as static and control field inhomogeneities. In the absence of inhomogeneities, the effective rotation due to a square pulse is simply about

the axis the pulse is applied. However, in the presence of static field inhomogeneity, the effective rotation axis is tipped toward the quantization axis leading to a rotation that deviates from the desired one. Square pulses only effectively rotate spins that deviate from the Larmor condition by less than the amplitude of the pulse. When control field inhomogeneities are taken into account, the pulse performance is further degraded [92].

5.1.1 Optimal Control Theory

It is well known that better compensation for incoherent noise processes may be achieved by using composite pulses [124], adiabatic pulses [12, 118, 47, 67], and shaped pulses [64]. These pulses achieve superior performance by increasing the number of degrees of freedom of the pulse shape. As noted previously [188], the most general pulse possible is simply a list of amplitudes and phases that do not necessarily adhere to a simple functional form. However, optimizing a general waveform can be challenging, especially for long waveforms with a corresponding large parameter space. A simulated annealing algorithm has been successfully applied to the design of pulses containing many periods of amplitude and phase variation [64, 68]. Convergence was achieved by reducing the number of degrees of freedom of the pulse shape by representing the waveform as a sum of Fourier components. Optimal control theory (OCT) techniques based on gradient search algorithms have proven exceptionally useful to efficiently find solutions in a large parameter space [40, 140, 171, 185]. OCT is a well-established method to determine locally optimal solutions in a multivariate space, subject to a cost-functional [163, 176, 102, 162]. Although these solutions correspond to local optima, these pulses have been demonstrated to yield excellent results and have found application in both nuclear [184, 186] and electron [86] magnetic resonance.

OCT is an important tool for the design of precise control sequences and has emerged as the method of choice for optimizing arbitrary unitary dynamics. The relevance of OCT to magnetic resonance has been well-established [40, 140, 171, 70]. A significant advantage of using OCT techniques is the flexibility of the method.

It allows addressing unique requirements and constraints in individual experimental situations. This is accomplished by redefining the measures of pulse performance. In general, one pulse will not ideally suit the needs of all applications. The versatility of OCT lies in the ease with which various performance functionals and constraints may be substituted into the optimization procedure without requiring a change to the general optimization methods.

5.1.2 Implementation of Optimal Control

The efficient GRadient Ascent Pulse Engineering (GRAPE) OCT algorithm [105] has been used extensively in spin-based implementations of quantum information processing (see [84, 174, 156] for example applications of the GRAPE algorithm). The relative efficiency of the GRAPE algorithm is derived from the need to only compute the propagator corresponding to each time step, U_j, a single time at each iteration of the optimization. The resulting single iteration propagators are then used to calculate both the value of the performance functional and an approximation of gradients used for pulse updating. The truncation of the gradients is valid when Δt is chosen to be significantly smaller than the inverse magnitude of the system Hamiltonian. Approximating the gradients in this way avoids the use of finite-differencing and other inefficient methods of computing the gradients.

In the notation of [105], and in the absence of reactance, the average gate fidelity and corresponding gradients to first order in Δt are

$$\Phi = |\langle U_{\rm d}|U_{\rm pulse}(T)\rangle|^2 = \langle P_j|X_j\rangle \langle X_j|P_j\rangle \tag{5.7}$$

and

$$\frac{\delta\Phi}{\delta u_k^j} = -2\mathrm{Re}\left[\langle P_j|i\Delta t H_k X_j\rangle \langle X_j|P_j\rangle\right], \tag{5.8}$$

where $P_j = U_{j+1}^\dagger ... U_N^\dagger U_d$ and $X_j = U_j ... U_1$ are the backward and forward representations, respectively, of the total pulse propagator at the $j^{\rm th}$ time interval.

The control amplitudes at optimization iteration n, $u_k^j(n)$, are updated according

to

$$u_k^j(n) = u_k^j(n-1) + \epsilon \frac{\delta \Phi}{\delta u_k^j(n-1)}, \tag{5.9}$$

where ϵ is an adjustable scaling factor for the gradients to prevent hindering algorithm convergence by making large deviations in the control parameters between iterations. The algorithm proceeds as follows:

1. An initial set of control parameters is defined: $\{u_k^j\}_{j=1}^N(0)$
2. The piecewise constant propagators for each time-step are calculated: U_j
3. The value of the performance functional is calculated: Φ
4. If $\Phi \geq \Phi_{\text{targ}}$ the algorithm exits, otherwise the gradients for each time-step and control are calculated: $\frac{\delta \Phi}{\delta u_k^j}$
5. A line-search is used to optimize the step size, ϵ, in the gradient direction
6. The control parameters are updated according to (5.9)
7. Loop to Step 2

A detailed derivation of the gradients, including finite reactance in the controls, is given in Appendix A.

5.2 Strongly Modulating Quantum Gates

To suppress non-Markovian noise in the environment, we present a protocol for constructing quantum gates based on periods of strong modulation interspersed with periods of free evolution. This protocol permits universal control of the quantum system while providing robustness to environmental couplings not directly included in numerical optimizations of gates. The use of strongly modulating pulses permits effective decoupling of the qubits and a non-Markovian environment, such that the qubit dynamics are composable over the gate.

5.2.1 Waugh's Decoupling Criteria

The definitive treatment of the criteria for decoupling in magnetic resonance was given by Waugh [217]. He considered a system of two spins-1/2, labeled as I and S, coupled via an Ising interaction. The I spin, representing the environment, is decoupled by an applied drive while the S spin, representing the qubit, free-induction decay (FID) is observed. The drive is taken to be applied to the environment, but the same principles apply for a drive applied to the qubit. The total Hamiltonian is

$$H_{tot} = -\omega_x(t)I_x - \omega_y(t)I_y - \delta(t)I_z + \omega_0 S_z + JI_zS_z, \tag{5.10}$$

where ω_x and ω_y are the quadrature drive strengths, δ is an offset of the environment Larmor resonance from the carrier frequency of the drive, ω_0 is the S spin Larmor frequency, and J is the Ising coupling strength between the two spins. This Hamiltonian may also be written as

$$H_{tot} = -\omega_e(t) \cdot \vec{I} + \omega_0 S_z + JI_Z S_z, \tag{5.11}$$

where ω_e is the effective field acting on the I spin due to the drive and resonance offset. The observable considered on the S spin is the expectation value of the S_x operator

$$\frac{\langle S_x(t)\rangle}{\langle S_x(0)\rangle} = \mathrm{Tr}\left[S_x U(t) S_x U^\dagger(t)\right], \tag{5.12}$$

with

$$U(t) = \mathcal{T} e^{-i\int_0^t \mathrm{d}\tau\, H_{tot}(\tau)}. \tag{5.13}$$

In the absence of decoupling, the qubit-environment interaction would lead to a S spin spectrum – defined as the Fourier transform of $\langle S_x(t)\rangle$ – consisting of two delta functions separated by J. Based on an average Hamiltonian argument, Waugh states that the signature of decoupling is a scaling of the effective J-coupling strength

$$J_{eff} = \lambda J, \tag{5.14}$$

with complete decoupling for $\lambda = 0$. To determine the criteria to obtain the complete decoupling condition, Waugh provides a general calculation of $\langle S_x(t) \rangle$ in terms of a piecewise constant control field. Because $[H_{tot}, S_z] = 0$, the dynamics on spin S admits a direct sum representation under two Hamiltonians, H_+ and H_-, corresponding to the effective qubit Hamiltonian when the I spin is in the state $m_s = +1/2$ and $m_s = -1/2$, respectively. The Hamiltonians are

$$H_+ = -\omega_e(t) \cdot \vec{S} + \frac{J}{2} S_z, \tag{5.15}$$

$$H_+ = -\omega_e(t) \cdot \vec{S} - \frac{J}{2} S_z. \tag{5.16}$$

The resulting unitary operator over the full system Hilbert space may be written in a block diagonal form, as U_+ and U_-, acting only on the S spin space. Since the dynamics are considered only in SU(2), $U_\pm$ may be written as a rotation of angle $\phi_\pm$ about an axis $\vec{n}_\pm$, which leads to an FID that may be written as

$$\frac{\langle S_x(t) \rangle}{\langle S_x(0) \rangle} = \frac{1}{2}(1 + \vec{n}_+ \cdot \vec{n}_-) \cos\left(\frac{\phi_+ - \phi_-}{2}\right) + \frac{1}{2}(1 - \vec{n}_+ \cdot \vec{n}_-) \cos\left(\frac{\phi_+ + \phi_-}{2}\right). \tag{5.17}$$

Given a strong drive, we may say that $\vec{n}_+ \approx \vec{n}_- = \vec{n}_d$, such that the rotation axis is completely determined by the drive and the second term becomes zero. The rotation angles are determined by the resonance offset, δ, and coupling strength, J, as $\phi_\pm = \phi(\delta \pm J/2)$. If we arrange for ϕ_+ and ϕ_- to be equal, the first term becomes unity and the two spins experience evolution only under their respective drift Hamiltonians. In terms of the effective coupling as a function of resonance offset, we obtain

$$J_{eff}(\delta) = \lambda J = \frac{\phi(\delta + J/2) - \phi(\delta - J/2)}{t_r}, \tag{5.18}$$

where t_r is a time over which the drive is periodic. In the limit of small J we obtain

$$\lambda = \frac{1}{t_r} \frac{\partial \phi}{\partial \delta}. \tag{5.19}$$

Waugh's criteria for decoupling, then, is simply stated as requiring the magnitude of the effective rotation on the spin of interest to be constant over the considered range of offset parameters, δ. Note that this argument does not imply any specific decoupling sequence, but allows the evaluation of all sequences based on minimizing λ. Waugh notes that the MLEV sequence [125] is a special case where pulses that perform an inversion of z magnetization over a broad range of δ are interspersed with delay periods to obtain $\phi \to 0$ for all δ over which the inversion pulse functions properly, trivially satisfying $\lambda = 0$.

5.2.2 Decoupling a Static Environment

The essence of Waugh's decoupling argument may be captured in the superoperator formalism (Chapter 2) to extend it to a general model of multiple qubits and an arbitrary, but known, qubit-environment coupling. Instead of computing an FID, we will be interested in determining the requirements on the drive to make the quantum map unitary and composable. We first consider a static environment, with total system Hamiltonian

$$H_{tot}(t, \vec{\omega}_q, \vec{\omega}_n) = H_Q(\vec{\omega}_q) + \omega_d(t) H_d + H_{QE}(\vec{\omega}_n), \tag{5.20}$$

where H_Q is the qubit drift Hamiltonian with $\vec{\omega}_q$ parameterizing any uncertainties, ω_d is the strength of a time-dependent drive applied to only the qubits, and H_{QE} is the qubit-environment coupling, parameterized by $\vec{\omega}_n$. Dissipation arises from averaging over multiple instances of $\vec{\omega}_n$ and $\vec{\omega}_q$. For each instance we may write a unitary propagator

$$U(t, \vec{\omega}_q, \vec{\omega}_n) = \mathcal{T} e^{-i \int_0^t \mathrm{d}\tau \, H_{tot}(\tau, \vec{\omega}_q, \vec{\omega}_n)}. \tag{5.21}$$

The quantum map, represented as a superoperator, may then be determined as an incoherent sum over instances of $\vec{\omega}_n$ and $\vec{\omega}_q$:

$$\mathcal{S}(t) = \int\int \mathrm{d}\vec{\omega}_n \, \mathrm{d}\vec{\omega}_q P(\vec{\omega}_n, \vec{\omega}_q) \overline{U}(t, \vec{\omega}_q, \vec{\omega}_n) \otimes U(t, \vec{\omega}_q, \vec{\omega}_n), \tag{5.22}$$

where $P(\vec{\omega}_n, \vec{\omega}_q)$ is a normalized classical probability distribution from which the instances are drawn. If $U(t, \vec{\omega}_q, \vec{\omega}_n) = U(t)$ for all instances of the noise then the superoperator admits a simple unitary form

$$\mathcal{S}(t) = \overline{U}(t) \otimes U(t). \tag{5.23}$$

One method of ensuring that the unitary trajectories are independent of $\vec{\omega}_q$ and $\vec{\omega}_n$ is to force the drive strength at all times to be significantly larger than the modulus of H_Q and H_{QE}. To see this, we discretize $\omega_d(t)$ to be a piecewise constant set of controls, (ω_d^k), and examine a Magnus expansion of $U_k(t, \vec{\omega}_q, \vec{\omega}_n)$ to determine the average Hamiltonian, $\overline{H}_{tot,k}$ that generates the unitary operation over the period. The zeroth order term over a pulse period length of t_k is:

$$\overline{H}^{(0)}_{tot,k} = \frac{\omega_d^k}{t_k} \int_0^{t_k} \mathrm{d}\tau \, H_d + \frac{1}{\omega_d^k} H_Q(\vec{\omega}_q) + \frac{1}{\omega_d^k} H_{QE}(\vec{\omega}_n). \tag{5.24}$$

If we now let $1/\omega_d^k \to 0$, then the effective Hamiltonian becomes

$$\overline{H}^{(0)}_{tot,k} \approx \omega_d^k H_d. \tag{5.25}$$

Thus, during periods of strong modulation, the contribution of H_Q and H_{QE} to the qubit dynamics is suppressed, yielding a unitary, composable map, as desired.

Assuming that the Lie algebra generated by the drive does not span the full qubit Hilbert space, we must allow evolution under the qubit drift Hamiltonian to achieve universal control. Having demonstrated that periods of weak modulation don't lead to the desired map, we now make an exception for periods of free evolution, during which $\omega_d = 0$. The effective Hamiltonian during these periods is given by

$$H_{tot}(\vec{\omega}_q, \vec{\omega}_n) = H_Q(\vec{\omega}_q) + H_{QE}(\vec{\omega}_n). \tag{5.26}$$

To ensure that the map over the entire gate is composable, we must both reoptimize the full gate to be robust to variations of $\vec{\omega}_q$ (as demonstrated in Chapter 6) and

enforce that $\overline{H}_{QE}(\vec{\omega}_n) = 0$ for all $\vec{\omega}_n$ over an averaging time t_a. The averaging condition on H_{QE} is equivalent to the group averaging discussed by Viola and Lloyd for *dynamical decoupling* [214]. There are many sequences that have been proposed to satisfy the averaging condition for various models of the environment [206, 220, 208]. These sequences often assume delta function pulses – i.e. *bang-bang control* – but have also been analyzed under restrictions of finite pulse length and bounded controls [212, 107]. We relax these conditions to state that the pulses used in a decoupling sequence must only be strongly modulating, where we have not introduced restrictions on the length of any pulse and free evolution periods. These restrictions arise when a stochastic environment is considered.

5.2.3 Generalization to a Stochastic Environment

For a stochastic environment, we use the model introduced in Section 2.4 of additive stochastic noise on the qubit Hamiltonian:

$$H = \omega_d(t) H_d + H_n(t), \tag{5.27}$$

If we assume that the stochastic noise generator, $H_n(t)$, commutes with itself at all times and is derived from a stationary, zero-mean, Gaussian process, then the superoperator is completely determined by the second cumulant

$$K_2(t) = \frac{1}{t^2} \int_0^t \mathrm{d}t_1 \int_0^{t_1} \mathrm{d}t_2 \, \langle \mathcal{L}(t_1)\mathcal{L}(t_2) \rangle \,, \tag{5.28}$$

with $\mathcal{L} = \overline{H} \otimes I - I \otimes H$. When the noise operator does not commute with itself at all times, the second cumulant still bounds the error. To derive an analytic result, we analyze a single qubit under a single cycle of the common CPMG decoupling sequence, consisting of two finite length pulses of constant drive strength ω_d separated by a delay period of length t_d over which $\omega_d = 0$. We further assume the pulses to be about the

x-axis, with noise along the z-axis

$$H = \omega_d \sigma_x + \alpha(t)\sigma_z. \tag{5.29}$$

If the correlation time of $G(t_1 - t_2) = \langle \mathcal{L}(t_1)\mathcal{L}(t_2) \rangle = \mathcal{L}^2 \langle \alpha(t_1)\alpha(t_2) \rangle$ is long compared to the cycle length, the correlation function, $G(t_1 - t_2)$, can be taken as constant, G_c. In this case the second cumulant reduces to

$$K_2 \approx \frac{8}{t^2} \frac{|G_c|}{\omega_d^2} \mathcal{L}^2, \tag{5.30}$$

which goes to zero as $|G_c| / \omega_d^2 \to 0$. For stochastic processes, then, we have the additional requirement that the averaging time is short compared with the correlation time of the noise. This condition was studied in detail by Cappellaro, *et al.* [31].

5.3 Discussion

If the full form of the qubit-environment interaction is known and tractable, we may directly optimize robust gates. In practice, it is not feasible to include the full environment in gate optimizations, so we must design gates that are insensitive to the environment. One method for achieving this is to compose gates of pulsing periods of strong modulation interspersed with periods of free evolution. Requiring that any portions of a quantum gate when the drive has non-zero strength are strongly modulating ensures that the superoperator map for those periods does not include the effects of the qubits drift Hamiltonian or the qubit-environment coupling Hamiltonian, leading to a unitary, composable map.

Permitting periods of free evolution, where the drive strength is set to zero, accomplishes two things: Evolution under the drift Hamiltonian during these periods allows for universal control of the qubits, and any evolution during these periods due to the environment is determined exactly by the qubit-environment coupling Hamiltonian. By arranging that the drive and qubit-environment coupling Hamiltonians are non-commutative, any sequence that averages the qubit-environment to zero over

an averaging time shorter than the correlation time of the noise will suppress evolution due to the environment, resulting in an overall map for the gate that is unitary and composable. For stochastic processes, requiring the averaging time of the noise generator to be short compared with the correlation time of the noise fluctuations ensures that the noise may be effectively refocused.

Strongly modulating pulses were first used in quantum information to design pulses for NMR QIP [61]. These pulses were specifically designed to contain a small number of relatively short periods of high drive amplitude and were noted to be robust to small uncertainties in the qubit drift Hamiltonian [61, 84]. However, when attempting to directly optimize a gate requiring multi-qubit couplings – like a CNOT gate – a single strongly-modulating pulse often cannot be used, as it is designed to suppress the effect of the qubit drift Hamiltonian that often contains the generators for multi-qubit operations. Using long pulses with weak modulation periods, optimal control pulses can be designed to directly implement more complex gates, but anecdotal evidence has shown that these pulses often do not experimentally implement as expected. This discrepancy can be traced to the periods of weak modulation which, while allowing more complex operations to be performed, do not sufficiently modulate the qubit-environment coupling to decouple the qubits from the environment. Thus, unless a complete description of the environment is included in the optimization – an impractical expectation – the experimental performance of weakly modulating pulses ends up being sensitive to small variations in the environment.

Chapter 6

Refocusing Noise: A Robust CPMG Sequence

It was noticed early-on in the development of control techniques for NMR that non-Markovian noise could be refocused by application of a π-angle refocusing pulse to reverse dephasing of magnetization to form a spin echo [78]. This sequence was extended by Carr and Purcell to a series of equally spaced π-angle pulses to form a string of echoes [34]. It was quickly noticed that implementation errors of the π-angle refocusing pulses caused pulse-error-induced dephasing of the initial quantum state. Meiboom and Gill modified the CP sequence to ensure the initial quantum state to be stored was maximally aligned with the phase of the refocusing pulses [149]. The resulting Carr-Purcell-Meiboom-Gill (CPMG) sequence allows the robust storage of a single orthogonal component of a quantum state.

The CPMG sequence is primarily used in magnetic resonance for situations where significant field inhomogeneities are present. The versatility of the sequence lies in its inherent robustness to pulse nutation angle errors and insensitivity to variations in the static, B_0, and the applied drive, B_1, fields. In the context of magnetic resonance, the CPMG sequence is most useful to monitor dynamic processes, such as relaxation and diffusion. For complex systems with multi-exponential decays, it is necessary to acquire large numbers of echoes with short echo spacings to cover the entire range of relaxation times. Averaging over the multiple echoes generated by the sequence

further enhances the signal-to-noise ratio (SNR) of these measurements. In one-sided and stray field magnetic resonance applications, where the inhomogeneity in B_0 is typically much larger than the available drive amplitude, the CPMG sequence is particularly important. These applications include well-logging [71, 92], the NMR-MOUSE [6], and ex-situ and single-sided NMR [150, 159].

The CPMG sequence has also proven to be an excellent means of dynamically suppressing decoherence in quantum information processing [214, 18, 106]. The extent to which the CPMG sequence suppresses a stochastic noise process depends on the memory of the process [31]. For processes with a correlation time, τ_c, approximately equal to the pulse spacing, τ, the CPMG sequence is ineffective. When τ_c is significantly shorter than τ the noise tends to self-decouple without need for applying the sequence. However, in the limit $\tau_c >> \tau$ the noise appears static to the refocusing sequence and may be effectively removed. Field inhomogeneities are a primary source of high-memory noise and we focus in this chapter on how optimal control theory (OCT) may be applied to the CPMG sequence to enhance its robustness to incoherent noise.

Although the CPMG sequence is inherently tolerant of field inhomogeneities and pulse nutation angle errors, the robustness of the sequence is ultimately limited by the quality of the refocusing pulses. In almost all circumstances, it is important to develop refocusing pulses for the CPMG sequence that simultaneously have a large bandwidth with respect to static field inhomogeneity, account for drive field inhomogeneity, and act as a universal rotation. Finding a global solution to maximizing bandwidth for a given pulse time and subject to constraints of pulse power has proven to be difficult [64], and perhaps impossible due to the complexity and size of the problem. However, by taking advantage of extensive theoretical and numerical results in quantum control, we may gain insight into the problem.

OCT provides a systematic means of finding consistent, effective solutions to the problem of designing broadband refocusing pulses suitable for use in the CPMG sequence. We focus, in particular, on finding refocusing pulses that perform an identical unitary operation over as large a range of resonance offsets and drive amplitudes as

possible, while adhering to constraints of pulse length and maximum instantaneous RF power. We also introduce a new method to compactly analyze the dynamics and accumulation of pulse errors in the CPMG sequence.

6.1 CPMG Criteria

The CPMG sequence consists of periodic applications of a cycle, $[\tau$ - $\pi)_y$ - 2τ - $\pi)_y$ - $\tau]$, which repeatedly refocuses transverse spin magnetization, leading to a train of echoes. The accumulation of pulse errors during the sequence causes only a single orthogonal component of the input state to be preserved - the component along the axis of the refocusing pulses. Meiboom and Gill's modification to the original Carr-Purcell sequence was to recognize this symmetry of the pulse errors, and shift the phase of the excitation pulse applied before the sequence such that the initial spin magnetization aligns with the axis of refocusing. There are, then, two common measures for the success of a CPMG sequence: (1) a single orthogonal component of the input state does not decay in the absence of relaxation, regardless of the time between refocusing pulses (echo spacing) and (2) that the echo visibility be maximal. These measures dictate the design requirements for the refocusing pulses: (i) the direction of the effective rotation axis must be oriented exactly in the xy-plane, (ii) the effective rotation axis and the initial spin magnetization must be aligned, and (iii) the effective nutation angle must be π radians.

The influence of not keeping the effective field direction in the transverse plane is seen by considering the efficiency of averaging static field inhomogeneities by a single hard π-pulse that is tilted an angle ζ from the xy-plane. The zeroth order contribution to the average Hamiltonian of a magnetic field inhomogeneity, $H_{\text{int}} = \Delta\omega\sigma_z$, for the sequence $\tau - \pi)_y - \tau$ is

$$\bar{H}_{\text{eff}}^{\text{CP}} = \Delta\omega\sigma_z(1 - \cos 2\zeta) + \Delta\omega\sigma_y \sin 2\zeta. \tag{6.1}$$

Ideally, $\zeta = 0$ and the Hamiltonian vanishes. Notice that when the RF field is

tilted from the transverse plane the refocusing under this sequence is incomplete and similar to that engineered in to the Chemical Shift Concertina sequence [103], which was designed to scale chemical shifts. In calculating (1) we have kept the nutation angle fixed to π as we wish to explicitly illustrate the decrease in averaging as the effective field is rotated out of the xy-plane. The residual contribution to $\bar{H}_{\text{eff}}^{\text{CP}}$ arises from incomplete modulation of the spin dynamics. This reduction in the modulation depth of the averaging is also detrimental to effective decoupling as described by Waugh [217].

Next, consider the sensitivity of the CP cycle to a mis-setting of the pulse nutation angle. We can observe this dependence by calculating the propagator corresponding to one cycle of the CP(MG) sequence, with pulse nutation error ϵ, applied to a spin whose Larmor precession is off-resonance by an amount $\Delta\omega$:

$$U(\epsilon, \Delta\omega) = e^{-i\frac{1}{2}\Delta\omega\sigma_z\tau} e^{-i\frac{1}{2}(\pi-\epsilon)\sigma_y} e^{-i\Delta\omega\sigma_z\tau} e^{-i\frac{1}{2}(\pi-\epsilon)\sigma_y} e^{-i\frac{1}{2}\Delta\omega\sigma_z\tau}. \tag{6.2}$$

For the sake of simplicity, the pulses are assumed to be on-resonance. The improvement that Meiboom and Gill brought to the Carr-Purcell cycle was to recognize that the refocusing is more robust when the pulse rotation axis and the initial magnetization are aligned. The benefit of the CPMG sequence is seen by examining the retained magnetization under conditions of maximal alignment and minimal alignment - $\rho_{\text{in}} = \sigma_y, \sigma_x$ respectively. The overlap of initial and final magnetization under the action of the cycle is

$$O_{x,y} = \frac{1}{2}\text{Tr}\left\{\sigma_{x,y} U(\epsilon, \Delta\omega)\sigma_{x,y} U^{\dagger}(\epsilon, \Delta\omega)\right\} \tag{6.3}$$

$$O_x = 1 - 2\cos^2(\Delta\omega\tau)\epsilon^2 + \mathcal{O}(\epsilon^4) \tag{6.4}$$

$$O_y = 1 - \frac{1}{8}\sin^2(2\Delta\omega\tau)\epsilon^4 + \mathcal{O}(\epsilon^5) \tag{6.5}$$

Notice that if the rotation axis and the initial magnetization are aligned then the pulse error appears only in the 4^{th} order of ϵ, while for the original CP sequence the pulse error appears already in 2^{nd} order.

The value of the CPMG sequence is that it simplifies the spin dynamics when applied over a distribution of Hamiltonians. For most applications, the relevant distribution is a spatially dependent spread in off-resonance frequencies, $\Delta\omega$, and scaled drive field amplitudes, ω_1, relative to a nominal value ($\omega_1 = 1$). The overall dynamics then correspond to a convex operator sum over a classical probability distribution, $P(\Delta\omega, \omega_1)$:

$$\rho_{\text{out}}^{(n)} = \int P(\Delta\omega, \omega_1) \left[U_{\text{cycle}}(\Delta\omega, \omega_1)\right]^n \rho_{\text{in}} \left[U_{\text{cycle}}^{\dagger}(\Delta\omega, \omega_1)\right]^n \mathrm{d}\Delta\omega \, \mathrm{d}\omega_1, \tag{6.6}$$

where $\rho_{\text{out}}^{(n)}$ is the density operator after the application of n cycles ($2n$ pulses). The averaging must be undertaken after the propagator for each element of the distribution is raised to the n^{th} power. An important result in the design of CPMG sequences is that the projection of the rotation axis of not only the refocusing pulse but also the cycle propagator, U_{cycle}, onto the initial magnetization must be as large as possible [91]. If this is true for each element of the distribution, it will be true when the result is averaged over $P(\Delta\omega, \omega_1)$. Additionally, it will be true for all n, as the rotation axis will remain unchanged when the individual propagators are raised to the n^{th} power - corresponding to repeated applications of the cycle. This requires the cycle propagator for each element of $P(\Delta\omega, \omega_1)$ to be expressable as

$$U_{\text{cycle}}(\Delta\omega, \omega_1) = e^{-i\frac{\theta(\Delta\omega,\omega_1)}{2}\sigma_y}, \tag{6.7}$$

such that all spins undergo a y-axis rotation of any angle over the cycle. This requirement places demands on the effective rotation axis and nutation angle of the refocusing pulses in the CPMG cycle.

The inherent robustness of the CPMG sequence to pulse nutation errors is reflected in the rotation axis of the cycle propagator. As stated previously, when the pulse rotation axis is taken to be aligned with the initial magnetization, the cycle rotation axis error appears to 4^{th} order in small deviations from a π nutation angle. However, when the nutation angle is taken to be exactly π radians, the cycle rotation axis error

appears as the cosine of small deviations from a y-axis rotation, first appearing to 2^{nd} order. It is apparent that a deviation of the refocusing pulse from a perfect y-axis rotation is more detrimental to a successful CPMG sequence than is an identical deviation from a perfect π nutation angle.

There is some flexibility in the precision of the rotation characterisitics of the pulse, if a certain amount of signal loss is tolerable. The signal for a particular value of $\Delta\omega$ and ω_1 after k echoes is given by:

$$M_y = (-1)^k \cos(k\delta)(1 - r_y^2) + r_y^2 \tag{6.8}$$

where δ is the deviation of the half-cycle nutation angle from π radians and r_y is the y-component of the half-cycle rotation axis for the isochromat being considered. In order to retain 99% of the initial magnetization, for example, we require r_y to be 0.995 for each isochromat, implying the pulse rotation axis must be within roughly 6 degrees of the initial magnetization, while the pulse nutation angle only need be within roughly 12 degrees of 180 degrees. However, since it is desirable to maximize the retained signal, it is necessary to require that the refocusing pulses be as close to a π rotation about the y-axis as possible, leading to $\theta(\Delta\omega, \omega_1) \approx 2\pi$ and $U_{\text{cycle}}(\Delta\omega, \omega_1) \approx$ I (identity) for all $\Delta\omega$ and ω_1. For input states orthogonal to σ_y, the deviation from identity is cumulative for repeated cycle applications and leads to pulse-error-induced dephasing of the input state.

6.2 Optimization Methods

A great deal of effort has been devoted in the past to using OCT techniques to optimize excitation and inversion pulses which achieve a single state-to-state transformation with a high degree of accuracy [40, 140, 185, 114]. The CPMG sequence, however, requires pulses that perform a universal rotation, acting as a single unitary operation on all input states. It has been shown previously that state-to-state pulses can be made into universal rotation pulses, yielding refocusing pulses of twice

the duration [133]. For example, given a 90° excitation pulse, a universal rotation pulse may be constructed by first applying a phase-reversed version of the excitation pulse, followed immediately by a time reversed version of the excitation pulse. While this symmetrization procedure leads to good refocusing pulses suitable for application in the CPMG sequence, we focus here on searching for general, non-symmetrized pulses. Expanding the set of potential solutions could possibly lead to pulses with better performance.

The dominant Hamiltonian generating the dynamics for an ensemble of isolated spin-$\frac{1}{2}$ nuclei consists of the Zeeman interaction with the applied static, B_0, field and the resonant interaction with the applied drive, B_1, field:

$$H(t) = \frac{\Delta\omega}{2}\sigma_z + A(t)\frac{\omega_1}{4}e^{-i(\omega_t t+\phi(t))\sigma_z/2}\sigma_x e^{i(\omega_t t+\phi(t))\sigma_z/2}. \tag{6.9}$$

Here the OCT pulse is a time-dependent modulation of the RF amplitude, $A(t)$, and phase, $\phi(t)$, applied at a transmitter frequency ω_t. In our notation, ω_1 is a dimensionless scaling factor of the drive amplitude. Our goal is to find time sequences of the control parameters, $\{A(t), \phi(t)\}$ which, taken over the set of Hamiltonians determined by $P(\Delta\omega, \omega_1)$, correspond to action which is sufficiently 'close' to a desired transformation, as measured by the average gate fidelity (eq. 5.4). Since we are optimizing over a classical probability distribution we take the convex weighted sum of the average gate fidelity for each member of the distribution:

$$\widetilde{\Phi} = \sum_{\Delta\omega,\omega_1} P(\Delta\omega, \omega_1)\, \Phi_{\Delta\omega,\omega_1}(U_{\text{pulse}}, U_{\text{targ}}), \tag{6.10}$$

where

$$\Phi_{\Delta\omega,\omega_1}(U_{\text{pulse}}, U_{\text{targ}}) = \frac{\left|\text{Tr}\left\{U_{\text{pulse}}(\Delta\omega, \omega_1)\, U_{\text{targ}}^{\dagger}\right\}\right|^2}{4}. \tag{6.11}$$

The behavior of (6.11) with respect to $\Delta\omega$ and ω_1 is sufficient to ensure the satisfaction of the CPMG criteria. Consider a general rotation in SU(2),

$$U(\theta, \widehat{r}) = e^{-i\frac{\theta}{2}\widehat{r}\cdot\vec{\sigma}}, \tag{6.12}$$

with nutation angle θ about an axis given by the unit vector $\widehat{r}$. The corresponding fidelity to a π rotation about the y-axis is

$$\Phi(U, e^{-i\frac{\pi}{2}\sigma_y}) = \sin^2\frac{\theta}{2}r_y^2 = \sin^2\frac{\theta}{2}\cos^2\phi, \tag{6.13}$$

where θ is, again, the nutation angle of the pulse and ϕ is the angle between $\widehat{r}$ and $\widehat{y}$. Small deviations from a π rotation about the y-axis cause the fidelity to decrease quickly, ensuring that high-fidelity correponds to the satisfaction of CPMG criteria (i) and (ii). Additionally, as noted in CPMG criteria (iii), the requirement that it is more important to minimize ϕ than it is to minimize θ is reflected in the behavior of the fidelity. It is useful to note that, in our approach, it is easy to substitute a particular functional for a different one. While our chosen performance functional exhibits the general behavior we desire, we cannot rule out the existence of another functional which may be more sensitive to deviations in ϕ while allowing more flexibility in θ. Such a functional could possibly lead to more accurate solutions with an enhanced bandwidth.

6.2.1 Iterative Optimization Strategy

In the absence of constraints, the GRAPE algorithm guarantees that our optimized pulse parameters will deterministically converge to the nearest local maximum of average fidelity. The value of the average fidelity at this local maximum depends on the structure of the control landscape – a geometric representation of the value of the performance functional as a function of the control parameters. By definition, the control landscape for our chosen performance functional is given by the weighted convex sum of the control landscapes for each member of the distribution, $P(\Delta\omega, \omega_1)$. The stucture and dimensionality of the control landscape is determined by our choice of T, Δt, and $P(\Delta\omega, \omega_1)$. Limiting the maximum instantaneous RF power constrains the ability of the algorithm to reach a local optimum from a given random initial guess of the pulse parameters, $\{A_j, \phi_j\}_{\text{init}}$

In idealized situations, two key results of quantum control theory provide some

insight into the structure of the control landscape, and thus, the level of control we can expect to achieve. In general, though, very little may be concretely said about the structure of the control landscape in quantum optimizations, which makes it difficult to find the best possible (global) solution. It has been shown that in the absence of decoherence every local optima is exact [166, 35], and even in the presence of a static, classical distribution of Hamiltonians there exist solutions which provide exact implementations of the desired unitary operation for every member of the ensemble (see online material for [166]). However, these results only apply to situations where there are no constraints on pulse length and amplitude and the pulse shape is taken to be changing continuously as a function of time. Imposing these constraints, as we do in this work, implies that our solutions will not reach the desired optimum over the distribution, and that no optimum will correspond to an exact implementation of the desired unitary operator. When optimizing a particular initial guess to the nearest optimum point, then, we are sampling from the set of non-degenerate local optima without any guarantee of the performance being close to the global maximum.

We tried two systematic methods to investigate the maximum achievable pulse performance for our techniques and constraints, each of which produced similar results but differed in efficiency and information gained about the structure of the control landscape. The first method involved choosing a particular width of the distribution and optimizing hundreds of random initial guesses to obtain a histogram of achievable fidelities. The best of these was then taken as the maximum performance we could achieve for the distribution in question. The width of the distribution was then increased, and the process repeated, until the highest achievable fidelity was no longer satisfactory. Our results for a single width of the distribution confirmed the behavior seen in [114]. A wide range of optimized fidelities were obtained, with the majority clustered around higher values. The results of these optimizations tell us that the static collective landscape for our problem contains many varieties of local optima that may trap gradient algorithms, but the performance of most of these optima is similar and normally correspond to good control.

To gain further insight into the way the collective landscape changes as new ele-

ments are added to the distribution, we also implemented a new method, where a single initial guess is systematically optimized over distributions of increasing width. We first attempted to maximize the bandwidth of the pulse with respect to static field inhomogeneity, while neglecting drive field inhomogeneity (i.e. setting $\omega_1 = 1$). The target bandwidth of the pulse was defined to be $2\Delta\omega_{\max}$, where the uniform distribution was defined as $\overline{P}(\Delta\omega) = 1/M$ for M values of $\Delta\omega = (-\Delta\omega_{\max}, ..., -\delta\omega, 0, \delta\omega, ..., \Delta\omega_{\max})$. The value of $\delta\omega$ is determined by the length of the pulse in order to ensure that if high fidelity is achieved at each point in the distribution, the fidelity taken continuously in between will remain high. We found that a value of $\frac{1}{4T}$, where T is the length of the pulse, is sufficient.

The iterative optimization procedure started with an on-resonance optimization, $\overline{P}_1(\Delta\omega = 0) = 1$, where the results of quantum control theory dictate that unit fidelity is always achievable regardless of initial guess. The resulting optimized pulse was then used as the initial guess for an optimization over 3 isochromats, $\overline{P}_2(\Delta\omega = -\delta\omega,\ 0,\ \delta\omega) = 1/3$, and allowed to run until a local maximum of the new collective landscape was found. A small amount of randomization was added such that the the distance between isochromats was not exactly equal. After a pulse was optimized over 3 isochromats, that pulse was used as an initial guess for 5 isochromats, $\Delta\omega = (-2\delta\omega,\ -\delta\omega,\ 0,\ \delta\omega,\ 2\delta\omega)$, and so on.

The iterative process was terminated when the average fidelity achieved over the distribution dropped below roughly 0.9. We found that by using this process, regardless of our initial guess, a series of convergent pulses with an associated fidelity vs. static inhomogeneity bandwidth curve was generated (Fig. 6-1) and a satisfactory result was obtained in only the order of tens of optimizations. The characteristics of this curve varied depending on the initial guess, but always yielded usable solutions. In order to account for drive field inhomogeneity a pulse from the related set generated by the iterative optimization was chosen to be reoptimized. Without changing the bandwidth of the pulse with respect to static field inhomogeneity, a certain amount of drive field inhomogeneity was added. For example, if we chose a pulse that was optimized over 41 values of $\Delta\omega$ and we added in $\pm 10\%$ drive field inhomogeneity, given by

$\omega_1 = 0.9, 0.95, 1, 1.05, 1.1$, the resulting distribution $\overline{P}(\Delta\omega, \omega_1) = 1/204$ would have 41*5 = 204 elements.

The success of this particular approach suggests that the structure of the collective landscape characterizing the average fidelity does not change abruptly as the width of the distribution is increased slowly. A good solution for a given distribution width should therefore remain in the immediate neighborhood of a local optimum with high fidelity for a slightly wider distribution width. However, concrete statements about the structure of the control landscape are the subject of quantum control theory, and are outside the scope of this present work.

6.3 Simulated Optimization Results

We present specific results obtained by optimizing the fidelity of OCT refocusing pulses constrained to be 1 ms duration and with a maximum instantaneous drive amplitude of $A_{\max}/2\pi = 5$ kHz. Our pulses were defined piecewise constant over 100 intervals of 10 μs duration and the 200 degrees of freedom in the problem - 100 periods of varying pulse amplitude and phase - were optimized iteratively over a uniform distribution using the GRAPE algorithm (Section 5.1.2) at each iteration. A 6 μs delay before and after the pulse was incorporated into the optimization to account for hardware switching times in back-to-back applications of our pulses. These delays are not directly part of the pulse waveform, but must be included in simulations and experiments in order for the pulse to function properly.

Using the iterative optimization procedure we generated a series of related pulses, terminating the series when the average fidelity dropped below roughly 0.9 for the target bandwidth being optimized. Figure 6-1 displays two representative curves of the average fidelity of the optimized pulses as a function of target bandwidth ($|\Delta\omega| \leq \Delta\omega_{\text{targ}}$). Not surprisingly, for small target bandwidths it is possible to find pulses with an average fidelity very nearly unity; unit fidelity was achieved only for the on-resonance optimization. As the target bandwidth is increased, the average fidelity begins to drop, with the detailed characteristics of the curve dependent upon

the initial guess. We found that the target bandwidth at which the average fidelity drops below 0.99 was nearly the same for all initial guesses we tried. We took this point to represent the maximum bandwidth achievable before pulse performance is significantly affected. Based on this performance criterium, the best refocusing pulse we could find for uniform drive is marked in fig. 6-1 and has an average fidelity $\widetilde{\Phi} = 0.989$ over a total bandwidth of 4 $A_{\max}$. Figure 6-2 shows the calculated response of a CPMG sequence using this refocusing pulse, in the absence of relaxation and with uniform drive. The response is almost entirely maximal across the entire optimization range with refocusing of over 96% of the magnetization at any offset. This performance is retained at higher echo numbers. This confirms that optimizing the average fidelity maximizes the echo visibility and allows the generation of a large number of echoes.

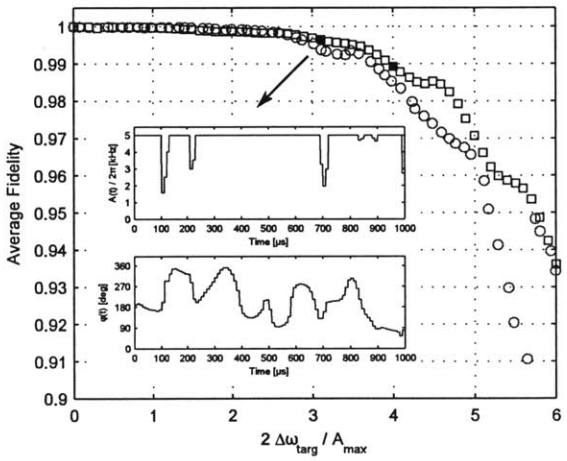

Figure 6-1: Two representative examples of the iterative optimization procedure utilized in this study. The results shown by the red circles and blue squares correspond to two iterative series of pulses derived from two different random initial guesses, respectively. The pulses are iteratively optimized over an increasing target bandwidth of resonance offsets. We find that, regardless of the initial guess, the resulting curves of average fidelity versus target bandwidth are similar, indicating that the pulses for the different realizations have similar maximum bandwidth. The filled in squares represent the pulses mentioned in the text, with the inset showing the temporal profile of the pulse chosen for extended analysis. High-resolution pulse profile and parameter list is available in supplementary material.

When drive field inhomogeneity is included in the optimizations, a trade-off be-

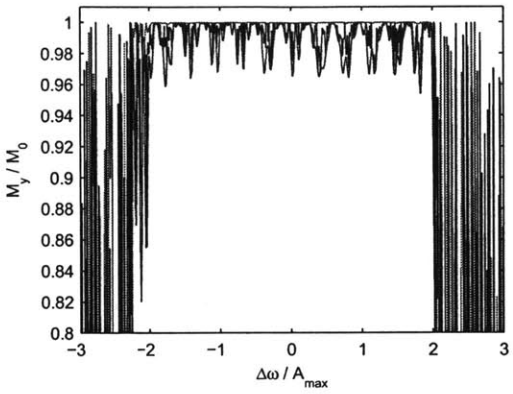

Figure 6-2: Calculated magnetization as a function of resonance offset for the first (blue), second (red), and 500th (black) echoes of a CPMG sequence using the 1 ms OCT refocusing pulse optimized over $|\Delta\omega| \leq 2\ A_{\max}$. The simulation assumes a perfect excitation pulse, no relaxation, and uniform drive. The time between refocusing pulse applications is $2\tau = 2$ ms. The magnetization is very nearly retained over the entire optimization range, and shows no additional degradation for higher echo numbers.

tween achievable resonance offset bandwidth and drive inhomogeneity compensation becomes apparent. For modest drive strength variations of $\pm 10\%$ ($\omega_1 = 0.9 - 1.1$), the average pulse fidelity of the pulse optimized over a static offset bandwidth of 4 $A_{\max}$ drops to 0.972, while a pulse optimized over a static offset bandwidth of 3.2 $A_{\max}$ has average fidelity of 0.982. For uniform drive the latter pulse has average fidelity of 0.996 over the respective bandwidth. We chose this pulse for further analysis. It's temporal profile is shown in the inset of fig. 6-1. The drive tends to remain on for nearly the entire pulsing time while the phase is non-trivially varied in a non-symmetric way.

To verify that high average fidelity leads to the desired pulse performance, we must consider the fidelity and CPMG criteria of our OCT refocusing pulse as a function of resonance offset. Given the relation between fidelity and pulse rotation errors (eq. 6.13), an average fidelity close to unity implies that for every value within the considered $B_0 - B_1$ distribution, the net action of the optimized pulse is very close to a π rotation around the y-axis. Figure 6-3 demonstrates that this is indeed the case. For comparison, we include the corresponding quantities for a standard hard π pulse of the same maximum drive amplitude (duration 100 μs). Note that, in general, the

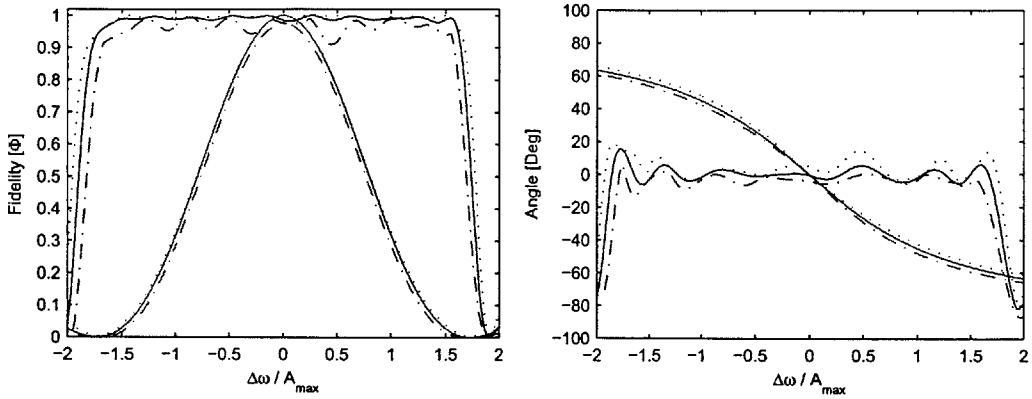

(a) Fidelity

(b) Angle From XY-Plane

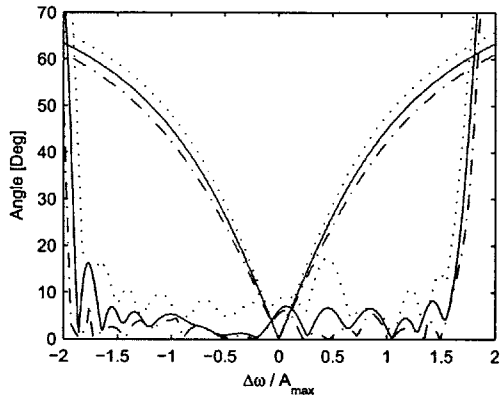

(c) Angle From Y-axis

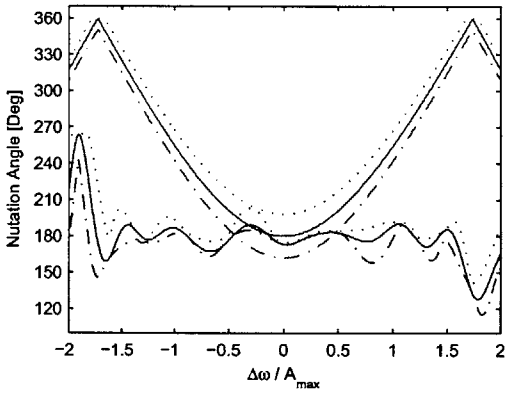

(d) Nutation Angle

Figure 6-3: Fidelity and CPMG criteria as a function of resonance offset for the 1 ms OCT refocusing pulse (Blue) optimized over $|\Delta\omega| \leq 1.6\ A_{\max}$ and $\omega_1 = 0.9 - 1.1$, as compared to a 100 μs hard pulse (Red). The solid lines indicate the response for uniform drive ($\omega_1 = 1$), while the dotted (dash-dotted) lines indicate the maximum (minimum) angle over the range of $\omega_1 = 0.9 - 1.1$. The rotation axis for the OCT pulse stays within 15° of the initial magnetization over the optimized distribution and the nutation angle remains within 30° of 180°.

deviation of the rotation for our OCT pulse from a y-axis rotation is smaller than the deviation from a π nutation angle, as desired.

6.4 Experimental Verification

In order to verify that our OCT pulses perform as expected in experiment, we performed CPMG measurements on a sample of 90% D_2O / 10% H_2O. Roughly 3 mM copper-sulfate ($CuSO_4$) was added to the sample in order to obtain a relaxation time of $T_2 \approx 270$ ms at 300 MHz proton resonance. RF inhomogeneity was measured to extend out to $\pm 20\%$, with the majority of the field strengths concentrated in the $\pm 10\%$ range. We performed CPMG measurements using the OCT refocusing pulse shown in the inset of fig. 6-1, having a total duration of 1 ms and a maximum RF amplitude $A_{\max}/2\pi = 5$ kHz, with a time between refocusing pulses of $2\tau = 20$ ms. The 90° excitation pulse was an on-resonance rectangular hard pulse of amplitude 31.25 kHz to ensure the sequence performance was limited only by the refocusing pulses. To test the performance under off-resonance conditions, we systematically varied the offset of the proton transmitter frequency from the Larmor frequency in 100 Hz increments in the range from -10 kHz to 10 kHz. Figure 6-4a shows the amplitudes of the first 13 echoes of a CPMG sequence with OCT refocusing pulses as a function of offset frequency. As a comparison, we show in fig. 6-4b the first 10 echoes of a CPMG sequence using standard, hard refocusing pulses of 5 kHz amplitude. The measurements confirm that, for the OCT refocusing pulses, pulse errors do not contribute significantly to the observed decoherence and the echo visibility is maximal over the entire optimized range of $|\Delta\omega| \leq 1.6\ A_{\max}$.

To further quantify the echo decay, we compared the amplitudes of the CPMG echoes as a function of time for different values of the time between OCT refocusing pulses, 2τ, and for two particular values of resonance offset (fig. 6-5). The slope for each of these echo spacings is nearly identical, in agreement with our expectation. In addition, there is no evidence of additional pulse-induced relaxation decay when shorter echo spacings are used. In fact, our results suggest that when more pulses are applied in a given time period, $T_{2,\text{eff}}$ becomes slightly longer. This is most likely due to T_1 being slightly longer than T_2. The complex trajectories taken on the Bloch sphere, as shown in fig. 6-6, cause the magnetization to spend some amount of time away

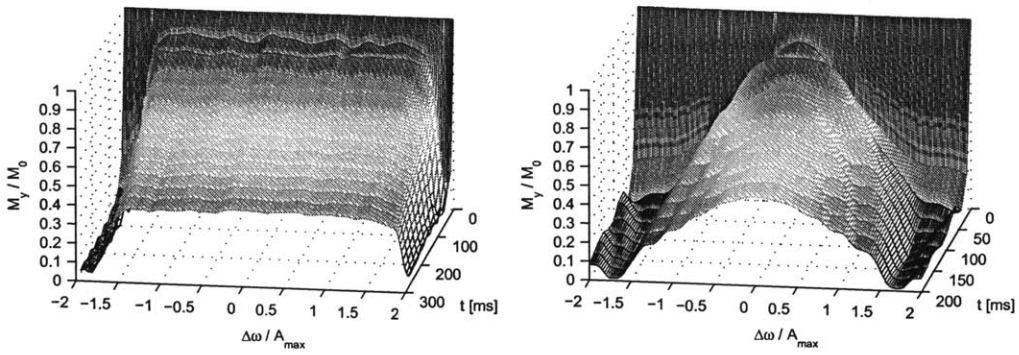

(a) OCT Pulses (b) Hard Pulses

Figure 6-4: Experimental results of echo amplitudes generated by CPMG sequences with OCT refocusing pulses (top) and standard hard pulses (bottom) acquired at 300 MHz on a sample of $CuSO_4$ doped 90% D_2O / 10% H_2O with $T_2 \approx 270$ ms. The results were acquired sequentially by changing the resonance offsets systematically over the range of $|\Delta\omega| \leq 2$ $A_{\max}$. The time between refocusing pulses is $2\tau = 20$ ms. The CPMG sequence with OCT pulses generates a uniform response over resonance offsets in the range of ± 1.6 $A_{\max}$. The response of the excitation pulse is shown to be flat over the relevant range of resonance offsets.

from the transverse plane. This implies that as more pulses are applied in a given time period, the effects of T_1 become increasingly important. While the exact proportion of time spent away from the transverse plane varies depending on resonance offset, in general the magnetization undergoes T_1 relaxation for roughly one third of the pulse duration. Using this approximation and a measured value of T_2 of roughly 270 ms (using a hard pulse CPMG sequence on-resonance), the measured $T_{2,\text{eff}}$ of 282 ms for $2\tau = 2$ ms implies a T_1 of roughly 370 ms. These values predict an apparent T_2 for $2\tau = 10$ ms of 275 ms, consistent with our measurement. Similarly, the measured and expected values of T_2 for $2\tau = 30$ ms and 60 ms are close to 272 ms.

6.5 Comparison to Previous Pulses

Figure 6-7 compares the performance of our OCT pulse with previously published refocusing pulses by examining the fidelity as a function of resonance offset, averaged

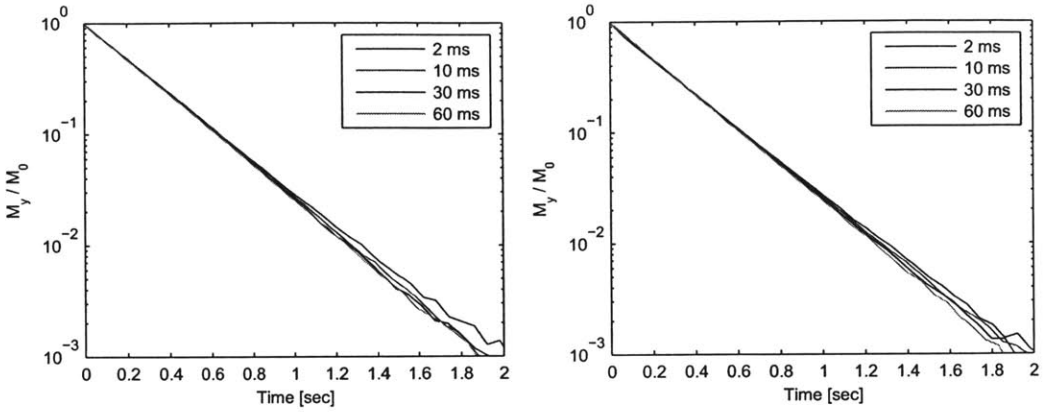

(a) $\Delta\omega/2\pi = 100$ Hz (b) $\Delta\omega/2\pi = 7000$ Hz

Figure 6-5: Comparison of measured echo amplitudes with different values of 2τ (time between refocusing pulses), as indicated in the legend, for a CPMG sequence with OCT refocusing pulses. The results show that a decrease in echo spacing does not lead to an increase in the relaxation rate, indicating that no additional relaxation is induced by the pulses. In fact, as the echo spacing is decreased and more pulses are applied, the measured relaxation time becomes longer. As discussed in the text, this is caused by T_1 effects during the application of the refocusing pulses. Additionally, the measured echo amplitudes show a small transient effect of roughly 1% amplitude, in agreement with expectation, but not apparent in the current display.

over $\pm 10\%$ RFI. The Chirp pulse is a composite adiabatic pulse [93] composed of a base element Chirp adiabatic inversion pulse [22, 21, 65] scaled to $A_{\max}/2\pi = 5$ kHz. The original pulse was 2 ms long, with a 60 kHz sweep width, 20% smoothing, and on-resonance adiabaticity of $Q_0 = 5$. Our scaled version changes the sweep width to 30 kHz and the pulse length to 4 ms, without changing Q_0. We found that, with the constraint of maximum RF amplitude, 4 ms was the minimum time required for the pulse to fulfill the adiabatic condition and function properly. Additionally, a previously derived 90° OCT excitation pulse was downloaded from the website mentioned in [114] and turned into a 1.02 ms refocusing pulse consisting of 1020 intervals of 1 μs duration by the method detailed in [133]. The excitation pulse was originally optimized over $|\Delta\omega| \leq 1.5\ A_{\max}$ and $\omega_1 = 0.8 - 1.2$. The performance quality of the original excitation pulse with respect to $\Delta\omega$ and ω_1 is retained by the symmetrized refocusing pulse.

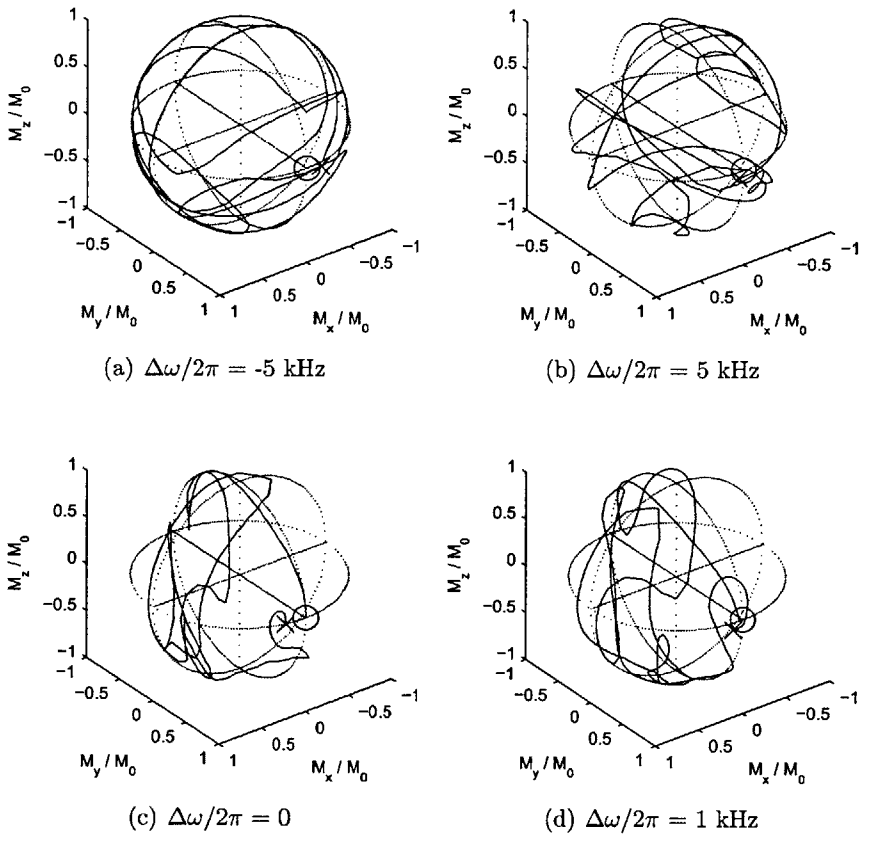

(a) $\Delta\omega/2\pi$ = -5 kHz (b) $\Delta\omega/2\pi$ = 5 kHz

(c) $\Delta\omega/2\pi = 0$ (d) $\Delta\omega/2\pi$ = 1 kHz

Figure 6-6: Bloch sphere trajectories during the OCT refocusing pulse for several values of resonance offset as applied to a σ_y initial state. The trajectories for different isochromats vary significantly but result in nearly identical effective rotations. Roughly two-thirds of the magnetization is in the transverse plane during pulsing. The black 'o' denotes the initial state, while the black 'x' denotes the final state.

As shown in the figure, each of the pulses considered performs very nearly as a $\pi)_y$ pulse over a range of resonance offsets of $\pm 1.6\ A_{\max}$. The Chirp pulse performs most closely to the desired behavior over the operating range, but at the expense of being four times longer than the OCT pulses. The performance of the pulse derived by symmetrizing a previously reported OCT excitation pulse is similar to the performance of our OCT pulse found by direct optimization without symmetrization. The fact that similar limits of performance for OCT pulses were obtained by different means and using many different initial guesses suggests that we may be very near the

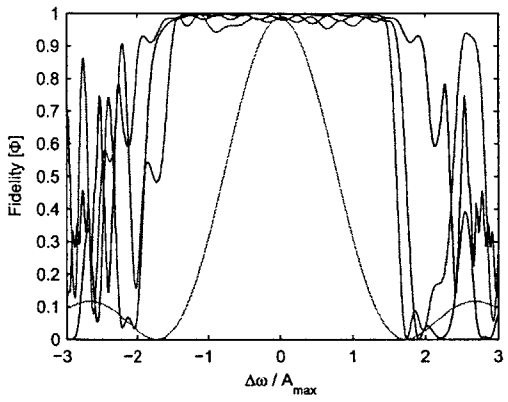

Figure 6-7: Simulated fidelity as a function of resonance offset for our 1 ms OCT pulse optimized over ±10% RFI and $|\Delta\omega| \leq 1.6\ A_{\max}$ (blue), a previously published OCT excitation pulse [114] optimized over ±20% RFI and $|\Delta\omega| \leq 1.5\ A_{\max}$ and modified to be a 1.02 ms refocusing pulse (red), a 4 ms Chirp refocusing pulse (black) [93], and a 100 μs hard pulse (green). All pulses have maximum RF amplitude $A_{\max}/2\pi = 5$ kHz. The fidelities for each offset were averaged over ±10% RFI ($\omega_1 = 0.9 - 1.1$). High-resolution time-domain profiles for each pulse are included in the supplementary material.

global limit on bandwidth for the constraints considered, and that the performance of many solutions are clustered around the global maximum. However, a proper treatment of this claim requires further investigation and is outside the scope of this work.

While it is instructive to consider the performance criteria of a single refocusing pulse, it is difficult to use this information directly to infer the performance of the CP(MG) sequence over many pulses. To do so we must consider not only the errors which occur during a single pulse application, but how they correlate and evolve during the application of many pulses. In the next section, we take advantage of developments in the study of quantum channels to compactly describe the nature and severity of errors that occur during the CP(MG) sequence and quantify the effects those errors have on the performance of the sequence.

6.6 Pulse Error Analysis

To appreciate how the near satisfaction of the CPMG criteria for each isochromat leads to a successful CPMG sequence, we consider the collective action averaged over $P(\Delta\omega, \omega_1)$. As given by eq. 6.6, the overall dynamics correspond to a convex operator sum over the distribution. While the action is unitary for each isochromat, the overall action viewed as an effective map from ρ_{in} to ρ_{out} need no longer be unitary. In this case, representation via a superoperator is needed to provide a compact and complete description of the dynamics.

6.6.1 CPMG Superoperator

The elements of the CPMG superoperator for n cycle applications are determined by the action of the map on a spanning set of basis vectors in Liouville space. In the Pauli basis the superoperator for n cycles of the CPMG sequence is

$$\langle\widetilde{\sigma}_\beta|\,\widetilde{S}_n\,|\widetilde{\sigma}_\alpha\rangle = \frac{1}{2}\mathrm{Tr}\Big\{\sigma_\beta \int P(\Delta\omega,\omega_1)\,[U_{\text{cycle}}(\Delta\omega,\omega_1)]^n\,\sigma_\alpha\,\Big[U^\dagger_{\text{cycle}}(\Delta\omega,\omega_1)\Big]^n\,\mathrm{d}\Delta\omega\,\mathrm{d}\omega_1\Big\}. \tag{6.14}$$

Here $\sigma_{\alpha,\beta} = \{I, \sigma_x, \sigma_y, \sigma_z\}$ are the usual spin-$\frac{1}{2}$ Pauli operators and $|\widetilde{\sigma}_{\alpha,\beta}\rangle$ are the columnized version of the operators obtained by stacking the first column of the respective Pauli matrix on top of its second column [81]. The columnized Pauli operators are basis vectors in Liouville space.

While the unitary dynamics for a single spin-$\frac{1}{2}$ are describable in a 2-dimensional Hilbert space, the superoperator is described in a 4-dimensional Liouville space. Notice that, because the superoperator is averaged over a physical distribution, we must describe a superoperator individually for each n. This is equivalent to the statement made in section 6.1 that the averaging must be undertaken after the propagator for each element of the distribution is raised to the n^{th} power. Since we have approximated the input density matrix of the system as being independent of this distribution, the superoperator is completely positive and has a Kraus representation (see

Section 2.1.2) with Kraus operators

$$A_k = \sqrt{p_k} U_k, \tag{6.15}$$

such that a portion of the sample given by the probability p_k experiences evolution under the action of the unitary propagator U_k. Since we also require that the map be trace-preserving, the Kraus operators must satisfy the condition

$$\sum A_k A_k^\dagger = \mathrm{I}. \tag{6.16}$$

The form of the Kraus operators given in eq. 6.15 is a result of the space of all completely positive, trace-preserving (CPTP) maps for a single spin being convex with unitary extrema. This means that any Kraus operator that is non-unitary may be written as a linear sum of unitary Kraus operators. Thus, any non-unitary Kraus representation of a CPTP map may be transformed into a linear combination of unitary operators.

A map corresponding to unitary evolution will yield only one non-zero eigenvalue and, as a result, be fully described by a single Kraus operator with unit probability. As the CPMG superoperator will not necessarily be unitary, the Kraus representation will generally consist of four operators with varying probabilities. Kraus representation as a Pauli channel yields considerable insight into the multi-pulse dynamics that occur during a CPMG sequence.

6.6.2 Pauli Channel Model

In the context of the CPMG sequence, the quantum channel is the sequence of refocusing pulses and delays taken together with incoherent noise given by magnetic field inhomogeneities. The quantum mechanical entities to be connected are the initial and final density matrices representing the spin state after n applications of the CPMG cycle. A Pauli channel representation, C_p, of the CPMG sequence acting on

an uncorrelated input state, ρ_{in}, for an ensemble of spins-$\frac{1}{2}$ is defined by

$$\rho_{\text{out}} = C_{\text{p}}(\rho_{\text{in}}) = \sum_{i=0}^{3} p_i \sigma_i \rho_{\text{in}} \sigma_i^{\dagger}, \tag{6.17}$$

where $\sigma_i = \{I, \sigma_x, \sigma_y, \sigma_z\}$ and p_i denotes the probability of the system undergoing evolution under the action of the i^{th} operator. For example, spin-spin (T_2) relaxation during a CPMG sequence with ideal pulses may be modeled as a Pauli channel dephasing process about the longitudinal axis, corresponding to σ_z-noise. For this process only two Kraus operators with non-zero probability are needed:

$$\begin{aligned} A_0(t) &= \sqrt{0.5 + 0.5e^{-t/\text{T}_2}}\ \text{I} \\ A_1(t) &= A_2(t) = 0 \\ A_3(t) &= \sqrt{0.5 - 0.5e^{-t/\text{T}_2}}\ \sigma_z \end{aligned} \tag{6.18}$$

A_0 refers to the identity operation, I, occuring with probability $p_0 = 0.5 + 0.5e^{-t/\text{T}_2}$, while A_3 refers to a transverse dephasing operation, σ_z, occuring with probability $p_3 = 0.5 - 0.5e^{-t/\text{T}_2}$. It is clear from this model that, for short times, all input states will experience the identity operation and remain unchanged. However, as time progresses, the probability of the dephasing operation, σ_z, occuring will exponentially grow, leading to the expected decay of the transverse spin states. Note, also, that the σ_z input state, corresponding to longitudinal magnetization, will remain unchanged for all time, as desired.

Similarly, if considered as a pure dephasing channel and assuming imperfect y-axis refocusing pulses, a Pauli channel representation of the CPMG sequence in the absence of relaxation will have two operations with non-zero probability, σ_y and I. The σ_y dephasing operator will cause the σ_x and σ_z input states to decay, while the σ_y input state will remain unchanged. In general, though, CPMG dynamics are not pure dephasing and to properly model the sequence as a Pauli channel requires consideration of all four possible Kraus operators. It is evident, then, that a successful CPMG sequence with y-axis refocusing pulses must have asymptotically small and

bounded probabilities for the σ_x and σ_z operators such that the σ_y input state does not decay.

The results of a Pauli channel fit for a CPMG sequence using our OCT refocusing pulse optimized over $|\Delta\omega| \leq 1.6\ A_{\max}$ and $\omega_1 = 0.9 - 1.1$ is shown in fig. 6-8a. Based on a comparison of the fitted superoperators to the superoperators calculated directly from eq. 6.14, the Pauli channel model captures over 99% of the action of the map. It is evident that the decay and growth of the I and σ_y operations are not entirely exponential, reinforcing the notion that the CPMG sequence cannot be fully represented as a pure dephasing channel. In fact, there are three main elements to the dynamics: An immediate loss of visibility due to the fringes of the distribution that are not compensated by the π-pulse, a fast loss of visibility due to initial oscillations that lead on large n to damping, and dephasing that preserves only a single orthogonal input state.

The complete simulated dynamics of a CPMG sequence and CP sequence using our OCT refocusing pulse is shown in fig. 6-9. Note that the complete CP(MG) dynamics are calculated for every echo while the Pauli channel representation is calculated over the cycle (2 echoes). The decay envelope of the CP sequence ($\rho_{\text{in}} = \sigma_x$) is captured almost entirely by the decay and growth of the probabilities of the Pauli channel identity and σ_y operations, respectively. It is the σ_y and σ_z operations that represent the dephasing part of the dynamics for a CP sequence. As the probability of the σ_y operation occuring is not asymptotically small and bounded, the magnetization retained by the CP sequence is nearly zero for large numbers of echoes. This contrasts with the envelope of the CPMG sequence ($\rho_{\text{in}} = \sigma_y$), where the dephasing operators are σ_x and σ_z. As the probabilities of these operators are asymptotically small and bounded, the magnetization retained by the CPMG sequence is always close to unity.

A method for quantitatively evaluating the cumulative pulse errors that occur during a CPMG sequence can now be formulated. We may assign a model based on a Pauli channel that captures the three elements of the CPMG dynamics just

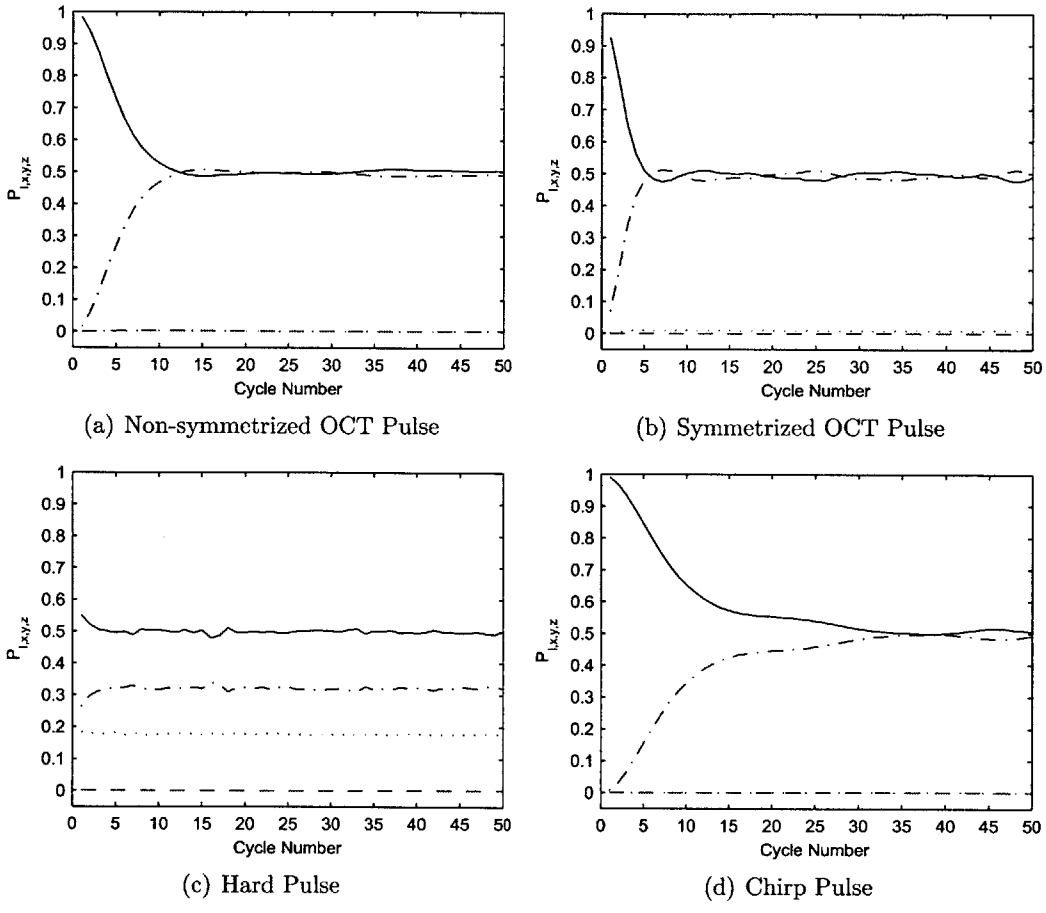

(a) Non-symmetrized OCT Pulse

(b) Symmetrized OCT Pulse

(c) Hard Pulse

(d) Chirp Pulse

Figure 6-8: Pauli channel representations for CPMG dynamics using four different refocusing pulses. Probabilities of the identity (black solid), σ_x (red dashed), σ_y (blue dash-dotted), and σ_z (green dotted) operations are shown as a function of the number of cycle applications. The sequences were simulated over $|\Delta\omega| \leq 1.6\ A_{\max}$ and $\omega_1 = 0.9 - 1.1$ with time between refocusing pulses of $2\tau = 2$ ms. Similar behavior is seen when the value of τ is varied. Representation as a Pauli channel allows us to accurately compare the influence of cumulative errors associated with each pulse. The dephasing rate constant, $T_{2,\text{pulse}}$, was taken as the 1/e point in the decay of the identity probability.

mentioned:

$$\begin{aligned} A_0(n) &= \sqrt{c_I + 0.5e^{-nt_c/T_{2,\text{pulse}}}}\ \mathrm{I} \\ A_1(n) &= \sqrt{c_x}\ \sigma_x \\ A_2(n) &= \sqrt{c_y - 0.5e^{-nt_c/T_{2,\text{pulse}}}}\ \sigma_y \\ A_3(n) &= \sqrt{c_z}\ \sigma_z \end{aligned} \tag{6.19}$$

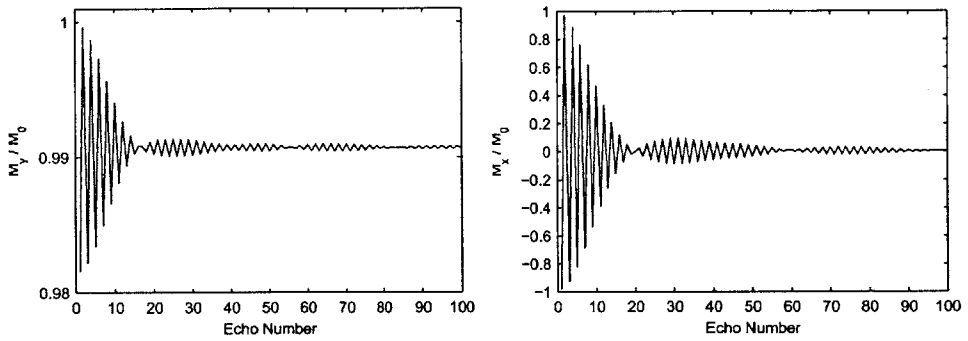

(a) CPMG Sequence (b) CP Sequence

Figure 6-9: Full simulated dynamics for a CPMG sequence and CP sequence using our OCT refocusing pulse optimized and simulated over $|\Delta\omega| \leq 1.6\ A_{\max}$ and a range of drive amplitudes of $\omega_1 = 0.9 - 1.1$. The time between refocusing pulses was set to $2\tau = 2$ ms. The immediate and fast loss of visibility is shown by the initial and asymptotic magnetization being less than unity. The decay of the transients is due to the dephasing portion of the dynamics. Representation of the dynamics as a Pauli channel captures over 99% of the action of the map, describing both the loss of visibility and pulse-induced dephasing.

In this model, $T_{2,\text{pulse}}$ is a time constant which represents the dephasing that occurs due to the pulse errors and t_c is the time between every 2 echoes (the cycle time). For $n << T_{2,\text{pulse}}/t_c$ the CPMG and CP sequences perform roughly the same as an identity operation, while for $n >> T_{2,\text{pulse}}/t_c$ the σ_y operator becomes significant, causing the CP sequence to retain no initial magnetization. Note that the probabilities are now a function of cycle number to reflect the distinction that T_2 is independent of echo spacing, while $T_{2,\text{pulse}}$ is not. The constants, $c_{I,x,y,z}$, determine the asymptotic behavior of the channel and represent loss of visibility. At the cost of losing information about the initial magnetization oscillations present in any CPMG sequence, the constants c_x and c_z are taken to be independent of n, such that the overall loss of visibility due to pulse errors is still retained. The asymptotically retained magnetization for a CPMG sequence is given by $M_\infty = c_I + c_y - (c_x + c_z)$ and the rate at which a CP sequence would lose signal is given by $T_{2,\text{pulse}}$. M_∞ and $T_{2,\text{pulse}}/t_c$ are two numbers that allow us to completely and compactly characterize refocusing pulses for use in multiple refocusing sequences. The ideal refocusing pulse has $T_{2,\text{pulse}}/t_c \to \infty$ and $M_\infty \to 1$.

The result of a Pauli channel fit for CPMG sequences using the four pulses previously compared in section 6.5 is displayed in fig. 6-8. All pulses were restricted to a maximum amplitude of $A_{\max}/2\pi = 5$ kHz and were simulated over $|\Delta\omega| \leq 1.6\ A_{\max}$ and $\pm 10\%$ drive field inhomogeneity ($\omega_1 = 0.9 - 1.1$). The difference in refocusing ability for each pulse is clearly distinguishable (see table 6.1).

Pulse	$T_{2,\text{pulse}}/t_c$	M_∞
Chirp	9 cycles	0.997
Non-symmetrized OCT	6 cycles	0.991
Symmetrized OCT	3 cycles	0.981
Hard	1 cycle	0.646

Table 6.1: Dephasing rate and asymptotically retained magnetization for CPMG sequences using four different types of refocusing pulses.

6.6.3 Validity of Pauli Channel Model

A Pauli channel model is an excellent description of CPMG dynamics due to both the refocusing being about a single cartesian coordinate and the averaging being complete enough over the distribution in question to suppress the off-diagonal components of the superoperator (eq. 6.14). A superoperator that may be accurately represented as a Pauli channel must be diagonal in the Pauli basis. This requirement is derived by noting that a Pauli channel (as defined by eq. 6.17) does not mix the components of the input state. For example, for each orthogonal input state (σ_x, σ_y, and σ_z) the output from the channel will remain either σ_x, σ_y, or σ_z, but with a scaling factor. In general, though, for an arbitrary distribution, $P(\Delta\omega, \omega_1)$, and a refocusing pulse about an arbitrary axis, the superoperator describing the dynamics in the Pauli basis will contain off-diagonal components. This can be seen by considering that for each element of the distribution, the cycle propagator is of the general form

$$U_{\text{cycle}}(\Delta\omega, \omega_1) = e^{-i\frac{\theta(\Delta\omega,\omega_1)}{2}\hat{r}(\Delta\omega,\omega_1)\cdot\vec{\sigma}}. \tag{6.20}$$

The resulting density matrix after n applications of the cycle, for an uncorrelated initial state ρ_{in}, is then given by

$$\begin{aligned}\rho_{\text{out}}^{(n)} = \int P(\Delta\omega,\omega_1)\Big[&\cos^2\frac{n\theta}{2}(\mathrm{I}\,\rho_{\text{in}}\,\mathrm{I}) + i\sin\frac{n\theta}{2}\cos\frac{n\theta}{2}(\mathrm{I}\,\rho_{\text{in}}\,\widehat{r}\cdot\vec{\sigma}) - \\ &i\sin\frac{n\theta}{2}\cos\frac{n\theta}{2}(\widehat{r}\cdot\vec{\sigma}\,\rho_{\text{in}}\,\mathrm{I}) + \sin^2\frac{n\theta}{2}(\widehat{r}\cdot\vec{\sigma}\,\rho_{\text{in}}\,\widehat{r}\cdot\vec{\sigma})\Big]\,\mathrm{d}\Delta\omega\,\mathrm{d}\omega_1.\end{aligned} \tag{6.21}$$

This equation is an expansion of eq. (6.20) inserted into eq. (6.14). The dependence of θ and $\widehat{r}$ on $\Delta\omega$ and ω_1 has been dropped for clarity and the argument $n\theta$ is taken to be modulo 2π. As noted in Ref. [92] using analysis in SO(3), if after a certain number of cycles the range $\theta = [0, 2\pi]$ is sampled uniformly over $\Delta\omega$ and ω_1, eq. (6.21) reduces to

$$\rho_{\text{out}} = \int P(\Delta\omega,\omega_1)\left[\frac{1}{2}(\mathrm{I}\,\rho_{\text{in}}\,\mathrm{I}) + \frac{1}{2}(\widehat{r}\cdot\vec{\sigma})\,\rho_{\text{in}}\,(\widehat{r}\cdot\vec{\sigma})\right]\mathrm{d}\Delta\omega\,\mathrm{d}\omega_1. \tag{6.22}$$

The integrand may be expanded as

$$\begin{aligned}&\frac{1}{2}(\mathrm{I}\,\rho_{\text{in}}\,\mathrm{I}) + \frac{1}{2}\Big[r_x^2\,(\sigma_x\rho_{\text{in}}\sigma_x) + r_y^2\,(\sigma_y\rho_{\text{in}}\sigma_y) + \\ &r_z^2\,(\sigma_z\rho_{\text{in}}\sigma_z) + r_x r_y\,(\sigma_x\rho_{\text{in}}\sigma_y) + r_x r_z\,(\sigma_x\rho_{\text{in}}\sigma_z) + r_y r_x\,(\sigma_y\rho_{\text{in}}\sigma_x) + \\ &r_y r_z\,(\sigma_y\rho_{\text{in}}\sigma_z) + r_z r_x\,(\sigma_z\rho_{\text{in}}\sigma_x) + r_z r_y\,(\sigma_z\rho_{\text{in}}\sigma_y)\Big].\end{aligned} \tag{6.23}$$

The same result may be arrived at by computing the eigenvalues of the Choi matrix, as outlined in [81].

The averaging of the off-diagonal elements of the superoperator in the product operator basis - elements of the form $\sigma_i\rho_{\text{in}}\sigma_j$, where $i \neq j$ - is dependent upon the distribution and refocusing pulse in question. The inhomogeneity we consider here is symmetric about the on-resonance Larmor precession frequency such that the average of r_z over $\Delta\omega$ and ω_1 will tend toward zero. Additionally, field inhomogeneities tend to tip the effective rotation axis of a refocusing pulse out of the transverse plane while minimally affecting the orientation in the transverse plane. Since we are considering a y-axis pulse, r_x will tend to be small for all values of $\Delta\omega$ and ω_1. Thus, the only

terms to be significant in eq. (6.23) will be $r_{x,y,z}^2$ such that the dynamics is given by a Pauli channel to a high degree of accuracy.

In the case of our OCT CPMG cycle, as shown in fig. 6-10, $\hat{r} \cdot \vec{\sigma}$ is very nearly σ_y for all $\Delta\omega$ and ω_1 and the variation in θ across $\Delta\omega$ and ω_1 is such that after roughly 30 cycle applications the averaging is complete enough that the map is given almost entirely by $\mathrm{I}\rho_{\mathrm{in}}\mathrm{I}$ and $\sigma_y\rho_{\mathrm{in}}\sigma_y$ with equal probabilities. For the field inhomogeneities considered here ($|\Delta\omega/2\pi| \leq 8$ kHz and $\omega_1 = 0.9 - 1.1$), the model is an excellent description of the dynamics, with a trace overlap of greater than 0.9999 between the fitted and simulated superoperators for all cycles. Even for the case of hard pulses where the variation of r_y and θ is large over a single cycle (see fig. 6-10), the trace overlap is still greater than 0.999 for all cycles.

6.7 Discussion

The performance of OCT pulses with respect to the CPMG criteria demonstrates a significant reduction in the variation of the net nutation angle and direction of the rotation axis over the optimization range when compared to a hard pulse. Although the variation is not fully eliminated, we were able to find a pulse which refocuses over 99% of the initial magnetization over a range of frequency offsets 4 times the maximum amplitude of the drive ($\pm$10 kHz) for uniform drive field. In the case when the drive field has an amplitude distribution of $\pm$10%, we were able to find a pulse that refocuses over 99% of the initial magnetization over a frequency range of 3.2 times the maximum drive amplitude ($\pm$8 kHz). The spin dynamics are well described as a Pauli channel, which provides a compact form to predict the performance of multiple pulses, both for CP and CPMG sequences, and allows the performance of the refocusing pulses to be succinctly described by only two parameters: the asymptotic visibility, M_∞, and the pulse-induced dephasing time, $T_{2,\mathrm{pulse}}$, of the sequence.

Potential applications of the methods described in this chapter include minimizing T_1 contamination during pulsing by limiting the allowed trajectories on the Bloch sphere, eliminating transients by designing pulses that dephase immediately due to

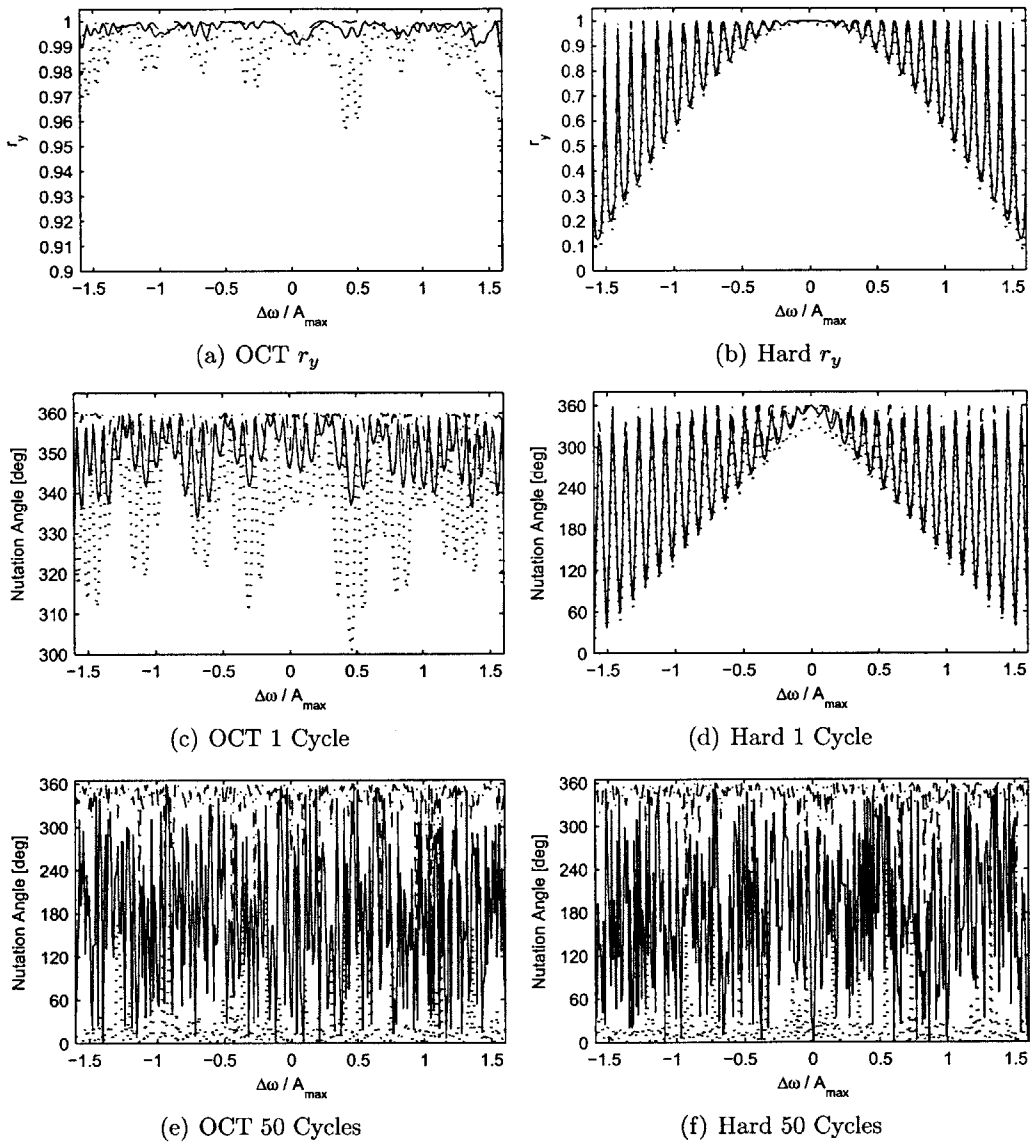

(a) OCT r_y (b) Hard r_y

(c) OCT 1 Cycle (d) Hard 1 Cycle

(e) OCT 50 Cycles (f) Hard 50 Cycles

Figure 6-10: Decomposition of the propagator characterizing a cycle $[\tau - \pi_y - 2\tau - \pi_y - \tau]$ with OCT pulses (left) and standard hard pulses (right) versus resonance offset. The top panels show the projections of the net rotation axis onto the $\widehat{y}$ axis, the middle panels the nutation angle for a single cycle, and the bottom panels the effective nutation angle for 50 cycles. In each panel, the solid line is the response for uniform drive ($\omega_1 = 1$), while the dashed (dotted) lines indicate the maximum (minimum) over the range of $\omega_1 = 0.9$ - 1.1. The OCT pulse was optimized over $|\Delta\omega| \leq 1.6\ A_{\max}$ with a uniform range of $\omega_1 = 0.9$ - 1.1. For this calculation τ was set to 1 ms. Note that in the top two panels, the scales for the OCT and hard pulses are different.

pulse errors (i.e. $T_{2,\text{pulse}} = 0$), increasing bandwidth by directly optimizing the rotation axis over a cycle, sculpting response of excitation pulses to directly match the rotation axis of the CPMG cycle for each element of the field distribution, and systematically optimizing SNR by examining the maximum bandwidth achievable for a variety of pulse lengths.

Chapter 7

Robust Qubit Storage: XY-Type Sequences and Logical Encodings

The CPMG sequence provides good decoupling properties for an arbitrary noise process, but accumulation of pulse errors causes only one orthogonal component of the input state to be retained. To achieve a robust qubit storage operation that treats all input states symmetrically, modifications to the CPMG sequence are required. One sequence for achieving a storage operation robust to pulse errors is the XY-4 sequence, a modified CPMG sequence consisting of repeated applications of a four-pulse cycle of equally spaced refocusing pulses with phases $XYXY$ [141]. Pulse errors for the XY-4 sequence come in at second order, as opposed to first order for the CPMG sequence. Enhanced robustness to pulse errors may be achieved by constructing higher order sequences built off of the XY-4 primitive. In this chapter we discuss the construction of XY-type sequences, and demonstrate how ideas from quantum information theory, such as logical encodings and twirling, may be used to further suppress pulse errors in XY-type sequences to implement a robust quantum memory.

7.1 Constructing Supercycles to Suppress Pulse Errors

Enhanced performance of decoupling sequences may be achieved by creating supercycles out of a primitive rotation and is the basis for MLEV sequences [125] often used for broadband spin decoupling [217]. The construction of supercycles has been later formalized to a systematic procedure [217, 126] and used to derive new robust decoupling sequences, such as WALTZ-16 [180]. The procedure begins with a primitive operation, R_1, that gives a good approximation to an identity operation. Assuming only unitary errors, this operation may be parameterized as a small rotation of angle ϕ_1 about some axis $\hat{n}_1$,

$$R_1 = \mathbb{I} e^{-i\phi_1 \hat{n}_1 \cdot \vec{I}}. \tag{7.1}$$

Two basic operations that have been applied to form compensation sequences to be concatenated with the primitive operation: *cyclic permutation* and *conjugation.* As for any rotation operator, the primitive operation may be decomposed into a series of rotations. We call the last of these rotations R_0, characterized by a rotation angle ϕ_0 about axis $\hat{n}_0$. The cyclic permutation operation consists of conjugating R_1 by R_0,

$$R_1^* = R_0 R_1 R_0^\dagger, \tag{7.2}$$

with the result being the cyclic permutation of R_0 from the end of the primitive to the beginning. Assuming ϕ_1 to be small, the effect of concatenating the primitive with the cyclic permutation compensation sequence is, to first order:

$$R_1 R_1^* \approx \mathbb{I} + \phi_1(\hat{n}_1 + \hat{n}_1^*) \cdot \vec{I}. \tag{7.3}$$

The correction is maximized if ϕ_0 and $\hat{n}_0$ are chosen such that $\hat{n}_1^* = -\hat{n}_1$.

The conjugation operation inverts all phases of the primitive:

$$\overline{R}_1 = R_z R_1 R_z^\dagger, \tag{7.4}$$

where

$$R_z = e^{-i\pi I_z}. \tag{7.5}$$

The first order effect of concatenating the primitive with the conjugate compensation sequence is

$$R_1 \overline{R}_1 \approx \mathbb{I}\phi_1 n_{1z} I_z. \tag{7.6}$$

The conjugation operation corrects for primitive errors along the x and y axes, with the effect maximized if the primitive z-axis error, n_{1z}, is small. Sequentially applying these two compensation operations suppresses pulse errors in a given primitive to increasingly high order.

7.1.1 Constructing a Primitive Operation

When building a primitive out of a given imperfect π-angle refocusing pulse, there are many methods to choose from, with three being prominently investigated. In the following we adopt the shorthand notation of X to denote an ideal π-angle rotation about the x-axis with a corresponding error of rotation angle ϵ about an arbitrary unit Bloch vector, $\hat{n}$, taken to operate immediately before the ideal pulse:

$$X = e^{-i\pi I_x} e^{-i\epsilon(n_x I_x + n_y I_y + n_z I_z)}. \tag{7.7}$$

The first option is to simply apply the rotation twice, $R_1 = XX$, as in the CPMG sequence. By commuting the errors through the ideal π rotations, we may write

$$R_1^{CPMG} = e^{-i\pi I_x} e^{i\pi I_x} e^{-i\epsilon(n_x I_x - n_y I_y - n_z I_z)} e^{-i\epsilon(n_x I_x + n_y I_y + n_z I_z)}. \tag{7.8}$$

Now assuming ϵ to be small, we keep only the leading order terms of a BCH expansion of the propagator, $e^A e^B = e^{A+B+\frac{1}{2}[A,B]+\cdots}$, to give

$$R_1^{CPMG} \approx \mathbb{I} e^{-i2\epsilon n_x I_x}. \tag{7.9}$$

Errors along the axis of rotation come in at first order in ϵ and quickly accumulate, leading to the fast decay of input states orthogonal to the axis of rotation characteristic of the CPMG sequence.

The second option is to apply the refocusing pulse followed immediately by its phase-inverted rotation, $R_1 = X\overline{X}$. Repeated applications of this primitive give the phase-alternated CP sequence [75]. The complete action of this primitive may be written as

$$R_1^{PACP} = e^{-i\pi I_x} e^{i\pi I_x} e^{-i\epsilon(n_x I_x - n_y I_y - n_z I_z)} e^{-i\epsilon(-n_x I_x - n_y I_y + n_z I_z)}. \tag{7.10}$$

To first order in ϵ, we see a similar error to the CPMG case, but phase-shifted:

$$R_1^{PACP} \approx \mathbb{I} e^{i2\epsilon n_y I_y}. \tag{7.11}$$

Due to errors normally being concentrated about the axis of refocusing, n_y will tend to be relatively small, leading to this sequence performing slightly better than the CPMG sequence for inputs orthogonal to I_y. However, since the errors still come in at first order in ϵ, they accumulate too quickly to effectively store a general quantum state.

A better option is the XY-4 sequence, $R_1^{XY-4} = XYXY$. To demonstrate the enhanced robustness of the XY-4 sequence, we consider the same general error on the X gate and assume phase shifts may be performed accurately, giving

$$Y = e^{-i\pi I_y} e^{-i\epsilon(n_y I_x - n_x I_y + n_z I_z)}, \tag{7.12}$$

and a total action of

$$\begin{aligned} R_1^{XY-4} =& e^{-i\pi I_x} e^{-i\pi I_y} e^{-i\pi I_x} e^{-i\pi I_y} e^{-i\epsilon(n_x I_x - n_y I_y - n_z I_z)} e^{-i\epsilon(-n_y I_x + n_x I_y + n_z I_z)} \\ & \times e^{-i\epsilon(-n_x I_x + n_y I_y - n_z I_z)} e^{-i\epsilon(n_y I_x - n_y I_y + n_z I_z)} \end{aligned} \tag{7.13}$$

The leading term in the BCH expansion is now

$$R_1^{XY-4} \approx \mathbb{I} e^{-2i\epsilon^2(n_x^2-n_y^2)I_z}. \tag{7.14}$$

The ideal propagator for the primitive is the identity operation, with the error coming in symmetrically at second order in ϵ.

7.1.2 Construction of Higher-Order XY-Type Sequences

The supercycle approach may be used to further suppress errors in the XY-4 sequence to derive the XY-8 and XY-16 sequences [76]. For the XY-8 sequence, $R_0 = e^{-i\pi I_y}$, yielding

$$R_1^* = Y(XYXY)\overline{Y} = YXYX \tag{7.15}$$

to give the XY-8 sequence, $R_1^{XY-8} = XYXYYXYX$, where the action of the cyclic permutation is to suppress the second order errors in I_x and I_z. The leading term in the BCH expansion of the XY-8 propagator is

$$R_1^{XY-8} \approx \mathbb{I} e^{-2i\epsilon^3(n_x^3-n_x n_y^2)(I_x+I_y)}. \tag{7.16}$$

The XY-16 sequence then appends to the XY-8 sequence a phase inverted XY-8, further suppressing errors. The final XY-16 sequence is then

$$XY-16 \rightarrow XYXYYXYX\overline{XYXYYXYX} \tag{7.17}$$

with a leading order term in the BCH expansion of

$$R_1^{XY-16} \approx \mathbb{I} e^{-2i\epsilon^4(n_x^3 n_y-n_x n_y^3)I_z}. \tag{7.18}$$

The dominant I_z error comes in at fourth order in ϵ, leading to a high-degree of rubustness to pulse errors. However, for a sufficiently large number of cycle applications a cumulative rotation about the z axis still occurs, causing a significant

deviation from the desired identity operation.

7.2 Pauli Channel Representation of Errors

In a similar manner as was demonstrated for the CPMG sequence (Section 6.6.2), the accumulation of pulse errors in the XY-type sequences may be compactly analyzed using a Pauli channel representation (Section 2.1.3). The action of the XY-type sequences may be described as transforming the dephasing of the CPMG sequence about a preferential axis into a depolarizing channel that acts symmetrically over all input states. Figure 7-1 demonstrates how sequences of increasing complexity lead to a better Pauli channel, as measured by diamond norm distinguishability [110, 216] between the full superoperator and the Pauli channel representation. As shown in Figure 7-3, however, this desirable property of the XY-type sequences is only valid for a limited number of cycles, when the σ_z errors have not yet significantly accrued.

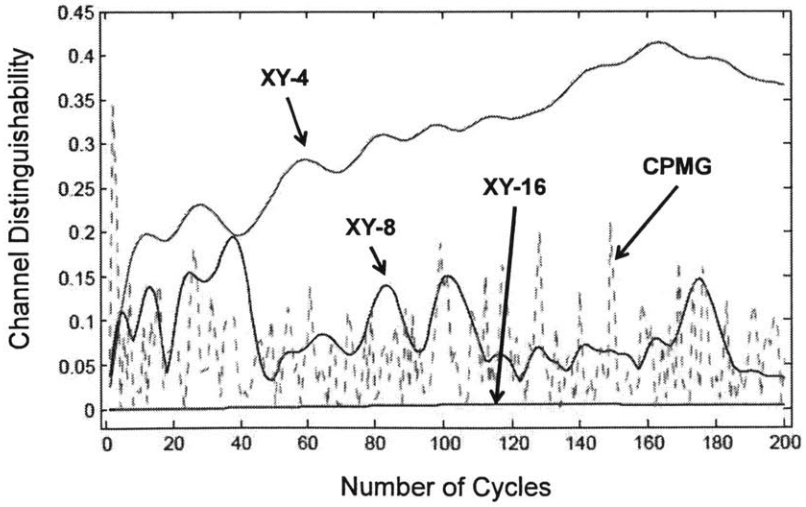

Figure 7-1: Diamond norm distinguishability from a Pauli channel as a function of the number of applied cycles for various decoupling sequences. As the complexity of the cycle increases (from CPMG to XY-16), the resulting channel becomes more accurately representable as a Pauli channel.

7.3 Twirling The XY-16 Sequence

Concepts similar to the twirling of a noise process [59] may be used to reduce and symmetrize the effects of pulse errors in the XY-16 sequence, providing enhanced performance. We start by noting that the XY-16 sequence acts as a dephasing channel about the z-axis. To symmetrize the channel, we desire a pulse which operates on the sequence to implement cycles of three periods of dephasing about the x, y, and z axes, respectively. The overall channel will then look depolarizing. Any rotation which maps Pauli operators to Pauli operators in an irreducible cyclic permutation will suffice. One example is a Clifford group element [26] which implements a rotation of $\frac{2\pi}{3}$ about the *magic state* with Bloch vector $\frac{1}{\sqrt{3}(1,1,1)}$:

$$R = e^{-i\frac{\pi}{3\sqrt{3}}(\sigma_x+\sigma_y+\sigma_z)}. \tag{7.19}$$

This rotation corresponds to a quantum operation, $\mathcal{R}(\rho) = R\rho R^\dagger$, that has the following action on the Pauli operators:

$$\begin{aligned} \mathcal{R}(X) &= Y \\ \mathcal{R}(Y) &= Z \\ \mathcal{R}(Z) &= X. \end{aligned} \tag{7.20}$$

The effective geometric twirl is shown in Figure 7-2.

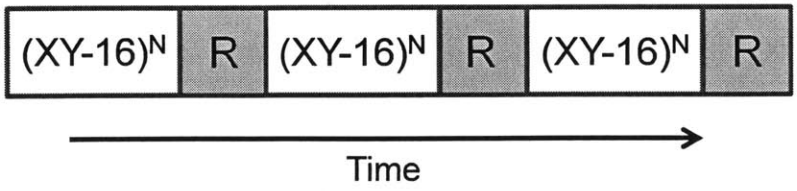

Figure 7-2: Sequence to perform a geometric twirl of pulse errors in the XY-16 sequence. A magic angle rotation (see main text) is performed after each XY-16 sequence consisting of N cycles. Note that the twirling pulse is applied only three times, mitigating the accumulation of errors associated with its implementation.

7.3.1 Simulated Twirl

To demonstrate the action of the twirling operation, the XY-16 sequence was simulated over a static distribution of resonance offsets and control amplitude variations with and without twirling. The total system Hamiltonian may be written as the sum of a drift Hamiltonian, H_d, taken to be time-independent on the time-scale of the experiment and a control Hamiltonian, $H_c(t)$, whose amplitude may be changed during the experiment:

$$H_{sys}(t) = H_d + H_c(t). \tag{7.21}$$

The incoherent noise is taken to act independently on each Hamiltonian, leading to a spread of the drift energy parameterized by a particular deviation value, $\Delta\omega$, from a nominal energy splitting, ω_0, and a particular scaling factor, ω_1, of the control amplitudes, $A(t)$:

$$H_d(\Delta\omega) = \frac{1}{2}(\omega_0 + \Delta\omega)\sigma_z, \tag{7.22}$$

and

$$H_c(\omega_1, t) = \omega_1 A(t)(\cos(\omega_t t + \phi(t)))\sigma_x, \tag{7.23}$$

where $\phi(t)$ is a time-dependent phase control that is taken to be noiseless and ω_t is the carrier frequency of the control modulation. Assuming the controls are applied on-resonance with the nominal energy splitting, setting $\omega_t = \omega_0$, and taking a rotating-wave approximation yields

$$H_{sys}(\Delta\omega, \omega_1, t) = \frac{1}{2}\Delta\omega\sigma_z + \frac{1}{2}\omega_1 A(t)(\cos(\phi(t))\sigma_x + \sin(\phi(t))\sigma_y). \tag{7.24}$$

The performed simulations assume perfect state preparation and measurement, with control provided by pulses of length 13 μs with constant amplitude and constant phase set to either $\phi = 0, \pi/2, \pi, 3\pi/2$ for X, Y, $\overline{X}$, and $\overline{Y}$ pulses, respectively. The delay between pulses was taken to be $2\tau = 200\mu$s and the incoherence was $\Delta\omega/2\pi = \{$-8 kHz, 8 kHz$\}$ in steps of 200 Hz and $\omega_1 = (0.95, 1\ 1.05)$. The cycle superoperator over the incoherent distribution was calculated as described in Section 2.3. The twirling

pulses were taken to act instantaneously and ideally, as any imperfections in these pulses may be absorbed into the errors that occur during the XY-16 sequence.

The simulation results are shown in Figure 7-3. In the absence of the twirling pulse, the expected dephasing Pauli channel about σ_z is shown, with the amplitudes of σ_x and σ_y error operations remaining vanishingly small. When the twirling pulses are included, the amplitudes of each of the errors become nearly identical over all cycles and become smaller, due to the larger error about a single axis now being spread equally over all three axes. Additionally, the amplitude of the identity operation remains larger than for the non-twirling case, indicating that by spreading out the errors, their effect has actually been reduced.

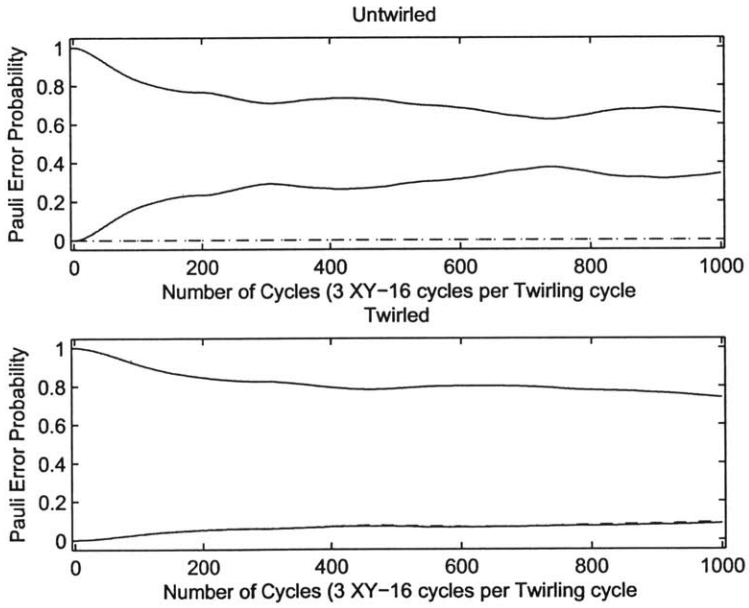

Figure 7-3: Result of an ideal twirl of an XY-16 sequence composed of hard pulses. The probability of each Pauli error occuring as a function of the number of cycles contained in each XY-16 sequence are plotted in the absence of twirling (top plot) and in the presence of twirling (bottom plot). In the untwirled case, the σ_z error is dominant, rising in probability as the number of cycles is increased. The σ_x and σ_y error probabilities remain small throughout the examined number of cycles. When twirling is applied, the error probabilities of each Pauli operator become nearly identical over all numbers of cycles considered.

7.4 Logical Encoding for Pulse Errors

A decoherence-free subspace (DFS) encoding is a class of noiseless quantum codes which provide infinite distance correction for errors with appropriate symmetry. DFS encodings are a generalization of the use of zero-quantum coherences in NMR spectroscopy and imaging [79, 215] and were suggested in for use in quantum information processing as a means of suppressing noise acting collectively on a number of qubits [225, 53, 127]. They have since been formalized in the language of quantum error correction as a subclass of noiseless subsystem passive error correcting codes [112, 224]. Many experimental demonstrations of DFS encodings exist, including implementations in NMR [62, 84, 32], quantum optics [119], and trapped ions [108]. They have even been used as motivation for the design of an experimental apparatus in neutron interferometry [165]. Here we provide a new application of a DFS to remove the effect of pulse errors which accrue during application of a decoupling sequence.

Mitigating the effect of cumulative pulse errors in lengthy control sequences has motivated arguments for reducing the number of refocusing pulses applied in a decoupling sequence [206]. For a given target decoupling time the application of fewer refocusing pulses necessarily implies a longer wait time between refocusing pulses, leading to decreased robustness to noise with correlation time on the order of the pulse spacing [31] and increased sensitivity to diffusive-like processes [190]. Experimentally, it is common practice to minimize the time between application of refocusing pulses subject to the constraints of sample heating and amplifier capacity. The use of a DFS encoding with a CPMG or XY-type sequence permits refocusing of stochastic environmental errors while preventing the accumulation of pulse-induced control errors throughout the sequence.

7.4.1 Requirements for Existence of a Logical Encoding

We consider a general case of two noisy qubits quantized in a large static magnetic field along the laboratory $\hat{z}$ direction and coupled by an exchange interaction – the same arguments may be made for other couplings, such as a dipolar coupling. The

drift Hamiltonian is given by

$$H_d = \frac{\omega_0^A(t)}{2}\sigma_z^A + \frac{\omega_0^B(t)}{2}\sigma_z^B + \frac{\pi J(t)}{2}\sigma^A \cdot \sigma^B, \tag{7.25}$$

where ω_0^A and ω_0^B are the Larmor frequencies dictating the interaction strength of qubit A and B, respectively, with the static quantizing field, and J is the strength of the exchange coupling. As discussed in Section 2.4, the time-dependence of each parameter is determined by a set of multi-point correlation functions, which for stationary, zero mean, Gaussian noise may be characterized by a single two-point correlation funtion, $G(\tau)$, and corresponding correlation time, τ_c, dictating the noise memory. For simplicity of our initial argument the coupling will be taken to be zero. In this case, the Hamiltonian may be written as

$$H_d = \frac{\omega_+(t)}{2}(\sigma_z^A + \sigma_z^B) + \frac{\omega_-(t)}{2}(\sigma_z^A - \sigma_z^B), \tag{7.26}$$

where

$$\omega_+(t) = \frac{\omega_0^A(t) + \omega_0^B(t)}{2} \tag{7.27}$$

and

$$\omega_-(t) = \frac{\omega_0^A(t) - \omega_0^B(t)}{2}. \tag{7.28}$$

We assume that the noise acts collectively on the two qubits such that $\omega_-(t) = 0$ for all time. The resulting noise generator is then simply the total spin angular momentum operator along the $\hat{z}$ direction, $J_z = \sigma_z^A + \sigma_z^B$. The interaction algebra, $\mathcal{A}$, generated by this error operator yields the set of possible errors which may occur [112]. $\mathcal{A}$ may be explicitly evaluated by taking progressive powers of J_z with the identity operator, $\mathbb{I}$. The resulting interaction algebra contains three unique operators: $\mathbb{I}$, $\sigma_z^A + \sigma_z^B$, and $\sigma_z^A\sigma_z^B$. In order to define a DFS for this interaction algebra, the basis states for logical qubits must be drawn from the *commutant* of $\mathcal{A}$ – the set of operators which commute with $\mathcal{A}$ and are left invariant under the noise. To properly define a qubit, we additionally require that a subset of the commutant of $\mathcal{A}$ satisfy the spin-1/2

Pauli commutation relations. An appropriate set of states is:

$$\begin{aligned}
\mathbb{I}^L &= (\mathbb{I}^A\mathbb{I}^B - \sigma_z^A\sigma_z^B)/2, \\
\sigma_x^L &= (\sigma_x^A\sigma_x^B + \sigma_y^A\sigma_y^B)/2, \\
\sigma_y^L &= (\sigma_x^A\sigma_y^B - \sigma_y^A\sigma_x^B)/2, \\
\sigma_z^L &= (\sigma_z^A - \sigma_z^B)/2,
\end{aligned} \tag{7.29}$$

where the superscript L denotes a Pauli operator acting on the logical space. This set of states is not unique, but satisfies the two requirements of being in the commutant of $\mathcal{A}$ and yielding the correct Pauli commutation relations for a qubit.

In the absence of any other interactions, the above $\mathrm{DFS_Z}$ encoding is perfectly protected against the noise. Regardless of the strength or correlation time of the noise, it has no effect on the defined subspace. However, if we reintroduce the second term of the Hamiltonian, $\omega_-(t)(\sigma_z^A - \sigma_z^B)$, the symmetry is broken and the error interaction algebra is modified. If we make the simplification that ω_- is time-independent and single-valued, the effect is a simple rotation within the logical subspace – due to the reintroduced term corresponding to a σ_z^L operation. Experimentally, however, this simplification is invalid and the assymmetric term must be refocused in analogy with a usual spin echo for a single qubit.

We assume that a control field may be applied that acts identically on the two qubits, with rotating frame Hamiltonian

$$H_c = \omega_1(t)\left[\cos(\theta(t))(\sigma_x^A + \sigma_x^B) + \cos(\theta(t))(\sigma_y^A + \sigma_y^B)\right]. \tag{7.30}$$

The terms $\sigma_x^A + \sigma_x^B$ and $\sigma_y^A + \sigma_y^B$ are not contained within the commutant of $\mathcal{A}$ and so introduction of this Hamiltonian, while necessary not only to refocus the assymetric term of the drift Hamiltonian but also to provide for universal control of the encoded qubit, induces *leakage* out of the protected subspace. A special case with no leakage occurs when a perfect π pulse about the $\hat{x}$ or $\hat{y}$ axis may be applied [31]. In this case, the effective propagator over the length of the pulse in the sense of Average Hamiltonian Theory [77] is given by $U = e^{-i\pi/2(\sigma_x^A + \sigma_x^B)} = -e^{-i\pi/2(\sigma_x^A\sigma_x^B)}$ or

$U = e^{-i\pi/2(\sigma_y^A + \sigma_y^B)} = -e^{-i\pi/2(\sigma_y^A \sigma_y^B)}$. Both of these correspond to rotations about the logical $\hat{x}$ operator and any leakage during application of the pulse is returned to the protected subspace at the end of the pulse.

Provided the noise fluctuates on a timescale long compared with the pulse length ($\tau_c >> t_p$), the leakage during the pulse does not cause decoherence and may be neglected. As discussed in Chapter 6 the errors associated with a non-ideal pulse correlate with the underlying distribution of drift and control Hamiltonian parameters, rendering the special case of a perfect π pulse invalid in practical implementations. For the general case of non-ideal pulses an appropriate compensation scheme must be applied to mitigate the effects of DFS leakage. In the following we assume the fluctuations of any noisy parameters are slow compared with both refocusing pulse lengths and the time delay between pulses, allowing us to treat the problem in terms of an incoherent distribution of static parameters.

7.4.2 A DFS for Pulse Errors

We once again assume a drift Hamiltonian of the form of eq. (7.26), but with an incoherent distribution over ω_+ and ω_- (see Section 2.3). A CPMG sequence applied simultaneously to each qubit refocuses both terms in the drift Hamiltonian. In the absence of coupling between the two qubits, the dynamics breaks into a direct sum structure and the error analysis of Section 6.6 may be applied to write the unitary action over n cycles of the CPMG sequence on a specific set of noise parameters as

$$U(\omega_+, \omega_-, n) \approx e^{-in\theta(\omega_+, \omega_-)(\sigma_y^A + \sigma_y^B)/2}. \tag{7.31}$$

Because we are assuming an incoherent distribution of the noise parameters, taking a convex operator sum over the full set of unitary propagators for each tuple of noise parameters leads to pulse-error induced decay of any operator not contained in the commutant of the interaction algebra generated by the dominant error: $J_y = \sigma_y^A + \sigma_y^B$. In analogy with the previously considered J_z error, the CPMG error interaction algebra contains predominantly the terms $\mathbb{I}^A\mathbb{I}^B$, $\sigma_y^A + \sigma_y^B$, and $\sigma_y^A \sigma_y^B$, and single qubit

logical operators which commute with this algebra may be defined:

$$\begin{aligned}
\mathbb{I}^L &= (\mathbb{I}^A\mathbb{I}^B - \sigma_y^A\sigma_y^B)/2, \\
\sigma_x^L &= (\sigma_x^A\sigma_z^B - \sigma_z^A\sigma_x^B)/2, \\
\sigma_y^L &= (\sigma_y^A - \sigma_y^B)/2, \\
\sigma_z^L &= (\sigma_x^A\sigma_x^B + \sigma_z^A\sigma_z^B)/2.
\end{aligned} \tag{7.32}$$

We now have an infinite distance QECC for J_y noise generators, meaning the code is valid for any number of cycles, n, of the CPMG sequence. Note that the robustness of this DFS_Y-CPMG sequence to noise in the drift and control Hamiltonians is equivalent to the robustness of the CPMG sequence on a single qubit. We are still requiring an average Hamiltonian over the cycle which is predominantly $J_y = \sigma_y^A + \sigma_y^B$, which requires the previously defined CPMG criteria to be satisfied (Section 6.1). Additionally, other terms in the error interaction algebra which were taken to be small, such as $\sigma_x^A \pm \sigma_x^B$ and $\sigma_z^A \pm \sigma_z^B$, cause leakage out of the DFS, but are bounded and do not accrue in analogy with the asymptotic stability of the expectation value of the component of spin magnetization aligned with the effective refocusing pulse axis in the single qubit CPMG sequence.

Thus far we have not considered the effect of the exchange coupling term. In the absence of the coupling term we do not have universal control over the two qubit system and may not initialize the system into the encoded subspace. However, this term generates a rotation within the coded subspace about either σ_x^L or σ_z^L – depending on whether a DFS_Z or DFS_Y encoding is used – and so must either be turned off or refocused. Assuming the distribution of coupling strengths is relatively small and static, π refocusing pulses about either σ_y^L or σ_x^L – again depending on the encoding used – may be applied halfway through the decoupling sequence and at the end of the sequence to refocus the logical rotation generated by the coupling. Any static variation of the coupling strength may be accounted for by designing an OCT pulse which operates with high fidelity over all values of the coupling. Because this pulse is only applied twice in the sequence the errors will not accrue.

By expanding the Hilbert space to include two qubits, a full logical qubit may now be defined by the states invariant under the pulse-induced errors of the sequence. In doing so, we have sacrificed the ability to have infinite depth protection from variations in the symmetric drift Hamiltonian term. However, this protection may be reintroduced by using a $\mathrm{DFS_Z}$ encoding and applying an XY-16 sequence instead of the CPMG sequence. As shown in Section 7.1.2 the action of the XY-16 sequence is to suppress pulse errors to fourth order and transform them to the $\hat{z}$ axis. The resulting error generator for the XY-16 sequence is then also J_z and the $\mathrm{DFS_Z}$ encoding accounts for both pulse errors and noise in the drift Hamiltonian. The disadvantage of this approach is greater sensitivity to variations of the pulse errors. Recall that, for the XY-16 sequence to operate correctly, the pulse errors must be constant over the entire 16 pulse cycle. The CPMG sequence has the advantage that the cycle length is significantly shorter (2 pulses). There is a trade-off, then, that dictates when each of the proposed sequence should be used:

- CPMG – appropriate for when robust efficient refocusing of a single component of a state is required.

- XY16 – appropriate for robustly storing an arbitrary quantum state for relatively short times.

- $\mathrm{DFS_Z}$-XY16 – appropriate for robustly storing an arbitrary quantum state for long times, especially when the noise in the drift Hamiltonian is so severe that it may not be directly refocused with a decoupling sequence, requiring the use of a DFS.

- $\mathrm{DFS_Y}$-CPMG – appropriate for robustly storing an arbitrary quantum state for long times, especially when the pulse errors fluctuate too quickly for application of an XY16 sequence.

Chapter 8

High-Fidelity Control with High-Q Resonators

In a common application of inductive manipulation and measurement of a quantum system, a tuned and matched resonator converts a pulsed electrical signal into a pulsed magnetic field and the resulting magnetic field produced by the quantum system back into an electrical signal. The same principles apply as well to capacitive coupling to electric fields. The conversion efficiency is determined by a number of factors, including the quality factor (Q) of the resonator, defined as the ratio of stored to dissipated energy in the resonant circuit. All other factors being equal, both the magnetic field strength resulting from the application of an electrical signal of a certain power and the signal-to-noise ratio (SNR) of an electrical signal induced by the magnetic response of the sample scale as $\sqrt{Q}$ [179, 1, 45, 169].

An important consequence of using tuned circuits is that any resonator has an associated ringdown time during which energy stored in the circuit dissipates. The signal to be observed from the quantum system is typically many orders of magnitude smaller than the control amplitudes, normally requiring a spectrometer deadtime of at least five times the ringdown time before receiver circuitry, such as low-power high-gain preamplifiers, can be switched on. When moving to a high-Q resonator to enable faster control and greater SNR, the relative amount of stored energy in the circuit increases, leading to longer ringdown and a deadtime that can exceed the

characteristic phase coherence time (T_2) of the quantum signal, significantly lowering measurement SNR and possibly preventing observation of the quantum signal at all. A dispersion of interaction strengths between quantum degrees of freedom in the sample may also lead to a spectral breadth which exceeds the resonator bandwidth of frequencies which are efficiently converted, preventing the rotation or detection of the entire spectrum with a single unoptimized pulse [88]. For these reasons it is common practice, especially in the field of pulsed electron spin resonance (ESR), to intentionally spoil the Q to reduce it to a value where these effects are no longer significant [170].

Another challenge inherent to the use of resonant circuits for pulse transmission is the distortions they produce of an ideal pulse waveform, once again due to the finite response time of the reactive elements used to construct a tuned circuit. For low values of Q (roughly 10 - 200), the effects of waveform distortions are relatively minor, resulting in a typical drop in pulse fidelity of a few percent [85]. However, as the Q is increased for applications that require high sensitivity the resonator distortions of the ideal waveform lead to a pulse action on the quantum system that differs drastically from a square pulse approximation.

Recent work proved that integration of a resonator impulse response function into an optimal control theory (OCT) pulse-design algorithm allows broadband excitation in pulsed ESR with limited power [193]. Here, we focus on applications that require a universal rotation that operates identically on all input states, particularly those that require a high Q resonator. Specifically, we describe how resonator distortions of an ideal waveform may be integrated into an optimal control theory (OCT) pulse-design algorithm to derive control sequences with limited ringdown that perform a target quantum operation with high fidelity. We experimentally verify the method by optimizing and implementing a bandwidth-limited OCT pulse, robust to static and microwave field inhomogeneity, which allows the observation of the free-induction decay (FID) of irradiated fused-quartz [57, 56] in a high-Q ($\approx$ 10,000) X-band ($\approx$ 10 GHz) rectangular cavity. We also consider a specific application of achieving universal control of a anisotropic-hyperfine coupled solid-state electron-nuclear spin system

via electron-only modulation even when the resonator bandwidth is significantly less than the hyperfine coupling strength. Through the derivation of example pulses, we demonstrate how the limitations imposed by linear response theory may be vastly exceeded when using a sufficiently accurate system model to optimize pulses of high complexity.

8.1 Resonator Model and Ringdown Suppression

Several models of the transient behavior of a resonator have been suggested and analyzed in detail [148, 8, 200], with various methods suggested for the suppression of pulse transients [210, 226, 211, 199]. We use the model of Barbara, *et al.* [8] consisting of a series RLC resonant circuit capacitively coupled to a voltage source through a real 50 Ohm impedance (Figure 8-1). We restate here the results of their analysis relevant to our integration of the model into an OCT algorithm, with further details available in the references.

The reactive elements necessary for efficient signal conversion have a finite response time to variations of the control signal, causing distortions of the ideal waveform. For a linear, time-invariant system, the waveform incident upon the quantum system, $y(t)$, is given by the convolution of the ideal control pulse, $x(t)$, with the impulse response, $h(t)$, of the transmitting circuit,

$$y(t) = h(t) * x(t) = \int_{-\infty}^{\infty} h(t-\tau)x(\tau)\,d\tau. \tag{8.1}$$

The impulse response gives a complete description of the transient behavior of the transmitting circuit and may be either inferred from measurement, or derived from an appropriate model. The ideal pulse is described as a time varying voltage of amplitude $v(t)$ and phase $\phi(t)$ applied at a driving frequency, ω_t:

$$V_s(t) = v(t)\cos\left(\omega_t t + \phi(t)\right). \tag{8.2}$$

When the driving frequency is set near resonance with energy level splittings of the

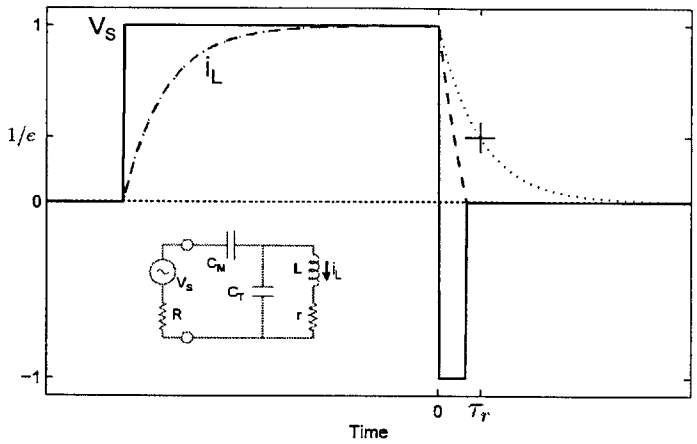

Figure 8-1: A general resonant transmission circuit may be modeled as a series tuned RLC circuit capacitively coupled to a time-varying voltage source [8] (inset). The quality factor (Q) of the resonator is given mainly by the circuit resonance frequency, $\omega_0 = 1/\sqrt{LC_T}$, the coil inductance,L, and the coil resistance, r: $Q \approx \omega_0 L/r$. The circuit impedance is matched to $R_0 = 50$ Ohms by varying the capacitances C_T and C_M. For high-Q resonators, the dominant transient response of the resonator to a square pulse input of voltage, V_S, (bold line) is an exponential rise (dashed line) and subsequent ring-down (dotted line) of the coil current, i_L, and resulting magnetic field. The ringdown may be suppressed by application of a phase inverted compensation pulse at the end of the square pulse to drive the coil current to zero. The characteristic transient ringdown time without compensation, $\tau_r = Q/\omega_0$, is denoted by a cross.

quantum system, the magnetic field induces transitions between the eigenstates of the system Hamiltonian. This model is representative of a general quantum control scenario and allows us to analytically understand the dynamics of high-Q resonators.

The resonator circuit response to an impulse of constant amplitude and phase may be determined by the application of Laplace transformation techniques [191]. The resulting filtered output waveform in the time domain is determined by the inverse Laplace transform, calculated via a partial fraction expansion, of the filtered waveform in the s-domain. The transient coil current, $i_L(t)$, which is proportional to the magnetic field applied to the sample, may be represented as a sum of poles, δ_k, and corresponding residues, d_k, after inverse Laplace transformation:

$$i_L(t) \propto \sum_k d_k e^{-\delta_k t}. \tag{8.3}$$

The four reactive elements in the circuit lead to four poles of the transfer function:

1. A steady-state oscillation at the driving frequency, ω_t.
2. An exponentially decaying DC transient.
3. An exponentially decaying oscillation at the probe free-ringing frequency, Ω.
4. An exponentially decaying oscillation at minus the probe free-ringing frequency, -Ω.

It is the third and fourth poles that are of most interest for determining the transient response of the circuit, as the DC transient is normally very small and the steady-state oscillation may be eliminated by moving into a reference frame rotating at the driving frequency. In a rotating wave approximation, this frame rotation also allows us to neglect the effect of the fourth pole.

The relevant third pole, δ_3, may be written as

$$\delta_3 = \delta_4^* = \gamma - i\omega_0 f\left(1 - \sqrt{\frac{r}{4R_0 f^2}}\right), \tag{8.4}$$

where $\gamma = \omega_0/Q$ is the rate of transient decay in terms of the inductor quality factor, $Q = \omega_0 L/r$, and

$$f = \sqrt{1 - \frac{1}{4Q^2}} \tag{8.5}$$

is a scaling factor determining how close the resonator free-ringing frequency, Ω, is to the tuned frequency, $\omega_0 = \sqrt{1/LC_T}$. For high-Q resonators, $r << R_0$, $\Omega \approx \omega_0$, and the transient oscillations in the rotating frame are critically damped. The resulting dynamics may then be approximated as a simple exponential ringup and ringdown of the pulse amplitude with time-constant

$$\tau_r = Q/\omega_0. \tag{8.6}$$

This time-constant differs from the commonly used $2Q/\omega_0$, which is valid only for an isolated series RLC circuit without the inclusion of a matching capacitor [148]. Such

approximations are used here only for the sake of argument and demonstration; when high-fidelity control of a particular system is desired the full form of the resonator transfer function must be experimentally determined.

Resonator ringdown may be suppressed by the application of a trailing compensation pulse of appropriate length and amplitude to drive the energy stored in the resonator to zero at the end of the pulse [89, 144]. As shown in Figure 8-1, this compensation pulse can significantly shorten the spectrometer deadtime, but at the expense of introducing an additional rotation to the quantum system. In the next section, we describe how the resonator transfer function and a ringdown compensation pulse may be integrated into an optimal control theory (OCT) algorithm to enable high-fidelity control even in the presence of transient effects and the additional rotation introduced by ringdown suppression.

8.2 Optimizing Bandwidth-Limited Controls

To include ringdown suppression and account for distortions of the ideal control parameters due to the limited bandwidth of a high-Q resonator we make several modifications to the OCT GRAPE algorithm outlined in Section 5.1.2. We first resample the control parameters to ensure the calculated propagators and gradients accurately reflect the distortions of the ideal control fields during periods when the applied control voltages are constant. For clarity, we define a *control period* as the time Δt during which the applied control voltage is constant, and a *evolution period* as the resampled time $\Delta t/n_s$ during which the control field seen by the quantum system is approximated as constant. Concretely, we begin with a set of undistorted controls, $\{u_k^j\}$, where $j = 1, ..., N$ and resample to obtain a new set of undistorted controls $\{\widetilde{u}_k^m\}$, where $m = 1, ..., M$ and $M = n_s N + n_r$ for n_s samples per N control periods and n_r values of zero appended to the waveform to account for pulse ringdown. We then define a mapping between the resampled undistorted controls and a new set of distorted controls, $\{\widetilde{v}_k^m\}_{m=1}^M$, given by the discrete convolution of the undistorted

controls with the resonator transfer function (8.1):

$$\widetilde{v}_k^m = h_k * \widetilde{u}_k^m = \sum_{l \leq m} h_k^{m-l+1} \widetilde{u}_k^l. \tag{8.7}$$

In contrast to the infinite-bandwidth case, the value of the control parameters during the m^{th} evolution period depends to a certain degree on the value of all previous controls. As a result, the gradient of the performance functional when control period j is perturbed depends on the change in the unitary propagator for all evolution periods $m > (j-1)n_s$. As derived in Appendix A the gradients for bandwidth-limited controls are

$$\frac{\delta\Phi}{\delta u_k^j} = \sum_{m>(j-1)n_s}^{M} \xi_k^m(j) \frac{\delta\Phi}{\delta \widetilde{v}_k^m}, \tag{8.8}$$

where $\xi_k^m(j)$ is the convolution of a top-hat function, Ξ, with the resonator response:

$$\xi_k^m(j) = \sum_{l \leq m} h_k^{m-l+1} \Xi(j, n_s). \tag{8.9}$$

The top-hat function, which is formally defined in Appendix A, accounts for the resampling of the control periods into evolution periods. The convolution of this function with the resonator impulse response may be interpreted as a weighting function of the gradients of all evolution periods affected by the perturbation of a given control period. The individual gradients of the evolution periods are

$$\frac{\delta\Phi}{\delta \widetilde{v}_k^m} = -2\text{Re}\left[\left\langle \widetilde{P}_m | i\frac{\Delta t}{n_s} H_k \widetilde{X}_m \right\rangle \left\langle \widetilde{X}_m | \widetilde{P}_m \right\rangle\right], \tag{8.10}$$

where $\widetilde{X}_m$ and $\widetilde{P}_m$ are defined in Appendix A. Note that pulse updating is done only for control periods, with evolution periods serving as a calculational tool.

Optimization of the compensation pulse for elimination of ringdown is performed as a sub-routine and is not considered in the calculation of the gradient direction. However, the compensation pulse is taken into account while calculating the total pulse fidelity and while performing a line search to optimize the step size in the gradient direction, ϵ. In practice, the line search is performed by choosing three values

of ϵ, optimizing the compensation pulse for each value, evaluating the fidelities of the resulting pulses, fitting to a quadratic, and taking the maximum value. The routine for the compensation pulse optimization may be implemented as a two-dimensional search over the length and amplitude of an appended final control period that minimizes the ringdown. An implementation of the GRAPE algorithm for bandwidth-limited control is described in Figure 8-2.

8.3 Optimization Results and Experimental Verification

Experiments were performed using a standard irradiated fused-quartz sample contained in a Varian E-231 rectangular cavity on a home-built X-band pulsed ESR spectrometer. The loaded quality factor and impulse response function of the cavity were measured by fitting an exponential to the rising and falling edges of a square pulse digitized with a pick-up coil inserted into a cavity iris opposite to the sample. Care was taken to only weakly couple the pick-up coil to the cavity fields in order to disturb the cavity mode structure as little as possible.

We measured a loaded Q of 8,486 for the Varian cavity, giving a ringdown time-constant of $\tau_r = 142$ ns at a resonance frequency of $\omega_0/2\pi = 9.5236$ GHz. The r^2 value of the exponential fit was 0.9804, verifying that modeling the transient behavior of our high-Q resonator as an exponential rise and fall of the field strength is a good approximation. We found that a spectrometer deadtime of 1.2 μs was required to allow the pulse ringdown to decay to a value below the spectrometer noise floor. The inhomogeneous phase coherence relaxation time of the sample, measured by observing a spin echo, was $T_2^* \approx 250$ ns, preventing us from observing a useful FID of the quartz sample when using an unoptimized pulse.

To observe the quartz FID we optimized a bandwidth-limited OCT pulse that performs a high-fidelity $\pi/2$ rotation about the x-axis robust to variations in the static and microwave fields. The resonator model discussed in Section 8.1 was included

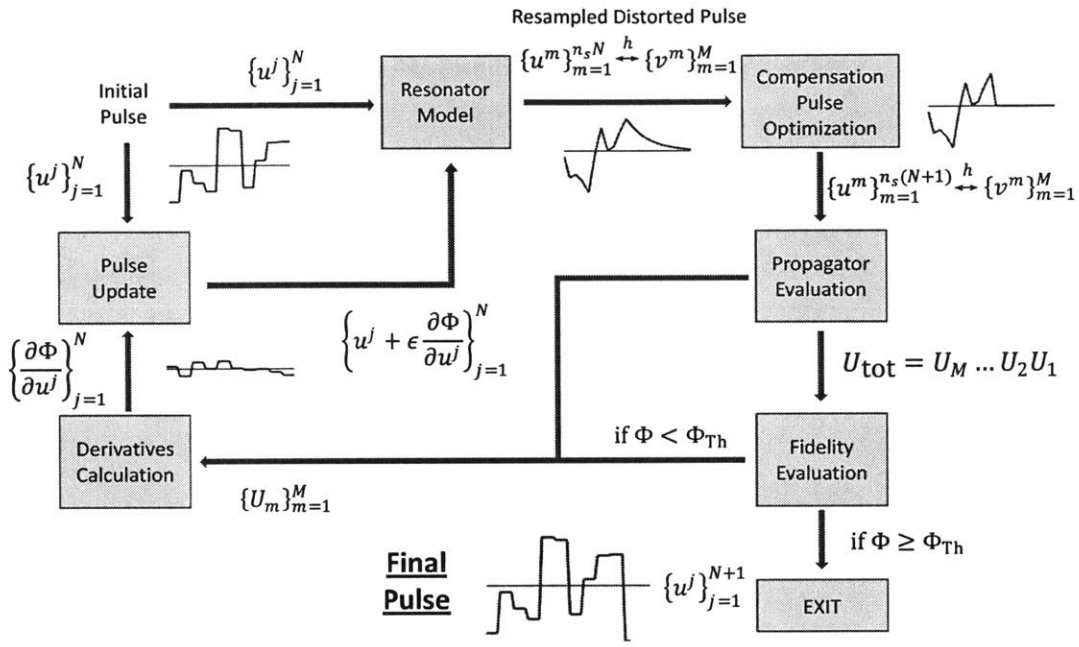

Figure 8-2: The bandwidth-limited GRAPE pulse optimization algorithm proceeds in a similar manner as for undistorted controls [105], with the resonator transfer function included in the calculation of the pulse propagator, average gate fidelity, and gradients. The notation is explained in the main text, with $k = 1$ for simplicity. An initial guess of control amplitudes is resampled and convolved with the resonator transfer function to yield a distorted set of control amplitudes including ringdown. A compensation pulse period is then optimized in a sub-routine and appended to the waveform to yield a distorted set of control amplitudes with minimized ringdown. The propagator for each evolution period of the distorted control amplitudes is then calculated and the average gate fidelity computed. The set of propagators is used to calculate the gradient direction of the fidelity with respect to the undistorted controls. A line search is then performed to optimize the step-size in the gradient direction. At each step of the line-search the sub-routines to calculate the updated distorted control amplitudes and corresponding compensation pulse are called, accounting for the compensation pulse not being included in the gradient calculation. The undistorted controls are then updated according to the gradient direction and step-size and the process iterates until a desired value of the fidelity is achieved.

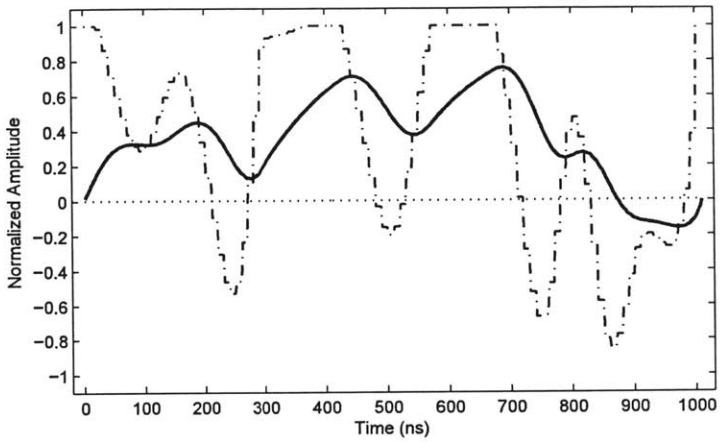

(a) Time-Domain Profile

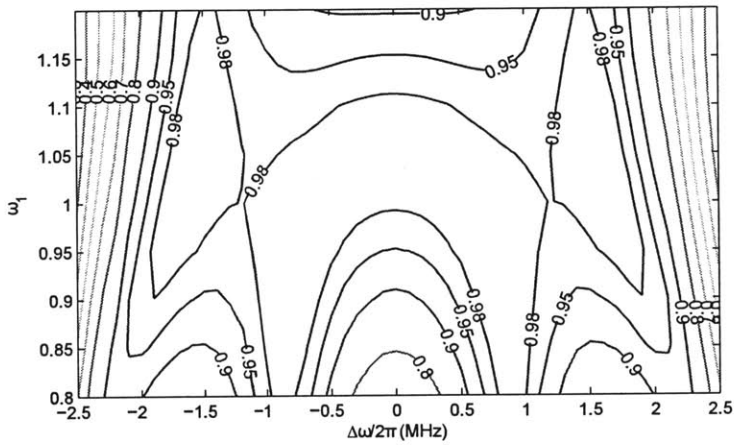

(b) Simulated Pulse Response

Figure 8-3: (a) Time-domain profile of a transients optimized OCT pulse with ringdown suppression implementing a $\pi/2)_x$ rotation robust to variations in the static and microwave field strengths. The dashed line represents the undistorted controls and the solid line represents the control fields seen by the spin system after transmission through a resonator with Q = 8,486. The control amplitudes are normalized to a nominal Rabi frequency of $\omega_{1,\mathrm{nom}}/2\pi = 5.26$ MHz. Optimization parameters and further details are discussed in the main text. Note that this pulse is phase-refocused, in that all spins in the sample are rotated with the same phase. (b) Simulated pulse fidelity over an extended range of static and microwave field inhomogeneities, demonstrating the robustness of the pulse.

in the optimization, as well as ringdown suppression. The Hamiltonian used for optimization, in a frame rotating at the nominal electron Larmor frequency, was

$$H(\Delta\omega, \omega_1) = \frac{1}{2}\Delta\omega\sigma_z + \frac{1}{2}\omega_1 A(t)\sigma_x, \tag{8.11}$$

where $\Delta\omega$ is a resonance offset parameter representing static field inhomogeneity in units of rad/s, ω_1 is a scaling factor of the nominal Rabi frequency, $\omega_{1,\mathrm{nom}}$, representing microwave field inhomogeneity, and $A(t)$ is the time-dependent amplitude modulation representing the OCT pulse, with range $\{-\omega_{1,\mathrm{nom}}, \omega_{1,\mathrm{nom}}\}$. The spin dynamics was calculated by taking a convex operator sum over a uniform classical probability distribution of field inhomogeneities, $P(\Delta\omega, \omega_1)$ [24].

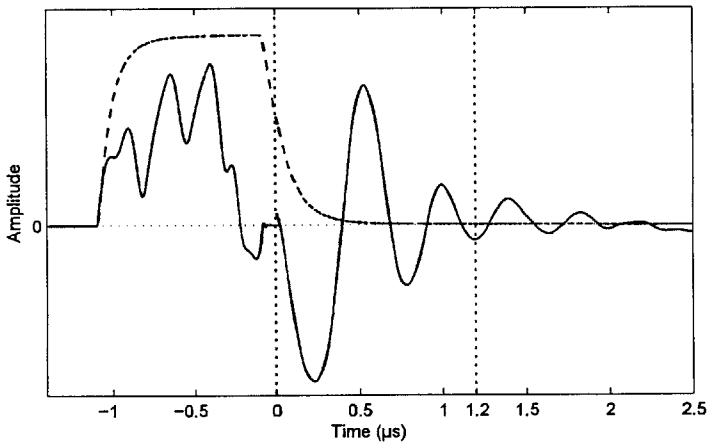

Figure 8-4: Digitized pulse and free-induction decay (FID) of irradiated quartz. The transients optimized OCT pulse shown in the previous figure was applied to an inhomogeneously broadened solid-state sample of irradiated fused-quartz in a rectangular cavity with Q = 8,486 at a resonance frequency of 9.5236 GHz. The black solid line for $t < 0$ shows the pulse profile digitized through a pick-up coil inserted in the cavity. The digitized profile closely matches the calculated profile with the only ringdown being a small oscillation which decays after roughly 75 ns. The resulting quartz FID is shown as a blue solid line for $t > 0$ and was acquired after a 75 ns spectrometer deadtime. The static field was moved roughly 2 MHz off-resonance (still within the high-fidelity operation regime of the pulse, as shown in Figure 8-3) to emphasize the shape of the FID. For comparison, a digitized square pulse of length 1 μs is shown as the black dashed line. In a separate measurement, the necessary spectrometer deadtime in the absence of ringdown suppression was determined to be 1.2 μs (shown as a dotted vertical line), which would prevent the detection of a significant portion of the FID. The separate plots have been scaled for visual clarity.

The pulse was defined piecewise constant over 100 steps of 10 ns each, giving a total length of 1 μs. The nominal Rabi frequency, $\omega_{1,\mathrm{nom}}/2\pi = 5.26$ MHz, was determined by Fourier transforming the result of a standard spin-echo Rabi oscillation experiment at a microwave power of 4 Watts and identifying the dominant frequency. The pulse was optimized over a microwave inhomogeneity of $\omega_1 = (0.95, 1, 1.05)$ and a static field inhomogeneity of $\Delta\omega/2\pi = \{$-2 MHz, 2 MHz$\}$ in steps of 250 kHz. The pulse optimization took roughly ten minutes on a standard laptop computer and resulted in an average fidelity over the distribution of $\Phi = 0.9905$. The resulting pulse profile and response over an extended distribution is shown in Figure 8-3. The free-induction decay (FID) of irradiated fused-quartz resulting from application of the pulse in the Varian cavity is shown in Figure 8-4, along with the digitized pulse profile measured through the pick-up coil. A spectrometer deadtime of 75 ns was required to allow the small oscillations shown at the end of the digitized pulse to decay. This deadtime was included in the pulse optimization as an additional control period of zero amplitude, allowing observation of the full FID at high Q and verifying the simulated behavior of the bandwidth-limited OCT pulse [1].

8.4 Controllability With Limited Bandwidth

For accurate spectroscopy and high-fidelity quantum information processing, control sequences must drive transitions and excite coherence over a range of frequencies given by the coupling structure and any uncertainties of the system Hamiltonian. A common solution, based on linear response theory [116], is to require the Fourier spectrum of the control pulse to contain significant contributions from all frequencies

[1] Upon initially implementing the optimized pulse we could not observe an FID due to spurious ringdown from a source which did not appear in the waveform digitized through the pick-up coil. The source of this ringdown was determined to be on-resonant leakage of the carrier signal through a double-balanced mixer used to mix in the ideal pulse waveform from an Arbitrary Waveform Generator (AWG). Leakage of this type has been noted previously [202] and was compensated using a similar method. Before the mixer we split off the carrier signal, phase-shifted it 180 degrees, then recombined it with the amplifier output through a directional coupler, appropriately adjusting the amplitude to cancel the amplified leakage signal. This method of active feedback suppression is also similar to the technique used by Broekaert and Jeener to compensate for radiation damping effects [29].

present in the quantum system [154, 90]. The principle, and limitations, of this approximate solution may be succinctly demonstrated using a description of the pulse trajectories in k-space [190]. In this description, each frequency ω present in the drift Hamiltonian of the quantum system has an associated wavenumber, $k = \omega t$, whose value is modulated by the control Hamiltonian during the length of the applied pulse.

The accuracy of predicting spin response through Fourier analysis depends primarily on the validity of two approximations. The first is that any rotations that occur during a period where the pulse waveform is constant are small, such that the full spin response given by the exponential of the Hamiltonian generating the motion may be truncated to first order. The second is that the amplitude of the control Hamiltonian during any pulse period be significantly greater than the amplitude of the drift Hamiltonian, such that the axis of rotation may be taken as being completely determined by the control Hamiltonian. When these two criteria are satisfied, excitations of the quantum system as a function of frequency may be written simply as the Fourier transform of the time-dependent control amplitudes, $x(t)$:

$$S(\omega) = -i \int_0^{t_p} x(t) e^{-ik} \, \mathrm{d}t, \tag{8.12}$$

where t_p is the pulse length and $S(\omega)$ is the observable spin response generated by the controls, which are taken for simplicity to be amplitude modulated only. If we now write the controls as a sum of Fourier components,

$$x(t) = \sum_{n=-\infty}^{\infty} x_n e^{i\omega_n^p t}, \tag{8.13}$$

we see that the only contributions to the observable signal are from Fourier components, n, where $x_n \neq 0$, such that the corresponding vector in k-space may be effectively refocused during the pulse. Within the linear response approximation, then, pulse design is frustrated by the narrow-band filtering property of a high-Q resonator. However, the ability to numerically optimize pulses allows us to move into a regime where linear response is no longer valid.

For general rotations there is significant mixing of the various k-vectors that leads to a complex spin response. Also, a general axis of rotation is not given entirely by the control Hamiltonian, but by the vector sum of the control and drift Hamiltonians. These effects are often small, but may be used to generate spin response deemed inaccessible by linear response. By solving the equations of motion exactly under an accurate system model, without making approximations, we can find bandwidth-limited pulses that retain the same degree of controllability as for infinite bandwidth pulses, albeit with a reduction in efficiency due to the inability to directly address all transitions in the system.

We first consider an ensemble of uncoupled spins with Larmor frequency, ω_0, off-resonance an amount $\Delta\omega = \omega_0 - \omega_t$ from a control field applied at ω_t. The Hamiltonian in a frame rotating at ω_t is given by eq. (8.11), where the term proportional to σ_z is the drift Hamiltonian, H_d, and the term proportional to σ_x is the control Hamiltonian, H_c. Generating a computationally universal set of quantum operations requires the ability to generate all elements of the Lie algebra spanning the Hilbert space [46]. For uncoupled spins, the Lie algebra is SU(2), with basis operators $\{I, \sigma_x, \sigma_y, \sigma_z\}$. The control algebra generated by a given set of Hamiltonians may be computed by taking successive Lie brackets to all orders [167, 177]. For H_d and H_c considered here $[H_d, H_c] \propto \sigma_y$, such that the generated control algebra is identical to SU(2), indicating universal control of the system by appropriate application of the given Hamiltonians.

The efficiency of control is difficult to quantify in general, but may be posed as the non-commutativity of effective Hamiltonians that may be generated during the pulse between incremental time periods. For SU(2) we may take a simple geometric view, posing the problem of efficiency as the maximum angle of rotation that may be generated over an incremental time period or, equivalently, the maximum angle between effective Hamiltonian vectors that may be generated from one instant in time to the next. Assuming an exponential model of the pulse transients for simplicity, and taking $A(t_0) = 0$ and $\omega_1 = 1$, we examine the non-commutativity of

$$H_{\text{eff}}(t_0) = \frac{1}{2}\Delta\omega\sigma_z, \tag{8.14}$$

and

$$H_{\text{eff}}(t_0+\delta t) = \frac{1}{2}\Delta\omega\sigma_z + \frac{1}{2}A(t_0+\delta t)(1-e^{-\frac{\omega_0}{Q}\delta t})\sigma_x. \tag{8.15}$$

The controllability of the system has not changed, provided Q is finite, as these Hamiltonians generate the same Lie algebra as for infinite bandwidth. The angle between the two Hamiltonian vectors, θ, is given by

$$\theta = \tan^{-1}\left[\frac{A(t_0+\delta t)}{\Delta\omega}(1-e^{-\frac{\omega_0}{Q}\delta t})\right]. \tag{8.16}$$

The size of the generated incremental rotation depends on the ratio of the target control amplitude to the resonance offset and the value of Q, with increasing efficiency for larger control amplitudes and smaller Q. Given that control amplitude is proportional to $\sqrt{Q}$, there is an inherent trade-off between sensitivity and the efficiency of generating rotations that must be considered. However, given sufficient time and a sufficiently accurate system model, pulses may be optimized that address transitions that are arbitrarily far off-resonance without containing Fourier components anywhere near the transition frequency. In the following section we provide examples, in the context of anisotropic hyperfine coupled electron-nuclear spin systems, of pulses that significantly exceed the limitations imposed by linear response theory.

8.5 Application of Bandwidth-Limited Control to Electron-Nuclear Spin Systems

To demonstrate that universal control via electron-only modulation may still be achieved when using a high-Q resonator we numerically optimized a pulse which implements an electron spin flip,

$$U_d = e^{-i\frac{\pi}{2}\sigma_x^e\otimes I^n}, \tag{8.17}$$

for a 1e-1n sample in a resonator with bandwidth smaller than the size of the hyperfine interaction. The ability to achieve such an operation implies full controllability of the

spin system with electron-only modulation (see Section 3.2). The control Hamiltonian was taken to be a time-dependent amplitude modulation of the electron spin only,

$$H_c(t) = \frac{1}{2}A(t)\sigma_x^e \otimes I^n. \tag{8.18}$$

The pulse was optimized using the algorithm outlined in Section 8.2 using a model of the resonator given in Section 8.1 with a Q of 10,000 (BW $\approx$ 1.2 MHz). The drift Hamiltonian parameters were taken from [86] and are defined in Section 3.2: $\omega_z^e/2\pi = 11.885$ GHz, $\omega_z^n/2\pi = 18.1$ MHz, $\omega_{zz}/2\pi = -42.7$ MHz, and $\omega_{zx}/2\pi = 14.2$ MHz. The carrier frequency of the pulses was set resonant with the 1-4 transition, $\omega_0/2\pi = 11.909$ GHz. The nominal Rabi frequency was taken to be $\omega_{\text{nom}}/2\pi = 100$ MHz. The resulting pulse is shown in Figure 8-5. A pulse time of 5 μs was chosen for convenience to provide sufficient time to easily achieve the desired operation. We expect solutions for shorter pulse times to exist, but have not systematically addressed the minimum time needed to achieve the operation for a given set of parameters. The final simulated average gate fidelity of the pulse was 0.9901 even when, as shown in Figure 8-5, all significant frequency modulation is much less than the hyperfine splitting.

8.6 Discussion

Integrating the impulse response function of a high-Q resonator into an optimal control theory pulse design algorithm allows higher sensitivity and signal-to-noise ratio in measurements without sacrificing the ability to perform a universal set of quantum operations with high fidelity. The limits imposed by linear response theory may be vastly exceeded when using numerically optimized pulses, allowing universal control of an electron-nuclear spin system even when the hyperfine coupling strength is significantly greater than the resonator bandwidth. These solutions rely on the non-commutativity of the effective Hamiltonians generated throughout the pulse and the ability to accurately engineer the exact response of a quantum system to complex

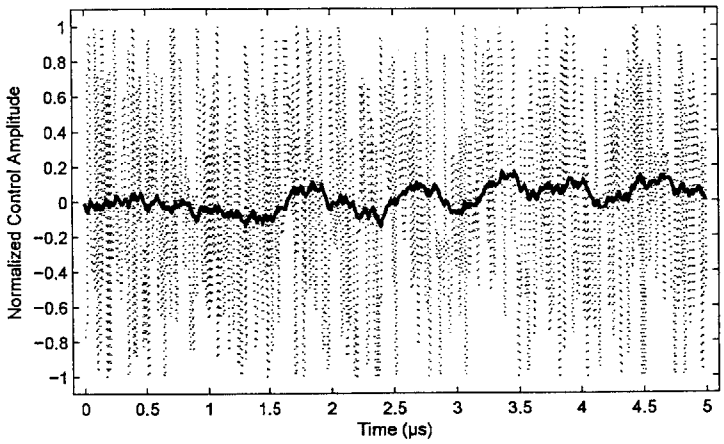

(a) Pulse Profile

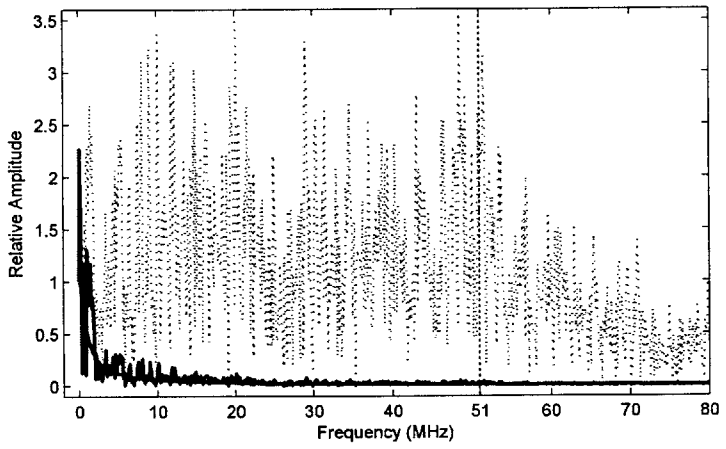

(b) Pulse Fourier Spectrum

Figure 8-5: (a) The undistorted (dashed line) and distorted (solid line) control amplitudes of a pulse designed to perform a π rotation of the electron spin in a resonator with Q = 10,000. Access to such an operation guarantees universal control of the nuclear spin via electron-only modulation [86]. The pulse consists of 500 time steps of Δt= 10 ns each for a total length of 5 μs, with $\omega_{1,\mathrm{nom}}/2\pi$ = 100 MHz. The simulated average gate fidelity is Φ = 0.9901. (b) The single-sided amplitude spectrum of the undistorted pulse (dotted line) and the distorted pulse (solid line) filtered by the resonator admittance function (bold solid line). The transitions necessary to achieve the desired operation were separated by an amount ($|\omega_{23} - \omega_{14}|$ = 51 MHz) much greater than the bandwidth of the resonator ($\approx$ 1.2 MHz), demonstrating that linear response may be greatly exceeded by pulses of high complexity optimized under a sufficiently accurate system model.

modulations.

The methods described in this chapter should find application in a broad range of fields. For example, advances in inductive imaging techniques have allowed for sub-micron resolution, pushing the limits of sensitivity using conventional resonators [205, 183, 196]. These techniques may also find application in hybrid quantum systems that aim to use spin ensembles as memory elements for microwave photons [219, 117].

Chapter 9

Conclusions and Outlook

We have demonstrated a number of techniques for control in open quantum systems, with emphasis on decoupling an environment to robustly store a qubit, developing control for spin-actuator multinode quantum information processing, obtaining high-fidelity control with limited resonator bandwidth, and formalizing notions of gate design. The technique for efficient information transfer between nodes put forth in Chapter 4 permits a universal set of gates to be performed across neighboring nodes with limited sensitivity to actuator decoherence. A particularly powerful operation enabled by this new protocol is the swapping of the complete nuclear spin processor states between nodes in parallel. In Chapter 5 we discussed the practical design of robust quantum gates and demonstrated that requiring control pulses to strongly modulate the environment leads to quantum gates that are robust to small unknown variations in the environment. Strong modulation also imposes composability of gates, ensuring any gate-dependent errors do not accumulate over the course of a computation.

The dynamical noise suppression techniques presented in Chapters 6 and 7 apply broadly to protecting the coherence of an arbitrary qubit. We demonstrated how optimal control theory can be used to optimize refocusing pulses for the CPMG sequence insensitive to variations in the applied control field and quanttizing field amplitudes. The enhanced robustness of the sequence expands its range of application in realistic control scenarios, and was shown to perform as expected in experiments.

We also introduced the concept of representing pulse errors in decoupling sequences – such as the CPMG and XY sequences – as a Pauli channel. This compact description enables the use of concepts from quantum information theory, such as noise twirling and logical subspace encodings, to enhance the functionality of the sequences by allowing them to simultaneously decouple an environment while treating all input states symmetrically.

Our novel method for high-fidelity control and ringdown suppression in high-Q resonators, developed and experimentally verified in Chapter 8, specifically enables a new design for a moderate-scale multinode quantum information processor based on solid-state electron-nuclear spin systems. The ability to accurately control a spin system with limited resonator bandwidth allows the use of high-Q superconducting resonators optimized for planar samples [16, 138], providing both a method for inductive readout of a small number of spins and the possibility of efficient entropy removal, without sacrificing the ability to implement a universal set of high-fidelity quantum gates. The small bandwidth of a high-Q resonator allows sideband cooling techniques to be used to quickly reset the electronic spins to a pure state [157, 209], a process important for performing efficient error correction. As the resonator directly couples to every actuator spin in the processor, entropy may be removed in parallel from all regions of the processor at once, a unique advantage to quantum information processing with spins coupled to high-Q cavities.

A spin-based platform for multinode quantum information processing may be obtained by making organic molecules with a localized free-radical electron spin into single-crystal molecular monolayers – using either a Langmuir-Blodgett process [151], or by self-assembly [139, 73]. Each node consists of a single molecule composed of an electron spin coupled via an anisotropic hyperfine interaction to a small number of nuclear spins. A particular advantage of having a purely two-dimensional array of identical processing nodes is the natural mapping to high-threshold planar quantum error correction codes (see Section 1.2). For qubit measurement, the resonator quality factors currently achieved, $\mathcal{O}(10^3)$, limit inductive sensitivity to roughly 10^6 electron spins, requiring initial designs to be composed of an ensemble of identical

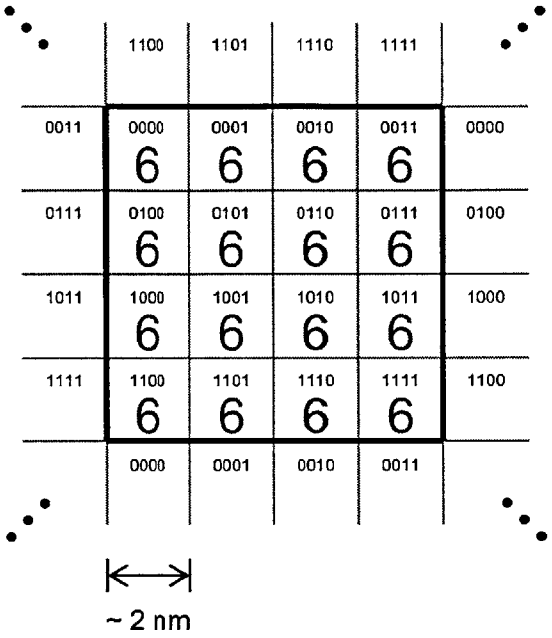

Figure 9-1: Schematic diagram of possible processor layout and addressing scheme. Each small blue square region denotes a node of the processor, containing a single molecule with a single electron spin coupled to ten nuclear spins – a candidate molecule is perchlorotriphenylmethyl (PTM) [7]. The black square regions denote a plaquette that is identically repeated about 10^6 times to allow inductive ensemble measurements. Four of the nuclear spins are used as classical bits to spatially label the nodes within each plaquette. The remaining six nuclear spins may be used as coherent processing qubits, leading to a total of 96 qubits in the processor.

plaquettes, each containing around 20 nodes (Figure 9-1). Quantum error correction may still be performed using ensemble measurements and coherent correction gates, but access to projective measurement of single nodes may be necessary to increase the efficiency and potential scalability of future designs. Possible projective measurement schemes include optical detection using Nitrogen-vacancy defect centers in diamond nanopillars [74, 137], electrical detection [153] or mechanical detection [172].

Access to a robust spin-based multinode quantum information processor containing around 100 qubits would provide a valuable tool for concretely testing and benchmarking quantum control and error correction in a setting unavailable to classical

simulation, easing the development of future large-scale devices. Potential challenges for engineering the described device include integrating superconducting electronics and pulsed gradient coils with low-temperature molecular monolayer spin samples, further investigation of control efficiencies in the presence of bandwidth limitations, identification and evaluation of various free-radical samples, and development of quantum error correction protocols specifically optimized for actuator-based nodes with multiple qubits.

Appendix A

Derivation of Gradients for Reactive Controls

In this appendix we derive in detail the gradients used to optimize pulses with optimal control theory in the presence of resonator distortions of the ideal waveform. We begin with a set of undistorted controls, $\{u^j\}$, where $j = 1, ..., N$ and resample to obtain a set of undistorted controls $\{\widetilde{u}^m\}$, where $m = 1, ..., M$ and $M = n_s N + n_r$ for n_s samples per N control periods and n_r values of zero appended to the waveform to account for pulse ringdown. For clarity, we assume only one control Hamiltonian ($k = 1$). The distorted controls, $\{\widetilde{v}^m\}$, are then given by the discrete convolution of the undistorted controls with the resonator impulse response function:

$$\widetilde{v}^m = \sum_{l \leq m} h^{m-l+1} \widetilde{u}^l. \tag{A.1}$$

The average gate fidelity may then be written as

$$\Phi = \left\langle U_d | \widetilde{U}_M ... \widetilde{U}_1 \right\rangle \left\langle \widetilde{U}_1 ... \widetilde{U}_M | U_d \right\rangle, \tag{A.2}$$

where the m^{th} propagator is calculated from the distorted controls as

$$\begin{aligned}\widetilde{U}_m =& e^{-i\frac{\Delta t}{n_s}(H_d+\tilde{v}^m H_1)} \\ =& e^{-i\frac{\Delta t}{N_s}(H_d+\sum_{l\leq m} h^{m-l+1}\tilde{u}^m H_1)}.\end{aligned} \tag{A.3}$$

We are interested in calculating the gradient of the fidelity with respect to a perturbation of the undistorted controls $\{u^j\}$, given by the usual product and chain rules of derivation as

$$\begin{aligned}\frac{\delta\Phi}{\delta u^j} =& \sum_{m=1}^{M} \left\langle U_d|\widetilde{U}_M...\frac{\delta\widetilde{U}_m}{\delta u^j}...\widetilde{U}_1\right\rangle \left\langle \widetilde{U}_1...\widetilde{U}_M|U_d\right\rangle + \\ & \left\langle U_d|\widetilde{U}_M...\widetilde{U}_1\right\rangle \left\langle \widetilde{U}_1...\frac{\delta\widetilde{U}_m}{\delta u^j}...\widetilde{U}_M|U_d\right\rangle.\end{aligned} \tag{A.4}$$

By defining a forward propagator, $\widetilde{X}_m = \widetilde{U}_m...\widetilde{U}_1$, a backward propagator, $\widetilde{P}_m = \widetilde{U}^\dagger_{m+1}...\widetilde{U}^\dagger_M U_d$, and noting that only propagators with $m > (j-1)n_s$ will be modified by a change in the j^{th} control period, we may simplify this expression to

$$\begin{aligned}\frac{\delta\Phi}{\delta u^j} =& \sum_{m>(j-1)n_s}^{M} \langle P_m|X_m\rangle \left\langle \frac{\delta\widetilde{U}_m}{\delta u^j}X_{m-1}|P_m\right\rangle + \\ & \left\langle P_m|\frac{\delta\widetilde{U}_m}{\delta u^j}X_{m-1}\right\rangle \langle X_m|P_m\rangle.\end{aligned} \tag{A.5}$$

Due to resampling the control period, we define a top-hat function, $\Xi(j,n_s)$, to account for the perturbation being constant during the entire j^{th} control period:

$$\Xi(j,n_s) = 1 \text{ for } (j-1)n_s < m \leq jn_s + 1, \tag{A.6}$$

$$\Xi(j,n_s) = 0 \text{ otherwise.} \tag{A.7}$$

The derivative $\delta\widetilde{U}_m/\delta u^j$ may then be calculated by definition as

$$\frac{\delta\widetilde{U}_m}{\delta u^j} = \lim_{\delta u^j\to 0} \frac{\widetilde{U}_m(\tilde{v}^m + \Xi(j,n_s)\delta u^j) - \widetilde{U}_m(\tilde{v}^m)}{\delta u^j}. \tag{A.8}$$

We apply a small perturbation to the j^{th} control, $u^j \to u^j + \delta u^j$ and determine the resulting m^{th} propagator:

$$\begin{aligned} &\widetilde{U}_m(\widetilde{v}^m + \Xi(j, n_s)\delta u^j) = \\ &e^{-i\frac{\Delta t}{n_s}\left[H_d + (\widetilde{v}^m + \sum_{l\leq m} h^{m-l+1}\Xi(j,n_s)\delta u^j)H_1\right]}. \end{aligned} \tag{A.9}$$

Assuming Δt to be small, we may approximate H_d and H_1 as commuting, allowing us to keep only the first order term of a BCH expansion of the perturbed propagator

$$\begin{aligned} &\widetilde{U}_m(\widetilde{v}^m + \Xi(j, n_s)u^j) = \\ &\widetilde{U}_m(\widetilde{v}^m)e^{-i\frac{\Delta t}{n_s}\sum_{l\leq m} h^{m-l+1}\Xi(j,n_s)\delta u^j H_1}. \end{aligned} \tag{A.10}$$

If we now assume the perturbation δu^j to also be small, we may make a first order series approximation of the exponential, to give

$$\begin{aligned} &\widetilde{U}_m(\widetilde{v}^m + \Xi(j, n_s)u^j) = \\ &\widetilde{U}_m(\widetilde{v}^m)(I - i\frac{\Delta t}{n_s}H_1\widetilde{U}_m \sum_{l\leq m} h^{m-l+1}\Xi(j, n_s)\delta u^j + \mathcal{O}(\Delta t^2). \end{aligned} \tag{A.11}$$

We may now plug this expression back into (A.8) to obtain

$$\frac{\delta\widetilde{U}_m}{\delta u^j} = -i\frac{\Delta t}{n_s}H_1\widetilde{U}_m \sum_{l\leq m} h^{m-l+1}\Xi(j, n_s), \tag{A.12}$$

which, when plugged into (A.5) gives

$$\frac{\delta\Phi}{\delta u^j} = \sum_{m>(j-1)n_s}^{M} \xi^m(j)\frac{\delta\Phi}{\delta\widetilde{v}^m}, \tag{A.13}$$

where $\xi^m(j)$ is the convolution of the top-hat function with the resonator impulse response function:

$$\xi^m(j) = \sum_{l\leq m} h^{m-l+1}\Xi(j, n_s). \tag{A.14}$$

This function may be interpreted as a weighting of the change of the fidelity due to a small change $\delta\widetilde{v}^m$ of the pulse parameter at the m^{th} evolution time step induced by the perturbation δu^j:

$$\frac{\delta\Phi}{\delta\widetilde{v}^m} = -2\text{Re}\left[\left\langle P_m|i\frac{\Delta t}{n_s}H_1X_m\right\rangle\langle X_m|P_m\rangle\right]. \tag{A.15}$$

Note that when the controls are undistorted, the gradient weighting function is equivalent to the top-hat function, giving

$$\frac{\delta\Phi}{\delta u^j} = \sum_{m\geq(j-1)n_s+1}^{jn_s}\frac{\delta\Phi}{\delta\widetilde{u}^m}, \tag{A.16}$$

which for short time steps and small perturbations, reduces to the undistorted gradient derived in [105]:

$$\frac{\delta\Phi}{\delta u^j} = -2\text{Re}\left[\langle P_j|i\Delta tH_1X_j\rangle\langle X_j|P_j\rangle\right]. \tag{A.17}$$

In the special case where two control Hamiltonians, H_1 and H_2, are in quadrature with one another - for example, amplitude and phase modulation of a single control field in magnetic resonance - the gradients must be modified to reflect the interdependence of the Hamiltonians. The resonator impulse response function, h, and the control signals, u and v, must be considered as complex functions, with the real part associated with H_1 and the imaginary part associated with H_2. The gradients for the real and imaginary parts of the controls are then:

$$\frac{\delta\Phi}{\delta\text{Re}[u^j]} = \sum_{m>(j-1)n_s}^{M}\text{Re}[\xi^m(j)]\frac{\delta\Phi}{\delta\text{Re}[\widetilde{v}^m]} + \text{Im}[\xi^m(j)]\frac{\delta\Phi}{\delta\text{Im}[\widetilde{v}^m]}, \tag{A.18}$$

$$\frac{\delta\Phi}{\delta\text{Im}[u^j]} = \sum_{m>(j-1)n_s}^{M}\text{Re}[\xi^m(j)]\frac{\delta\Phi}{\delta\text{Im}[\widetilde{v}^m]} - \text{Im}[\xi^m(j)]\frac{\delta\Phi}{\delta\text{Re}[\widetilde{v}^m]}, \tag{A.19}$$

where

$$\frac{\delta\Phi}{\delta\text{Re}[\widetilde{v}^m]} = -2\text{Re}\left[\left\langle P_m|i\frac{\Delta t}{n_s}H_1X_m\right\rangle\langle X_m|P_m\rangle\right], \tag{A.20}$$

$$\frac{\delta\Phi}{\delta \mathrm{Im}[\widetilde{v}^m]} = -2\mathrm{Re}\left[\left\langle P_m | i\frac{\Delta t}{n_s} H_2 X_m \right\rangle \langle X_m | P_m \rangle\right]. \tag{A.21}$$

Bibliography

[1] A. Abragam. *The Principles of Nuclear Magnetism.* Oxford University Press, 1961.

[2] A. Abragam and B. Bleaney. *Electron Paramagnetic Resonance of Transition Ions.* Oxford University Press, 1970.

[3] A. Ajoy and P. Cappellaro. Mixed-state quantum transport in correlated spin networks. *Phys. Rev. A*, 85:042305, 2012.

[4] P. Aliferis, D. Gottesman, and J. Preskill. Quantum accuracy threshold for concatenated distance-3 code. *Q. Info. Comp.*, 6:97–165, 2006.

[5] N.M. Atherton. *Principles of Electron Spin Resonance.* Ellis Horwood, 1993.

[6] F. Balibanu, K. Hailu, R. Eymael, D.E. Demco, and B. Blumich. Nuclear magnetic resonance in inhomogeneous magnetic fields. *J. Magn. Reson.*, 145:246–258, 2000.

[7] M. Ballester. Inert free radicals (ifr): A unique trivalent carbon species. *Acc. Chem. Res.*, 18:380, 1985.

[8] T.M. Barbara, J.F. Martin, and J.G. Wurl. Phase transients in nmr probe circuits. *J. Magn. Reson.*, 93:497–508, 1991.

[9] J. Baugh, J. Chamilliard, C. M. Chandrasekhar, M. Ditty, A. Hubbard, R. Laflamme, M. Laforest, D. Maslov, O. Moussa, C. Negrevergne, M. Silva, S. Simmons, C.A. Ryan, D.G. Cory, J.S. Hodges, and C. Ramanathan. Quantum information processing using nuclear and electron magnetic resonance: Review and prospects. *arXiv:0710.1447v1*, 2007.

[10] J. Baugh, O. Moussa, C.A. Ryan, R. Laflamme, C. Ramanathan, T.F. Havel, and D.G. Cory. Solid-state nmr three-qubit homonuclear system for quantum-information processing: Control and characterization. *Phys. Rev. A*, 73:022305, 2006.

[11] J. Baugh, O. Moussa, C.A. Ryan, R. Laflamme, C. Ramanathan, T.F. Havel, and D.G. Cory. Solid-state nmr three-qubit homonuclear system for quantum-information processing: Control and characterization. *Phys. Rev. A*, 73:022305, 2006.

[12] J. Baum, R. Tycko, and A. Pines. Broadband and adiabatic inversion of a two-level system by phase-modulated pulses. *Phys. Rev. A*, 32:3435–3447, 1985.

[13] P. Benioff. The computer as a physical system: A microscopic quantum mechanical hamiltonian model of computers as represented by turing machines. *J. Stat. Phys.*, 22:563–591, 1980.

[14] P. Benioff. Quantum mechanical hamiltonian models of turing machines. *J. Stat. Phys.*, 29:515–546, 1982.

[15] P. Benioff. Quantum mechanical models of turing machines that dissipate no energy. *Phys. Rev. Lett.*, 48:1581–1585, 1982.

[16] O.W.B. Benningshof, H.R. Mohebbi, I.A.J. Taminiau, G.X. Miao, and D.G. Cory. Superconducting microstrip resonator for pulsed esr of thin films. *in preparation*, 2012.

[17] A. Bermudez, F. Jelezko, M.B. Plenio, and A. Retzker. Electron-mediated nuclear-spin interactions between distant nitrogen-vacancy centers. *Phys. Rev. Lett.*, 107:150503, 2011.

[18] M.J. Biercuk, H. Uys, A.P. VanDevender, N. Shiga, W.M. Itano, and J.J. Bollinger. Optimized dynamical decoupling in a model quantum memory. *Nature*, 458:996–1000, 2009.

[19] K. Binder, editor. *The Monte Carlo Method in Condensed Matter Physics.* Springer-Verlag, New York, 1995.

[20] N. Bloembergen, E.M. Purcell, and R.V. Pound. Relaxation effects in nuclear magnetic resonance absorption. *Phys. Rev.*, 73:679–712, 1948.

[21] J.-M. Bohlen and G. Bodenhausen. Experimental aspects of chirp nmr spectroscopy. *J. Magn. Reson. A*, 102:293–301, 1993.

[22] J.-M. Bohlen, M. Rey, and G. Bodenhausen. Refocusing with chirped pulses for broadband excitation without phase dispersion. *J. Magn. Reson.*, 84:191–197, 1989.

[23] T.W. Borneman, C.E. Granade, and D.G. Cory. Parallel information transfer in a multinode quantum information processor. *Phys. Rev. Lett.*, 108:140502, 2012.

[24] T.W. Borneman, M.D. Hurlimann, and D.G. Cory. Application of optimal control to cpmg refocusing pulse design. *J. Magn. Reson.*, 207:220–233, 2010.

[25] N. Boulant, J. Emerson, T.F. Havel, D.G. Cory, and S. Furuta. Incoherent noise and quantum information processing. *J. Chem. Phys.*, 121(7):2955–2961, 2004.

[26] S. Bravyi and A. Kitaev. Universal quantum computation with ideal clifford gates and noisy ancillas. *Phys. Rev. A*, 71:022316, 2004.

[27] H.-P. Breuer and F. Petruccione. *The Theory of Open Quantum Systems.* Oxford University Press, 2002.

[28] H.-J. Briegel, W. Dur, J.I. Cirac, and P. Zoller. Quantum repeaters: The role of imperfect local operations in quantum communication. *Phys. Rev. Lett.*, 81:5932–5935, 1998.

[29] P. Broekaert and J. Jeener. Suppression of radiation damping in nmr in liquids by active electronic feedback. *J. Magn. Reson.*, A113:60, 1995.

[30] J. Bylander, S. Gustavsson, F. Yan, F. Yoshihara, K. Harrabi, G. Fitch, D.G. Cory, Y. Nakamura, J.-S. Tsai, and W.D. Oliver. Noise spectroscopy through dynamical decoupling with a superconducting flux qubit. *Nature Phys.*, 7:565–570, 2011.

[31] P. Cappellaro, J.S. Hodges, T.F. Havel, and D.G. Cory. Principles of control for decoherence-free subsystems. *J. Chem. Phys.*, 125:044514, 2006.

[32] P. Cappellaro, J.S. Hodges, T.F. Havel, and D.G. Cory. Subsystem pseudopure states. *Phys. Rev. A*, 75:042321, 2007.

[33] P. Cappellaro, L. Jiang, J.S. Hodges, and M.D. Lukin. Coherence and control of quantum registers based on electronic spin in a nuclear spin bath. *Phys. Rev. Lett.*, 102:210502, 2009.

[34] H.Y. Carr and E.M. Purcell. Effects of diffusion on free precession in nuclear magnetic resonance experiments. *Phys. Rev.*, 94:630–638, 1954.

[35] R. Chakrabarti and H. Rabitz. Quantum control landscapes. *Int. Rev. Phys. Chem.*, 26:671–735, 2007.

[36] H. Cho, P. Cappellaro, D.G. Cory, and C. Ramanathan. Decay of highly correlated spin states in a dipolar-coupled solid: Nmr study of caf2. *Phys. Rev. B*, 74:224434, 2006.

[37] M.-D. Choi. Completely positive linear maps on complex matrices. *Linear Alg. Appl.*, 10:285–290, 1975.

[38] I.L. Chuang, R. Laflamme, P.W. Shor, and W.H. Zurek. Quantum computers, factoring, and decoherence. *Science*, 270:1633–1635, 1995.

[39] J.I. Cirac and P. Zoller. Quantum computations with cold trapped ions. *Phys. Rev. Lett.*, 74:4091–4094, 1995.

[40] S. Connolly, D. Nishimura, and A. Macovski. Optimal control solutions to the magnetic resonance selective excitation problem. *IEEE Trans. Med. Imaging*, MI-5:106–115, 1986.

[41] D.G. Cory, A.F. Fahmy, and T.F. Havel. Ensemble quantum computing by nmr spectroscopy. *Proc. Natl. Acad. Sci. USA*, 94:1634–1639, 1997.

[42] D.G. Cory, R. Laflamme, E. Knill, L. Viola, T.F. Havel, N. Boulant, G. Boutis, E. Fortunato, S. Lloyd, R. Martinez, C. Negrevergne, M. Pravia, Y. Sharf, G. Teklemariam, Y.S. Weinstein, and W.H. Zurek. Nmr based quantum information processing: Achievements and prospects. *Fortschr. Phys.*, 48:875–907, 2000.

[43] D.G. Cory, M.D. Price, and T.F. Havel. Nuclear magnetic resonance spectroscopy: An experimentally accessible paradigm for quantum computing. *Physica D*, 120:82–101, 1998.

[44] B. Cowan. *Nuclear Magnetic Resonance and Relaxation.* Cambridge University Press, 1997.

[45] R. Crepeau, A. Dulic, J. Gorcester, T. Saarinen, and J. Freed. Composite pulses in time-domain ESR. *J. Magn. Reson.*, 84(1):184–190, August 1989.

[46] D. D'Alessandro. *Introduction to Quantum Control and Dynamics.* Chapman and Hall/CRC, 2007.

[47] R.A. de Graaf, Y. Luo, M. Terpstra, H. Merkle, and M. Garwood. A new localization method using an adiabatic pulse, bir-4. *J. Magn. Reson. B*, 106:245–252, 1995.

[48] E. Dennis, A. Kitaev, A. Landahl, and J. Preskill. Topological quantum memory. *J. Math. Phys.*, 43:4452, 2002.

[49] D. Deutsch. Quantum theory, the church-turing principle and the universal quantum computer. *Proc. R. Soc. Lond. A*, 400:97–117, 1985.

[50] D.P. DiVincenzo. Quantum computation. *Science*, 270:255–261, 1995.

[51] D.P. DiVincenzo. Two-bit gates are universal for quantum computation. *Phys. Rev. A*, 51:1015–1022, 1995.

[52] D.P. DiVincenzo. The physical implementation of quantum computation. *Fortschr. Phys.*, 48:771–783, 2000.

[53] L.-M. Duan and G.-C. Guo. Preserving coherence in quantum computation by pairing quantum bits. *Phys. Rev. Lett.*, 79:1953–1956, 1997.

[54] L.M. Duan and C. Monroe. Colloquium: Quantum networks with trapped ions. *Rev. Mod. Phys.*, 82:1209–1224, 2010.

[55] F.J. Dyson. The radiation theories of tomonaga, schwinger, and feynman. *Phys. Rev.*, 75:486–502, 1949.

[56] G.R. Eaton, S.S. Eaton, R.W. Quine, D. Mitchell, V. Kathirvelu, and R.T. Weber. A signal-to-noise standard for pulsed EPR. *J. Magn. Reson.*, 205(1):109–113, July 2010.

[57] S.S. Eaton and G.R. Eaton. Irradiated Fused-Quartz Standard Sample for Time-Domain EPR. *J. Magn. Reson.*, 102(3):354–356, May 1993.

[58] A.K. Ekert. Quantum cryptography based on bell's theorem. *Phys. Rev. Lett.*, 67:661–663, 1991.

[59] J. Emerson, M. Silva, O. Moussa, C. Ryan, M. Laforest, J. Baugh, D.G. Cory, and R. Laflamme. Symmetrized characterization of noisy quantum processes. *Science*, 317:1893–1896, 2007.

[60] R.P. Feynman. Simulating physics with computers. *Int. J. Theor. Phys.*, 21:467, 1982.

[61] E.M. Fortunato, M.A. Pravia, N. Boulant, G. Teklemariam, T.F. Havel, and D.G. Cory. Design of strongly modulating pulses to implement precise effective hamiltonians for quantum information processing. *J. Chem. Phys.*, 116:7599–7606, 2002.

[62] E.M. Fortunato, L. Viola, J. Hodges, G. Teklemariam, and D.G. Cory. Implementation of universal control on a decoherence-free qubit. *New J. Phys.*, 4:5.1–5.20, 2002.

[63] A.G. Fowler, A.M. Stephens, and P. Groszkowski. High-threshold universal quantum computation on the surface code. *Phys. Rev. A*, 80:052312, 2009.

[64] R. Freeman. Shaped radiofrequency pulses in high resolution nmr. *J. Prog. Nucl. Magn. Reson. Spect.*, 32:59–106, 1998.

[65] R. Fu and G. Bodenhausen. Broadband decoupling in nmr with frequency-modulated 'chirp' pulses. *Chem. Phys. Lett.*, 245:415–420, 1995.

[66] D. Gamliel and H. Levanon. *Stochastic Processes in Magnetic Resonance.* World Scientific, 1995.

[67] M. Garwood and L. DelaBarre. The return of the frequency sweep: Designing adiabatic pulses for contemporary nmr. *J. Magn. Reson.*, 153:155–177, 2001.

[68] H. Geen and R. Freeman. Band-selective radiofrequency pulses. *J. Magn. Reson.*, 93:93–141, 1991.

[69] N.A. Gershenfeld and I.L. Chuang. Bulk spin-resonance quantum computation. *Science*, 275:350–356, 1997.

[70] S.J. Glaser, T. Schulte-Herbruggen, M. Sieveking, O. Schedletzky, N.C. Nielsen, O.W. Sorensen, and C. Griesinger. Unitary control in quantum ensembles, maximizing signal intensity in coherent spectroscopy. *Science*, 280:421–424, 1998.

[71] G. Goelman and M.G. Prammer. The cpmg sequence in strong magnetic field gradients with applications to qil-well logging. *J. Magn. Reson. A*, 113:11–18, 1995.

[72] D. Gottesman. Stabilizer codes and quantum error correction. *arXiv:quant-ph/9705052*, 1997.

[73] F. Grillo, V. Mugnaini, M. Oliveros, S.M. Francis, D.-J. Choi, M.V. Rastei, L. Limot, C. Cepek, M. Pedio, S.T. Bromley, N.V. Richardson, J.-P. Bucher, and J. Veciana. Chiral conformation at a molecular level of a propeller-like open-shell molecule on au(111). *J. Phys. Chem. Lett.*, 3:1559, 1012.

[74] B. Grotz, J. Beck, P. Neumann, B. Naydenov, R. Reuter, F. Reinhard, F. Jelezko, J. Wrachtrup, D. Schweinfurth, B. Sarkar, and P. Hemmer. Sensing external spins with nitrogen-vacancy diamond. *New J. Phys.*, 13:055004 (2011), 2011.

[75] J.B. Grutzner and R.E. Santini. Coherent broad-band decoupling - an alternative to proton noise decoupling in carbon-13 nuclear magnetic resonance spectroscopy. *J. Magn. Reson.*, 19:173–187, 1975.

[76] T. Gullion, D.B. Baker, and M.S. Conradi. New, compensated carr-purcell sequences. *J. Magn. Reson.*, 89:479–484, 1990.

[77] U. Haeberlen and J.S. Waugh. Coherent averaging effects in magnetic resonance. *Phys. Rev.*, 175:453–467, 1968.

[78] E.L. Hahn. Spin echoes. *Phys. Rev.*, 80:580–594, 1950.

[79] L.D. Hall and T.J. Norwood. Zero-quantum-coherence, chemical-shift-resolved imaging in an inhomogeneous magnetic field. *J. Magn. Reson.*, 67:382–385, 1986.

[80] W. Harneit. Fullerene-based electron-spin quantum computer. *Phys. Rev. A*, 65:032322, 2002.

[81] T.F. Havel. Robust procedures for converting among lindblad, kraus and matrix representations of quantum dynamical semigroups. *J. Math. Phys.*, 44:534–557, 2003.

[82] A. Heidebrecht, J. Mende, and M. Mehring. Indirect detection of selective nuclear spin-spin interactions in a hostile environment. *Sol. State Nuc. Magn. Reson.*, 29:90–94, 2006.

[83] A. Heidebrecht, J. Mende, and M. Mehring. Quantum state engineering with spins. *Fortschr. Phys.*, 54:788–803, 2006.

[84] M.K. Henry, C. Ramanathan, J.S. Hodges, C.A. Ryan, M.J. Ditty, R. Laflamme, and D.G. Cory. Fidelity Enhancement by Logical Qubit Encoding. *Phys. Rev. Lett.*, 99(22):220501+, November 2007.

[85] J.S. Hodges. *Engineering Coherent Control of Quantum Information in Spin Systems.* PhD thesis, Massachusetts Institute of Technology, 2007.

[86] J.S. Hodges, J.C. Yang, C. Ramanathan, and D.G. Cory. Universal control of nuclear spins via anisotropic hyperfine interactions. *Phys. Rev. A*, 78:010303, 2008.

[87] E.C. Hoffman, M. Hubrich, and A. Schweiger. Primary Nuclear Spin Echoes in EPR Induced by Microwave Pulses. *J. Magn. Reson. A*, 117(1):16–27, November 1995.

[88] J.P. Hornak and J.H. Freed. Spectral rotation in pulsed ESR spectroscopy. *J. Magn. Reson.*, 67(3):501–518, May 1986.

[89] D.I. Hoult. Fast recovery, high sensitivity NMR probe and preamplifier for low frequencies. *Rev. Sci. Instr.*, 50(2):193–200, 1979.

[90] D.I. Hoult. The solution of the bloch equations in the presence of a varying b1 field–an approach to selective pulse analysis. *J. Magn. Reson.*, 35:69–86, 1979.

[91] M.D. Hurlimann. Carr-purcell sequences with composite pulses. *J. Magn. Reson.*, 152:109–123, 2001.

[92] M.D. Hurlimann and D.D. Griffin. Spin dynamics of carr-purcell-meiboom-gill-like sequences in grossly inhomogeneous bo and b1 fields and application to nmr well logging. *J. Magn. Reson.*, 143:120–135, 2000.

[93] T.-L. Hwang, P.C.M. van Zilj, and M. Garwood. Broadband adiabatic refocusing without phase distortion. *J. Magn. Reson.*, 124:250–254, 1997.

[94] D. Jaksch, J.I. Cirac, P. Zoller, S.L. Rolston, R. Cote, and M.D. Lukin. Fast quantum gates for neutral atoms. *Phys. Rev. Lett.*, 85:2208–2211, 2000.

[95] F. Jelezko and J. Wrachtrup. Single defect centres in diamond: A review. *Phys. Stat. Sol. A*, 203:3207–3225, 2006.

[96] L. Jiang, J.S. Hodges, J.R. Maze, P. Maurer, J.M. Taylor, D.G. Cory, P.R. Hemmer, R.L. Walsworth, A. Yacoby, A.S. Zibrov, and M.D. Lukin. Repetitive readout of a single electronic spin via quantum logic with nuclear spin ancillae. *Science*, 326:267–272, 2009.

[97] L. Jiang, J.M. Taylor, A.S. Sorensen, and M.D. Lukin. Scalable quantum networks based on few-qubit registers. *Phys. Rev. A*, 76:062323, 2007.

[98] J.A. Jones. Quantum computing with nmr. *J. Prog. Nuc. Magn. Reson. Spect.*, 59:91–120, 2011.

[99] J.A. Jones and E. Knill. Efficient refocusing of one-spin and two-spin interactions for nmr quantum computation. *J. Magn. Reson.*, 141:322–325, 1999.

[100] R. Jozsa. Quantum algorithms and the fourier transform. *Proc. R. Soc. Lond. A*, 454:323–337, 1998.

[101] R. Jozsa and N. Linden. On the role of entanglement in quantum-computational speed-up. *Proc. R. Soc. Lond. A*, 459:2011–2032, 2003.

[102] A. Bryson Jr. and Y.-C. Ho. *Applied Optimal Control.* Hemisphere, Washington, D.C., 1975.

[103] J.D. Ellett Jr. and J.S. Waugh. Chemical-shift concertina. *J. Chem. Phys.*, 51:2851–2858, 1969.

[104] B.E. Kane. A silicon-based nuclear spin quantum computer. *Nature*, 393:133–137, 1998.

[105] N. Khaneja, T. Reiss, C. Kehlet, T. Schulte-Herbruggen, and S.J. Glaser. Optimal control of coupled spin dynamics: design of nmr pulse sequences by gradient ascent algorithms. *J. Magn. Reson.*, 172:296–305, 2005.

[106] K. Khodjasteh and D.A. Lidar. Performance of deterministic dynamical decoupling schemes: Concatenated and periodic pulse sequences. *Phys. Rev. A*, 75:062310, 2007.

[107] K. Khodjasteh and L. Viola. Dynamical quantum error correction of unitary operations with bounded controls. *Phys. Rev. A*, 80:032314, 2009.

[108] D. Kielpinski, V. Meyer, M. A. Rowe, C. A. Sackett, W.M. Itano, C. Monroe, and D.J. Wineland. A decoherence-free quantum memory using trapped ions. *Science*, 291:1013–1015, 2001.

[109] D. Kielpinski, C. Monroe, and D.J. Wineland. Architecture for a large-scale ion-trap quantum computer. *Nature*, 417:709–711, 2002.

[110] A. Kitaev. Quantum computations: Algorithms and error correction. *Russian Mathematical Surveys*, 52:1191–1249, 1997.

[111] A.Y. Kitaev. Fault-tolerant quantum computation by anyons. *Ann. Phys.*, 303:2–30, 2003.

[112] E. Knill, R. Laflamme, and L. Viola. Theory of quantum error correction for general noise. *Phys. Rev. Lett.*, 84:2525–2528, 2000.

[113] K. Kobzar, B. Luy, N. Khaneja, and S.J. Glaser. Pattern pulses: design of arbitrary excitation profiles as a function of pulse amplitude and offset. *J. Magn. Reson.*, 173:229–235, 2005.

[114] K. Kobzar, T.E. Skinner, N. Khaneja, S.J. Glaser, and B. Luy. Exploring the limits of broadband excitation and inversion pulses. *J. Magn. Reson.*, 170:236–243, 2004.

[115] K. Kraus. General state changes in quantum theory. *Ann. Phys.*, 64:311–335, 1971.

[116] R. Kubo and K. Tomita. A General Theory of Magnetic Resonance Absorption. *J. Phys. Soc. Japan*, 9(6):888–919, June 1954.

[117] Y. Kubo, I. Diniz, C. Grezes, T. Umeda, J. Isoya, H. Sumiya, T. Yamamoto, H. Abe, S. Onoda, T. Ohshima, V. Jacques, A. Dreau, J.-F. Roch, A. Auffeves, D. Vion, D. Esteve, and P. Bertet. Electron spin resonance detected by a superconducting qubit. *arXiv:1205.5659v1*, 2012.

[118] E. Kupce and R. Freeman. Adiabatic pulses for wideband inversion and broadband decoupling. *J. Magn. Reson. A*, 115:273–276, 1995.

[119] P.G. Kwiat, A.J. Berglund, J.B. Altpeter, and A.G. White. Experimental verification of decoherence-free subspaces. *Science*, 290:498–501, 2000.

[120] T.D. Ladd, F. Jelezko, R. Laflamme, Y. Nakamura, C. Monroe, and J.L. O'Brien. Quantum computers. *Nature*, 464:45–53, 2010.

[121] R. Laflamme, D. Cory, C. Negrevergne, and L. Viola. Nmr quantum information processing and entanglement. *Q. Info. Comp.*, 2:166–176, 2002.

[122] R. Laflamme, C. Miquel, J.P. Paz, and W.H. Zurek. Perfect quantum error correcting code. *Phys. Rev. Lett.*, 77:198–201, 1996.

[123] R. Landauer. Is quantum mechanics useful? *Phil. Trans. R. Soc. Lond. A*, 353:367–376, 1995.

[124] M.H. Levitt. Composite pulses. *J. Prog. Nucl. Magn. Reson. Spect.*, 18:61–122, 1986.

[125] M.H. Levitt and R. Freeman. Composite pulse decoupling. *J. Magn. Reson.*, 43:502–507, 1981.

[126] M.H. Levitt, R. Freeman, and T. Frenkiel. *Adv. Magn. Reson.*, 11:47, 1983.

[127] D.A. Lidar, I.L. Chuang, and K.B. Whaley. Decoherence-free subspaces for quantum computation. *Phys. Rev. Lett.*, 81:2594–2597, 1998.

[128] S. Lloyd. A potentially realizable quantum computer. *Science*, 261:1569–1571, 1993.

[129] S. Lloyd. Envisioning a quantum supercomputer. *Science*, 263:695, 1994.

[130] S. Lloyd. Universal quantum simulators. *Science*, 273:1073, 1996.

[131] C.C. Lopez, B. Levi, and D.G. Cory. Error characterization in quantum information processing: A protocol for analyzing spatial correlations and its experimental implementation. *Phys. Rev. A*, 79:042328, 2009.

[132] D. Loss and D.P. DiVincenzo. Quantum computation with quantum dots. *Phys. Rev. A*, 57:120–126, 1998.

[133] B. Luy, K. Kobzar, T.E. Skinner, N. Khaneja, and S.J. Glaser. Construction of universal rotations from point-to-point transformations. *J. Magn. Reson.*, 176:179–186, 2005.

[134] E. Magesan, D. Puzzuoli, C.E. Granade, and D.G. Cory. Modeling quantum noise for efficient testing of fault-tolerant circuits. *arXiv:1206.5407*, 2012.

[135] J. Majer, J.M. Chow, J.M. Gambetta, J. Koch, B.R. Johnson, J.A. Schreier, L. Frunzio, D.I. Schuster, A.A. Houck, A. Wallraff, A. Blais, M.H. Devoret, S.M. Girvin, and R.J. Schoelkopf. Coupling superconducting qubits via a cavity bus. *Nature*, 449:443–447, 2007.

[136] J.B. Majer, F.G. Paauw, A.C.J. Ter Haar, C.J.P.M. Harmans, and J.E. Mooij. Spectroscopy on two coupled superconducting flux qubits. *Phys. Rev. Lett.*, 94:090501, 2005.

[137] P. Maletinsky, S. Hong, M.S. Grinolds, B. Hausmann, M.D. Lukin, R.L. Walsworth, M. Loncar, and A. Yacoby. A robust scanning diamond sensor for nanoscale imaging with single nitrogen-vacancy centres. *Nature Nano.*, 7:320, 2012.

[138] H. Malissa, D.I. Schuster, A.M. Tyryshkin, A.A. Houck, and S.A. Lyon. Superconducting coplanar waveguide resonators for low temperature pulsed electron spin resonance spectroscopy. *arXiv:1202.6305*, February 2012.

[139] M. Mannini, L. Sorace, L. Gorini, F.M. Piras, A. Caneschi, A. Magnani, S. Menichetti, and D. Gatteschi. Self-assembled organic radicals on au(111) surfaces: A combined tof-sims, stm, and esr study. *Langmuir*, 23:2389, 2007.

[140] J. Mao, T.H. Mareci, K.N. Scott, and E.R. Andrew. Selective inversion radiofrequency pulses by optimal control. *J. Magn. Reson.*, 70:310, 1986.

[141] A.A. Maudsley. Modified carr-purcell-meiboom-gill sequence for nmr fourier imaging applications. *J. Magn. Reson.*, 69:488–491, 1986.

[142] J.R. Maze, P.L. Stanwix, J.S. Hodges, S. Hong, J.M. Taylor, P. Cappellaro, L. Jiang, M.V.G. Dutt, E. Togan, A.S. Zibrov, A. Yacoby, R.L. Walsworth, and M.D. Lukin. Nanoscale magnetic sensing with an individual electronic spin in diamond. *Nature*, 455:644–647, 2008.

[143] R.C. McCalley and A.L. Kwiram. Endor studies at 4.2 k of the radicals in malonic acid single crystals. *J. Phys. Chem.*, 97:2888–2903, 1993.

[144] M. Mehring. *Principles of High Resolution NMR in Solids.* Springer-Verlag, 1983.

[145] M. Mehring and J. Mende. Spin-bus concept of spin quantum computing. *Phys. Rev. A*, 73:052303, 2006.

[146] M. Mehring, J. Mende, and W. Scherer. Entanglement between an electron and a nuclear spin-1/2. *Phys. Rev. Lett.*, 90:153001, 2003.

[147] M. Mehring, W. Scherer, and A. Weidinger. Pseudoentanglement of spin states in the multilevel 15n@c60 system. *Phys. Rev. Lett.*, 93:206603, 2004.

[148] M. Mehring and J.S. Waugh. Phase Transients in Pulsed NMR Spectrometers. *Rev. Sci. Instr.*, 43(4):649–653, 1972.

[149] S. Meiboom and D. Gill. Modified spin-echo method for measuring nuclear relaxation times. *Rev. Sci. Instru.*, 29:688–691, 1958.

[150] C.A. Meriles, D. Sakellariou, H. Heise, A.J. Moule, and A. Pines. Approach to high-resolution ex situ nmr spectroscopy. *Science*, 293:82–85, 2001.

[151] J. Le Moigne, J.L. Gallani, P. Wautelet, M. Moroni, L. Oswald, C. Cruz, Y. Galerne, J.C. Arnault, R. Duran, and M. Garett. Nitronyl nitrozide and imino nitroxide mono- and biradicals in langmuir and langmuir-blodgett films. *Langmuir*, 14:7484, 1998.

[152] C. Monroe, D.M. Meekhof, B.E. King, W.M. Itano, and D.J. Wineland. Demonstration of a fundamental quantum logic gate. *Phys. Rev. Lett.*, 75:4714–4717, 1995.

[153] A. Morello, J.J. Pla, F.A. Zwanenburg, K.W. Chan, K.Y. Tan, H. Huebl, M. Mottonen, C.D. Nugroho, C. Yang, J.A. van Donkelaar, A.D.C. Alves, D.N. Jamieson, C.C. Escott, L.C.L. Hollenberg, R.G. Clark, and A.S. Dzurak. Single-shot readout of an electron spin in silicon. *Nature*, 467:687, 2010.

[154] G.A. Morris and R. Freeman. Selective excitation in fourier transform nuclear magnetic resonance. *J. Magn. Reson.*, 29:433–462, 1978.

[155] J.J.L. Morton, A.M. Tyryshkin, R.M. Brown, S. Shankar, B.W. Lovett, A. Ardavan, T. Schenkel, E.E. Haller, J.W. Ager, and S.A. Lyon. Solid-state quantum memory using the 31p nuclear spin. *Nature*, 455:1085–1088, 2008.

[156] O. Moussa, J. Baugh, C.A. Ryan, and R. Laflamme. Demonstration of Sufficient Control for Two Rounds of Quantum Error Correction in a Solid State Ensemble Quantum Information Processor. *Phys. Rev. Lett.*, 107:160501, October 2011.

[157] K.W. Murch, U. Vool, D. Zhou, S.J. Weber, S.M. Girvin, and I. Siddiqi. Cavity-assisted quantum bath engineering. *arXiv:1207.0053*, 2012.

[158] M.A. Nielsen and I.L. Chuang. *Quantum Computation and Quantum Information.* Cambridge University Press, Cambridge, UK, 2000.

[159] J. Perlo, V. Demas, F. Casanova, C.A. Meriles, J. Reimer, A. Pines, and B. Blümich. High-resolution nmr spectroscopy with a portable single-sided sensor. *Science*, 308:1279, 2005.

[160] J.R. Petta, A.C. Johnson, J.M. Taylor, E.A. Laird, A. Yacoby, M.D. Lukin, C.M. Marcus, M.P. Hanson, and A.C. Gossard. Coherent manipulation of coupled electron spins in semiconductor quantum dots. *Science*, 309:2180–2184, 2005.

[161] L.M. Pham, D. Le Sage, P.L. Stanwix, T.K. Yeung, D. Glenn, A. Trifonov, P. Cappellaro, P.R. Hemmer, M.D. Lukin, H. Park, A. Yacoby, and R.L. Walsworth. Magnetic field imaging with nitrogen-vacancy ensembles. *New J. Phys.*, 13:045021, 2011.

[162] E. Pinch. *Optimal Control and the Calculus of Variations.* Oxford University Press, Oxford, 1993.

[163] L. Pontryagin, B. Boltyanskii, R. Gamkrelidze, and E. Mishchenko. *The Mathematical Theory of Optimal Processes.* Wiley-Interscience, New York, 1962.

[164] M.A. Pravia, N. Boulant, J. Emerson, A. Farid, E.M. Fortunato, T.F. Havel, R. Martinez, and D.G. Cory. Robust control of quantum information. *J. Chem. Phys.*, 119:9993–10001, 2003.

[165] D.A. Pushin, M.G. Huber, M. Arif, and D.G. Cory. Experimental realization of decoherence-free subspace in neutron interferometry. *Phys. Rev. Lett.*, 107:150401, 2011.

[166] H.A. Rabitz, M.M. Hsieh, and C.M. Rosenthal. Quantum optimally controlled transition landscapes. *Science*, 303:1998–2001, 2004.

[167] V. Ramakrishna, M.V. Salapaka, M. Dahleh, H. Rabitz, and A. Peirce. Controllability of molecular systems. *Phys. Rev. A*, 51(2):960–966, February 1995.

[168] C. Ramanathan, P. Cappellaro, L. Viola, and D.G. Cory. Experimental characterization of coherent magnetization transport in a one-dimensional spin system. *New J. Phys.*, 13:103015, 2011.

[169] G.A. Rinard, R.W. Quine, S.S. Eaton, and G.R. Eaton. Frequency dependence of epr sensitivity. *Bio. Magn. Reson.*, 21:115–154, 2004.

[170] G.A. Rinard, R.W. Quine, S.S. Eaton, G.R. Eaton, and W. Froncisz. Relative Benefits of Overcoupled Resonators vs Inherently Low-Q Resonators for Pulsed Magnetic Resonance. *J. Magn. Reson. A*, 108(1):71–81, May 1994.

[171] D. Rosenfeld and Y. Zur. Design of adiabatic selective pulses using optimal control theory. *Magn. Reson. Med.*, 36:401–409, 1996.

[172] D. Rugar, R. Budakian, H.J. Mamin, and B.W. Chui. Single spin detection by magnetic resonance force microscopy. *Nature*, 430:329, 2004.

[173] C.A. Ryan, O. Moussa, J. Baugh, and R. Laflamme. Spin based heat engine: Demonstration of multiple rounds of algorithmic cooling. *Phys. Rev. Lett.*, 100:140501, 2008.

[174] C.A. Ryan, C. Negrevergne, M. Laforest, E. Knill, and R. Laflamme. Liquid-state nuclear magnetic resonance as a testbed for developing quantum control methods. *Phys. Rev. A*, 78:012328, 2008.

[175] M. Saffman, T. G. Walker, and K. Molmer. Quantum information with rydberg atoms. *Rev. Mod. Phys.*, 82:2313–2363, 2010.

[176] A.P. Sage. *Optimum Systems Control.* Prentice-Hall, Inc., Englewood Cliffs, NJ, 1968.

[177] S.G. Schirmer, H. Fu, and A.I. Solomon. Complete controllability of quantum systems. *Phys. Rev. A*, 63:063410, 2001.

[178] L.J. Schulman and U. Vazirani. Scalable nmr quantum computation. In *Proceedings of the 31st Annual ATM (STOC)*, pages 322–329, 1998.

[179] A. Schweiger and G. Jeschke. *Principles of Pulse Electron Paramagnetic Resonance.* Oxford University Press, 2001.

[180] A.J. Shaka, J. Keeler, T. Frenkiel, and R. Freeman. An improved sequence for broadband decoupling: Waltz-16. *J. Magn. Reson.*, 52:335–338, 1983.

[181] C.E. Shannon. A mathematical theory of communication. *The Bell Systems Technical Journal*, 27:379–423, 1948.

[182] P.W. Shor. Scheme for reducing decoherence in quantum computer memory. *Phys. Rev. A*, 52:2493–2496, 1995.

[183] L. Shtirberg, T. Twig, E. Dikarov, R. Halevy, M. Levit, and A. Blank. High-sensitivity q-band electron spin resonance imaging system with submicron resolution. *Rev. Sci. Instr.*, 82:043708, 2011.

[184] T.E. Skinner, K. Kobzar, B. Luy, M.R. Bendall, W. Bermel, N. Khaneja, and S.J. Glaser. Optimal control design of constant amplitude phase-modulated pulses: Application to calibration-free broadband excitation. *J. Magn. Reson.*, 179:241–249, 2006.

[185] T.E. Skinner, T.O. Reiss, B. Luy, N. Khaneja, and S.J. Glaser. Application of optimal control theory to the design of broadband excitation pulses for high-resolution nmr. *J. Magn. Reson.*, 163:8–15, 2003.

[186] T.E. Skinner, T.O. Reiss, B. Luy, N. Khaneja, and S.J. Glaser. Reducing the duration of broadband excitation pulses using optimal control with limited rf amplitude. *J. Magn. Reson.*, 167:68–74, 2004.

[187] C.P. Slichter. *Principles of Magnetic Resonance.* Springer-Verlag, New York, 1992.

[188] M.A. Smith, H. Hu, and A.J. Shaka. Improved broadband inversion performance for nmr in liquids. *J. Magn. Reson.*, 151:269–283, 2001.

[189] K-A B. Soderberg and C. Monroe. Phonon-mediated entanglement for trapped ion quantum computing. *Rep. Prog. Phys.*, 73:036401, 2010.

[190] A. Sodickson and D.G. Cory. A generalized k-space formalism for treating the spatial aspects of a variety of nmr experiments. *J. Prog. Nuc. Magn. Reson. Spect.*, 33:77–108, 1998.

[191] S.S. Soliman and M.D. Srinath. *Continuous and Discrete Signals and Systems.* Prentice-Hall, 1998.

[192] S. Somaroo, C.H. Tseng, T.F. Havel, R. Laflamme, and D.G. Cory. Quantum simulations on a quantum computer. *Phys. Rev. Lett.*, 82:5381, 1999.

[193] P.E. Spindler, Y. Zhang, B. Endeward, N. Gershernzon, T.E. Skinner, S.J. Glaser, and T.F. Prisner. Shaped optimal control pulses for increased excitation bandwidth in epr. *J. Magn. Reson.*, 218:49–58, 2012.

[194] A.M. Steane. Multiple-particle interference and quantum error correction. *Proc. R. Soc. Lond. A*, 452:2551–2557, 1996.

[195] A.M. Stephens and Z.W.E. Evans. Accuracy threshold for concatenated error detection in one dimension. *Phys. Rev. A*, 80:022313, 2009.

[196] E. Suhovoy, R. Halevy, L. Shtirberg, and W. Herneit. Esr imaging in solid phase down to sub-micron resolution: methodology and applications. *Phys. Chem. Chem. Phys.*, 11:6689–6699, 2009.

[197] D. Suter and K. Lim. Scalable architecture for spin-based quantum computers with a single type of gate. *Phys. Rev. A*, 65:052309, 2002.

[198] D. Suter and T.S. Mahesh. Spins as qubits: Quantum information processing by nuclear magnetic resonance. *J. Chem. Phys.*, 128:052206, 2008.

[199] Y. Tabuchi, M. Negoro, K. Takeda, and M. Kitagawa. Total compensation of pulse transients inside a resonator. *J. Magn. Reson.*, 204(2):327–332, June 2010.

[200] K. Takeda, Y. Tabuchi, M. Negoro, and M. Kitagawa. Active compensation of rf-pulse transients. *J. Magn. Reson.*, 197(2):242–244, April 2009.

[201] K. Temme, T. J. Osborne, K. G. Vollbrecht, D. Poulin, and F. Verstraete. Quantum metropolis sampling. *Nature*, 471:87–90, 2011.

[202] M. Tseitlin, R.W. Quine, G.A. Rinard, S.S. Eaton, and G.R. Eaton. Digital EPR with an arbitrary waveform generator and direct detection at the carrier frequency. *J. Magn. Reson.*, 213:119–125, September 2011.

[203] A.M. Turing. On computable numbers, with an application to the *Entscheidungs problem. Proc. Lond. Math. Soc.*, 42:230–265, 1936.

[204] J. Twamley. Quantum-cellular-automata quantum computing with endohedral fullerenes. *Phys. Rev. A*, 67:052318, 2003.

[205] Y. Twig, E. Dikarov, W.D. Hutchison, and A. Blank. Note: High sensitivity pulsed electron spin resonance spectroscopy with induction detection. *Rev. Sci. Instr.*, 82:076105, 2011.

[206] G.S. Uhrig. Keeping a quantum bit alive by optimized pi-pulse sequences. *Phys. Rev. Lett.*, 98:100504, 2007.

[207] W.G. Unruh. Maintaining coherence in quantum computers. *Phys. Rev. A*, 51:992–997, 1995.

[208] H. Uys, M.J. Biercuk, and J.J. Bollinger. Optimized noise filtration through dynamical decoupling. *Phys. Rev. Lett.*, 103:040501, 2009.

[209] S.O. Valenzuela, W.D. Oliver, D.M. Berns, K.K. Berggren, L.S. Levitov, and T.P. Orlando. Microwave-induced cooling of a superconducting qubit. *Science*, 314:1589, 2006.

[210] R.W. Vaughan, D.D. Elleman, L.M. Stacey, W-K. Rhim, and J.W. Lee. A simple, low power, multiple pulse nmr spectrometer. *Rev. Sci. Instr.*, 43:1356–1364, 1972.

[211] A.J. Vega. Controlling the effects of pulse transients and rf inhomogeneity in phase-modulated multiple-pulse sequences for homonuclear decoupling in solid-state proton nmr. *J. Magn. Reson.*, 170:22–41, 2004.

[212] L. Viola and E. Knill. Robust dynamical decoupling of quantum systems with bounded controls. *Phys. Rev. Lett.*, 90:037901, 2003.

[213] L. Viola, E. Knill, and R. Laflamme. Constructing qubits in physical systems. *J. Phys. A: Math. Gen.*, 34:7067, 2001.

[214] L. Viola and S. Lloyd. Dynamical suppression of decoherence in two-state quantum systems. *Phys. Rev. A*, 58:2733–2744, 1998.

[215] W.S. Warren, S. Ahn, M. Mescher, M. Garwood, K. Ugurbil, W. Richter, R.R. Rizi, J. Hopkins, and J.S. Leigh. Mr imaging contrast enhancement based on intermolecular zero quantum coherences. *Science*, 281:247–251, 1998.

[216] J. Watrous. Semidefinite programs for completely bounded norms. *Theory of Computing*, 5:11, 2009.

[217] J.S. Waugh. Theory of broadband spin decoupling. *J. Magn. Reson.*, 50:30–49, 1982.

[218] Y.S. Weinstein, T.F. Havel, J. Emerson, N. Boulant, M. Saraceno, S. Lloyd, and D.G. Cory. Quantum process tomography of the quantum Fourier transform. *J. Chem. Phys.*, 121(13):6117–6133, 2004.

[219] J.H. Wesenberg, A. Ardavan, G.A.D. Briggs, J.J.L. Morton, R.J. Schoelkopf, D.I. Schuster, and K. Molmer. Quantum computing with an electron spin ensemble. *Phys. Rev. Lett.*, 103:070502, 2009.

[220] J.R. West, D.A. Lidar, B.H. Fong, and M.F. Gyure. High fidelity quantum gates via dynamical decoupling. *Phys. Rev. Lett.*, 105:230503, 2010.

[221] C.J. Wood, J.D. Biamonte, and D.G. Cory. Tensor networks and graphical calculus for open quantum systems. *arXiv:1111.6950v1*, 2011.

[222] W.K. Wooters and W.H. Zurek. A single quantum cannot be cloned. *Nature*, 299:802–803, 1982.

[223] J. Wrachtrup and F. Jelezko. Processing quantum information in diamond. *J. Phys.: Cond. Matt.*, 18:S807, 2006.

[224] P. Zanardi. Stabilizing quantum information. *Phys. Rev. A*, 63:012301, 2000.

[225] P. Zanardi and M. Rasetti. Noiseless quantum codes. *Phys. Rev. Lett.*, 79:3306–3309, 1997.

[226] S. Zhang, X. Wu, and M. Mehring. Elimination of ringing effects in multiple-pulse sequences. *Chem. Phys. Lett.*, 173:481–484, 1990.

[227] Y. Zhang, C.A. Ryan, R. Laflamme, and J. Baugh. Coherent Control of Two Nuclear Spins Using the Anisotropic Hyperfine Interaction. *Phys. Rev. Lett.*, 107:170503, October 2011.